SRT-1

VALOR

Technical Analysis Report

SPRING 2014

Texas A&M University Sounding Rocketry Team
Department of Aerospace Engineering

CONTENTS

1. Introduction 1

1.1. Objectives 1

1.2. Project Structure 2

1.3. General Layout 3

2. Dynamics and Controls 5

2.1. Objective 5

2.2. Trajectory 5

2.2.1. Rocket Modeled as a Point-Mass 5

2.2.2. Equations of Motion for a Rigid Body Model 6

2.3. Stability 9

2.3.1. Layout of the Rocket 9

2.3.2. Center of Gravity 10

2.3.3. Longitudinal Dynamic Stability 11

2.3.4. Non-linear Aerodynamics 12

2.3.5. Consideration of Cant Angles 12

2.4. Fin Design 13

2.4.1. Geometry 13

2.4.2. Airfoil 14

2.4.3. Amount of Fins 16

2.5. Computer Modeling 16

2.5.1. Rocksim 19

2.5.2. Simulation Verification 19

2.5.3. Independent Simulation 19

2.6. References 19

3. Engine 21

3.1. Objective 21

3.2. Oxidizer and Fuel 21

3.3. Combustion Chamber 25

3.4. Injector System 27
3.5. Nozzle 29
3.6. Plumbing 32
3.6.1. Oxidizer Tank and Fittings 32
3.6.2. Flow Analysis 33
3.6.3. Quick Disconnect 36
3.7. System Modelling 36
3.7.1. Analysis of Engine Performance 36
3.7.2. Engine Simulation Results 39
3.8. Fabrication Analysis 41
3.9. Testing 42
3.10. References 43
4. Aerodynamics 45
4.1. Objective 45
4.2. Theoretical Aerodynamics 45
4.3. Body Aerodynamics 46
4.4. Fin Aerodynamics 46
4.5. Nose Cone 47
4.5.1. Subsonic Nose Cone 47
4.5.2. Nose Cone for Transonic Flight 48
4.5.3. Choice of Nose cone 49
4.6. Total Vehicle Aerodynamics and Center of Pressure 49
4.7. Computational Fluid Dynamics 50
4.8. References 52
5. Recovery 54
5.1. Objective 54
5.2. Drogue 54
5.3. Main 56
5.4. Deployment 57

5.4.1. Two-Stage Deployment 58
5.4.2. Deployment Forces 59
5.5. Fabrication and Testing 62
5.6. References 62
6. Electronics and Instrumentation 63
6.1. Objective 63
6.2. Instruments 63
6.2.1. Configuration 63
6.2.2. Altimeters 64
6.2.3. Programmable Computer 65
6.2.4. Tracking device 66
6.3. Power 66
6.4. Electronics Bay Assembly and Wiring 67
6.4.1. Assembly 67
6.4.2. Wiring 68
6.5. Testing 69
6.6. References 69
7. Payload 70
7.1. Design Considerations 70
7.2. Fabrication Analysis 70
7.3. Instrumentation 71
7.4. Testing 71
8. Vehicle Structure 71
8.1. Objective 71
8.2. Body Tube 71
8.2.1. Structural Analysis 72
8.2.2. Manufacturing Plan 72
8.3. Body Tube Connectors 73
8.4. Bulkheads 74

8.4.1. Engine Bulkhead 74
8.4.2. Recovery Bulkhead 74
8.5. Vehicle Fastener Analysis 76
8.6. Fabrication Analysis 77
8.7. Testing 78
8.8. References 78
9. Safety 79
9.1. Objective 79
9.2. Documentation 79
9.3. Training Requirements 79
9.4. Testing Authorization 80
9.5. References 80
10. Registration and Finance 81
10.1. Registration Deadlines 81
10.2. Budget 81
10.3. Fundraising/Sponsorships 82
11. Conclusion 82
12. Acknowledgments 83

Table of Figures

Figure 1.1. Team structure. 2

Figure 1.2. Rocket component layout. 3

Figure 2.1. Rocket modeled as a point-mass. 5

Figure 2.2. Rocket model. 6

Figure 2.3. Preliminary layout of the rocket. 10

Figure 2.4. Tail contribution to damping pitch. 12

Figure 2.5. Normal Force Coefficient vs Angle of Attack. 12

Figure 2.6. Illustration of cant angles. 12

Figure 2.7. Contour plots of the static margin for different pairs of variables. 13

Figure 2.8. Current dimensions of the fin. 14

Figure 2.9. NACA 65-010 Profile[5]. 14

Figure 2.10. NACA 65-006 Profile[5]. 15

Figure 2.11. NACA 65-006 Orthographic View. 15

Figure 2.12. Drag coefficient for different fineness and designs. 16

Figure 2.13 a) Height as a Function of Time b) Velocity as a Function of Time c) Acceleration as a Function of Time 18

Figure 3.1. (a) Combustion temperature (Kelvin) versus O:F ratio, (b) Specific heat ratio versus O:F ratio, (c) Average molecular weight versus O:F ratio. 24

Figure 3.2. Recessed Rising Sun port configuration. 25

Figure 3.3. (a) Exploded view of the Injector (b) Upstream side of Injector Plate. 28

Figure 3.4. Section view of injector system. 29

Figure 3.5. Cross-section of the nozzle. 31

Figure 3.6. Upper engine arrangement from oxidizer tank (left) to injector plate (right). 32

Figure 3.7. Quick disconnect system. (Right) plug (Left) body. 36

Figure 3.8. Interdependency of parameters in hybrid rocket engines. (courtesy: Aspire Space) 37

Figure 3.9. Theoretical Thrust vs. Time curve 40

Figure 3.10. Theoretical Combustion Chamber Pressure vs. Time curve. 40

Figure 3.11. Aluminum injector coin sandwiched between the plate and combustion chamber. 43

Figure 4.1. Elliptical nosecone design concept. 47

Figure 4.2 Performance for different nose cones and Mach numbers 47

Figure 4.3 Drag Coefficients for different nose cone designs. 48

Figure 4.4. 2D plot of Von Kármán nose cone design 48

Figure 4.5. Drag coefficient for different fineness and designs 49

Figure 4.6. Cylinder Test Case Replica[7,8] 51

Figure 4.7. 65-006 CFD results.[7] 52

Figure 4.8 Dynamic Pressure using Eqns. 4.7.1. and 4.7.2.[7] 52

Figure 5.1. Gore layup template. [4].....55
Figure 5.2. Rotafoil gore sizing. 55
Figure 5.3. Typical infinite mass force-time history of a solid cloth parachute in a wind tunnel.[2] 56
Figure 5.4. Gore for main parachute.....57
Figure 5.5. Bullet Casings 58
Figure 5.6. Defy Gravity Tether 59
Figure 5.7. Opening Forces of a Parachute.....59
Figure 5.8. Optimal Line Lengths for Coefficient of Drag of Parachute [4]. 61
Figure 6.1. Electronics Bay with Center of Gravity. 67
Figure 6.2. E-Bay Ortho-view. 67
Figure 6.3. Schematic Diagram 68
Figure 7.1. The judging sheet for the official evaluation of the payload is shown. 70
Figure 8.1. The Little Hornet filament winder is shown with one layer of yarn partially laid up. 72
Figure 8.2. Carbon fiber tube laid up and epoxied. 73
Figure 8.3. Body Tube Connector 73
Figure 8.4. Lower Engine bulkhead 74
Figure 8.5. Recovery Bulkhead 75
Figure 8.6. Recovery Bulkhead Stress Contours 76

Table of Tables

Table 2.1. Center of gravity distribution. 11
Table 2.2. Values used in MATLAB Rocket Model and Results 17
Table 2.3. Verification Data 19
Table 2.4. Full Prediction 19
Table 3.1. Nitrous oxide properties at different temperatures. 21
Table 3.2. Comparison between the final three fuels. 23
Table 3.3. Initial fuel grain specifications based on required thrust. 24
Table 3.4. Property comparison of phenolics and silica. 26
Table 3.5. Final Nozzle Design Parameters 31
Table 3.6. Pressure losses through the plumbing. 34
Table 3.7. Inputs used for engine simulation. 39
Table 3.8. Material properties of brass and aluminum. 42
Table 5.1. Parameters for the Drogue Rotafoil Parachute 54
Table 5.2. Parameters for the Main Parachute. 56
Table 5.3. Summary of Parachute Shape Test Results. [3] 60
Table 5.4. Parachute Weights 61
Table 6.1. PerfectFlite Stratologger specifcications. 64
Table 6.2. G-wiz LCX specifications. 64
Table 6.3. G-wiz HCX specifications. 65
Table 6.4. Atlas TeleMetrum specifications. 65
Table 6.5. Components of the electronics bay. 68
Table 10.1. Budget layout for the academic year. 82

1. Introduction

1.1. Objectives

The Texas A&M University Sounding Rocketry Team, or SRT, is a multi-disciplinary design organization originating in the Department of Aerospace Engineering. The team was established over the summer of 2013, with the managers of each respective subdivision being recruited on a personal basis by the team director. Being its first year in existence, the SRT mimicked the capstone design courses by self-requiring two preliminary design reviews in the fall semester and a critical design review at the end. The SRT has four overarching objectives: (1) to compete in and win the Intercollegiate Rocket Engineering Competition, (2) to develop practicality of academic studies to design challenges, (3) to enhance interpersonal communication as part of an engineering team, and (4) to prepare students in the area of oral presentations and technical reports.

The primary objective of the SRT is to compete in the Intercollegiate Rocket Engineering Competition, or IREC, which is run by the Experimental Sounding Rocket Association. This event is held every June in Green River, Utah. Universities from all over the world participate in this three day event. Texas A&M University would enter its first year under the basic class. This category's rules dictate that the rocket must reach at least 5,000ft above ground level (AGL) to qualify, with an optimal target altitude of precisely 10,000ft AGL. The rocket must carry a 10-lb payload the entire flight and the team must be able to recover the payload intact for maximum points. The payload is defined as an object which could be replaced with a dead weight and not affect the other functions and overall flight of the rocket, though scientific payloads maximize points. A poster is also included in the presentations at the event and each team member must be capable of answering questions directed to them by official judges. The main challenge in achieving this goal is to get enough money to send individuals to the competition, which makes up a good portion of our budget (Section 10).

The most prevalent conditioning that the SRT provides is the bridge between the classroom and workroom. Many students in engineering long for hands-on experience and the ability to apply concepts to real-world challenges. Building a high-powered rocket to reach a target altitude provides a demanding task that develops that experience for each member of the team. The entire team is structured in a very similar way to the senior capstone course, except in the sense that the team managers and upperclassmen take on underclassmen to teach them not only hands-on tools, but analytical concepts they may not have had classes for yet. This provides earlier development of students in both the Aerospace and Mechanical Engineering departments and keeps those not as interested in lecture-type teachings still interested in their majors.

Team communication skills are also a main priority for members, as well as those in leadership positions. Each team is structured so that a manager oversees the progress of different components of the rocket. That manager is, in turn, responsible for clear communication to both the team director and the graduate student advisor (Section 1.2). By having a strict organizational approach, each member works on being able to effectively communicate with their supervisor. While team members are encouraged to talk to others not necessarily on their sub-team, it is stressed that vital information go through managers to avoid miscommunication and maintain accuracy of data.

The final goal of the team is to allow a stage where students can practice their presentation skills before the beginning of their senior year. The fall semester contains two preliminary design reviews and one critical design presentation which demands that each member communicate their findings effectively on a public stage. These reviews also maintain accountability of design concepts for each member, whether it be productive or not. A number of professors attended these reviews last semester and each time the input was used to further improve the function of the rocket.

1.2. Project Structure

As mentioned in the previous section, the SRT utilizes both semesters of the academic school year to design, build, and test the rocket. The first semester is primarily design and filling any knowledge gaps that members may have about their components, while the second semester is dedicated to fabrication and testing. In order to achieve these things, however, the team was organized into three teams: dynamics & operation, structures, and propulsion (engine). Team leadership was also vitally structured to make sure there were no mishaps in the design or build phases of the project.

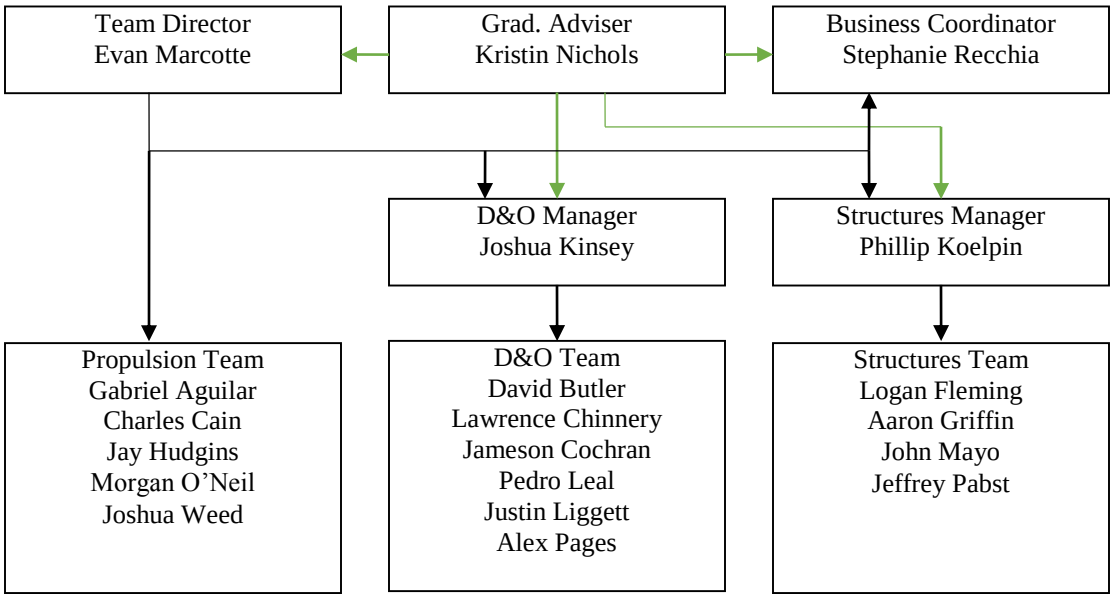

Figure 1.1. Team structure.

The project is headed by the team director, Evan Marcotte, who is responsible for faculty communication, administrative reports, and overall team management. The graduate student advisor, Kristin Nichols, serves as a "mentor" to everyone on the team, including the team director. She led the vehicle team in her senior design class during the 2012-2013 school year, so she has far more experience with building a rocket than anyone on the team. The business coordinator was selected with all of the other members during the application and interview process. Her main goal is to act as the professional business administrator to both potential donors, the competition officials, and faculty advisers.

The rest of the team is divided into the three subdivisions listed in Fig. 1.1. The Dynamics & Operations team is under the management of Joshua Kinsey, while the Structures team is headed by Santos Ramirez. Each team manager, with the exception of the business coordinator, was recruited prior to the end of spring 2013. Members were chosen from around 46 applicants ranging from freshmen to graduate students in both the Mechanical and Aerospace Engineering Departments. Overall, twelve aerospace and four mechanical students were chosen, with a Brazilian student eventually joining the team in an international collaboration with his university. This brings the total membership of the team to twenty-one individuals; however, Santos Ramirez graduated in December so the current membership stand at twenty.

1.3. General Layout

The layout of the rocket is not very special in any regard. The intent of the design was to keep it simple, but also have it do exactly what the design requirements demanded. Given Dr. Pollock's experience in building rockets, it was decided that the general layout be very similar to rockets that have already been built. Components include the engine assembly, payload compartment, electronics bay, recovery system, body tube, bulkheads, and fin structure. Each of these items is then divided into further analysis and development based on its designated team. Figure 1.2 shows the overall design of the rocket.

Figure 1.2. Rocket component layout.

One of the main parameters that was decided early on in the design process was that the rocket would not contain an active control system, unlike the 2012-13 senior design class. This was due to an increase in the complexity of the rocket as well as the ambiguity of what exactly was restricted by the International Traffic in Arms Regulations, or ITAR. Since the competition allows teams from other countries to evaluate the rocket, ask questions, and look over designs in detail, utilizing an active control system seemed legally suspect.

The engine design of the rocket followed previous years by analyzing and developing a hybrid engine. While much more complex than a solid motor, the hybrid structure allows for more points in the competition and provided a great learning experience for the team. One concern leading into the year was that a hybrid may be too advanced for the first year but, as Section 3 will hopefully prove, the members were more than capable of utilizing their academic know-how to predict the thrust-time curve of a hybrid engine. Liquid engines were analyzed at the beginning of the year as well for educational purposes, but the safety concerns, weight requirements, and extreme complexity of required pumps never made them a serious consideration for a team in its first year.

The structure of the rocket also differed significantly from the senior capstone class in that the body tube would be made from carbon fiber wound on a filament winder. During the fall semester this was considered a stretch given the cost of carbon fiber, the nonexistence of funds in the team's account, and the team's inexperience with a winder. Even so, the structures team learned the entire winding process from scratch on their own and a lot of materials were donated to the team by Dr. Creasy (MEEN), who also provided the filament winder. Without a doubt, the structure of the rocket as deigned could not have been done without Dr. Creasy's help.

2. Dynamics and Controls

2.1. Objective

The dynamics and controls requirements were provided by the ESRA, and an additional set of requirements were agreed upon by the team for performance standards. First, the rocket must be statically stable without the assistance of active control surfaces. Second, the rocket is designed to reach apogee at precisely 10,000 ft. above ground level with qualification altitudes between 5,000 and 12,000 ft. Last, for stability purposes, the rocket is designed with a static margin of 1 to 2 rocket diameters (6 to 12 in.) with an acceptable margin between 1 and 4 (6 to 24 in.).

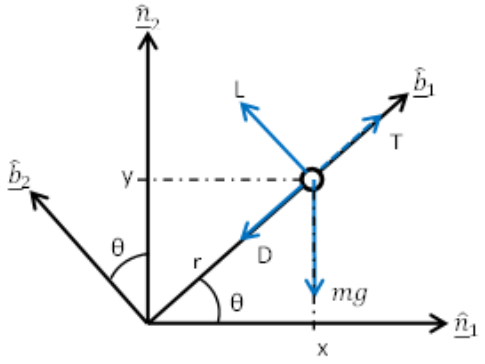

Figure 2.1. Rocket modeled as a point-mass.

2.2. Trajectory

2.2.1. Rocket Modeled as a Point-Mass

Beginning with the basis that the rocket was a simple point-mass, an inertial and body reference frame were defined as seen in Figure 2.1. The inertial frame was denoted with an "n" and the body frame was denoted with a "b." The angle "θ" represented the angle from the ground to the rocket's location and was measured from the $\hat{n}_1$ direction. For this particular case, the distance was defined as some radial length "r" between the point-mass and the launch site along the $\hat{b}_1$ direction. The relationship between the inertial and body frame can be seen below.

$$\hat{n}_1 = cos(\theta)\,\hat{b}_1 - sin(\theta)\hat{b}_2 \tag{2.1}$$

$$\hat{n}_2 = sin(\theta)\hat{b}_1 + cos(\theta)\hat{b}_2 \tag{2.2}$$

$$\hat{b}_1 = cos(\theta)\hat{n}_1 + sin(\theta)\hat{n}_2 \tag{2.3}$$

$$\hat{b}_2 = -sin(\theta)\hat{n}_1 + cos(\theta)\hat{n}_2 \tag{2.4}$$

The forces shown in Figure 2.1 are the lift, symbolized as "L," drag as "D," and the mass of the rocket multiplied by gravity as "mg." Each of these forces represented a resultant of the various surface or body loads that the rocket was expected to experience during flight.

These forces were initially expressed in their respective reference frames before undergoing a coordinate transformation into the inertial reference frame. This utilization of Equations 2.3 and 2.4, and the sum of the forces can be seen below:

$$\underline{F} = -mg\hat{n}_2 - D\,\hat{b}_1 + L\,\hat{b}_2 \tag{2.5}$$

$$\underline{F} = -\big(Lsin(\theta) + Dcos(\theta)\big)\hat{n}_1 + (Lcos(\theta) - Dsin(\theta) - mg)\hat{n}_2 \tag{2.6}$$

The next step in deriving the equations of motion was to develop the kinematic equations. This involved defining a position equation and taking the derivative with respect to time up to the acceleration equation, as seen in equations 2.7-2.9.

$$\underline{p} = x\underline{\hat{n}}_1 + y\underline{\hat{n}}_2 \tag{2.7}$$

$$\underline{v} = \dot{x}\underline{\hat{n}}_1 + \dot{y}\underline{\hat{n}}_2 \tag{2.8}$$

$$\underline{a} = \ddot{x}\underline{\hat{n}}_1 + \ddot{y}\underline{\hat{n}}_2 \tag{2.9}$$

By applying Newton's Second Law to equations 2.9 and 2.6, the equations of motion were fully developed for this simple model, as seen below.

$$\underline{\hat{n}}_1 : -Tcos(\theta) - Lsin(\theta) - Dcos(\theta) = m\ddot{x} \tag{2.10}$$

$$\underline{\hat{n}}_2 : -Tsin(\theta) + Lcos(\theta) - Dsin(\theta) - mg = m\ddot{y} \tag{2.11}$$

While these equations provided preliminary insight as to how the rocket would fly, a more complex model was needed to develop more precise equations. As such, the next foreseeable step was to derive the equations of motion while modeling the rocket as a rigid bar.

2.2.2. Equations of Motion for a Rigid Body Model

As seen in the previous section, the rocket was modeled as a simple point-mass with two degrees of freedom. However, for precise equations of motion a more complex model was needed. As such, the rocket was modeled as a 3simple rigid bar with variable mass. This newer model took into account the orientation of the rocket as well as CG travel due to fuel loss that helped with designing a stable system.

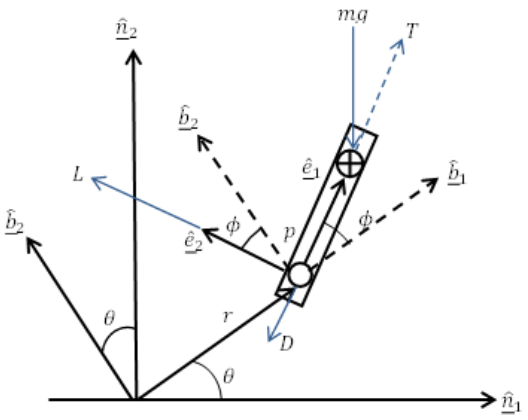

Figure 2.2. Rocket model.

This model has four degrees of freedom and three reference frames. The first two frames follow the same pattern as the previous model, where the inertial reference frame was "n," and the launch frame was denoted by a "b." This frame tracked the rocket from the launch site to the rocket's center of pressure (CP). The third frame was a body fixed frame, set at the CP location and running along the length of the body, and was denoted by an "e." Figure 2.2 is the diagram of the rocket that was modeled for this analysis. The distance from the launch site to the CP was "r" whereas the distance between the CP and CG was "p." The frame convention was set so that every cross product was positive out of the board; as such, counterclockwise rotation was considered positive. Equations 2.3 and 2.4 still hold, and will continue to, for the relationship between the "n" frame to the "b" frame while equations 2.12 through 2.14

mathematically define the relationship between the "n' frame and "e" frame. The cosines and sines in the following were represented as a simple "c" and "s", respectively.

$$\underline{\hat{e}}_1 = (c\phi c\theta - s\phi s\theta)\underline{\hat{n}}_1 + (c\phi s\theta + s\phi s\theta)\underline{\hat{n}}_2 \tag{2.12}$$

$$\underline{\hat{e}}_2 = -(s\phi c\theta + c\phi c\theta)\underline{\hat{n}}_1 + (s\phi s\theta - c\phi s\theta)\underline{\hat{n}}_2 \tag{2.13}$$

$$\underline{\hat{n}}_3 = \underline{\hat{b}}_3 = \underline{\hat{e}}_3 \tag{2.14}$$

In, Figure 2.2 the forces that acted on the rocket were represented in blue. For this case, the forces that were predicted to act on the rocket were the lift (L), drag (D), thrust (T), and gravitational forces (mg). For a simplified case, the forces on the rocket were considered to be constant throughout the derivation process. In reality, the forces listed would experience change over the course of the flight, and that is accounted for later.

The main goal of this analysis was to develop more accurate equations of motion that were based from the ground observer's point of view. Having kept the rotations of the frames in mind, the total angular velocity from the body frame to the inertial frame was found to be the following:

$$\underline{\omega}_{E/N} = (\dot{\phi} + \dot{\theta})\underline{\hat{e}}_3 = (\dot{\phi} + \dot{\theta})\underline{\hat{n}}_3 \tag{2.15}$$

Eq. 2.15 was needed to use the Transport Theorem to derive the equations of motion as well as Equations 2.12 through 2.14. Two other equations that were needed were the position of the CG and the sum of the forces acting on the rocket. Recall, the CG and CP locations were denoted by a "p" and "r," respectively. The forces that were considered to be acting on the rocket were the gravitational force (mg) at the CG, the thrust (T) acting through the CG, and the aerodynamic forces acting at the CP. The aerodynamic forces consisted of the resultant lift (L) and drag (D) forces.

$$\underline{r}_{CG} = r\underline{\hat{b}}_1 + p\underline{\hat{e}}_1 \tag{2.16}$$

$$\underline{F} = -mg\underline{\hat{n}}_2 + (T - D)\underline{\hat{e}}_1 + L\underline{\hat{e}}_2 \tag{2.17}$$

Eq. 2.17 was later rewritten in order to have all the terms in the inertial reference frame, ensuring that the equations of motion would be in a ground observer's point of view. For simplicity the components were written separately below in equations 2.18.

$$\underline{F} = F_1\underline{\hat{n}}_1 + F_2\underline{\hat{n}}_2 \tag{2.18}$$

$$F_1 = [(T - D)(c\phi c\theta - s\phi s\theta) - L(s\phi c\theta + c\phi s\theta)\,] \tag{2.18a}$$

$$F_2 = [L(c\phi c\theta - s\phi s\theta) + (T - D)(c\phi s\theta + s\phi s\theta) - mg] \tag{2.18b}$$

With Eqns. 2.15 and 2.16, the Transport Theorem was then used to derive the kinematic equations describing the motion of the CG. The first of these was the velocity of the CG. For simplicity the components were written separately

in equations 2.19 through 2.20. In this instance, the $\dot{r}$ and $\dot{p}$ represented the radial velocities; whereas the $\dot{\theta}$ and $\dot{\phi}$ represented the angular velocities.

$$\underline{v}_{CG} = v_1\underline{\hat{n}}_1 + v_2\underline{\hat{n}}_2 \tag{2.19}$$

$$v_1 = \dot{r}c\theta + r\dot{\theta}c\theta + \dot{p}(c\phi c\theta - s\phi c\theta) - p\left(\dot{\phi} - \dot{\theta}\right)(s\phi c\theta + c\phi c\theta) \tag{2.19a}$$

$$v_2 = -\dot{r}s\theta + r\dot{\theta}s\theta - \dot{p}(c\phi s\theta + s\phi s\theta) + p\left(\dot{\phi} - \dot{\theta}\right)(s\phi s\theta - c\phi s\theta) \tag{2.19b}$$

$$\underline{v}_{CG,mag} = \sqrt{v_1^2 + v_2^2} \tag{2.20}$$

The same was done for the acceleration, which became even more complex. Again, the components were written separately for simplicity. Terms with two dots over them represent the either the radial or the angular acceleration.

$$\underline{a}_{CG} = a_1\underline{\hat{n}}_1 + a_2\underline{\hat{n}}_2 \tag{2.21}$$

$$a_1 = \left(\ddot{r} - r\dot{\theta}^2\right)c\theta + \left(2\dot{r}\dot{\theta} + r\ddot{\theta}\right)c\theta + \left(\ddot{p} - p\left(\dot{\phi} - \dot{\theta}\right)^2\right)(c\phi c\theta - s\phi c\theta) - \left(2\dot{p}\left(\dot{\phi} - \dot{\theta}\right) + p\left(\ddot{\phi} - \ddot{\theta}\right)\right)(s\phi c\theta + c\phi c\theta) \tag{2.21a}$$

$$a_2 = -\left(\ddot{r} - r\dot{\theta}^2\right)s\theta + \left(2\dot{r}\dot{\theta} + r\ddot{\theta}\right)s\theta - \left(\ddot{p} - p\left(\dot{\phi} - \dot{\theta}\right)^2\right)(c\phi s\theta + s\phi s\theta) - \left(2\dot{p}\left(\dot{\phi} - \dot{\theta}\right) + p\left(\ddot{\phi} - \ddot{\theta}\right)\right)(s\phi s\theta - c\phi s\theta) \tag{2.21b}$$

The lift (L) and drag (D) forces from Eqn. 2.21were represented as the following two equations.

$$L = \frac{1}{2}C_L\rho A\underline{v}_{CG,mag}^2 \tag{2.22}$$

$$D = \frac{1}{2}C_D\rho A\underline{v}_{CG,mag}^2 \tag{2.23}$$

In Equations 2.22 and 2.23, the velocity used is the magnitude of the velocity for the center of gravity (CG) and will be defined later. The density was denoted as "ρ" and the area was denoted by an A. The area was considered constant for this case. The two coefficients were denoted by a C_D and C_L, for the respective drag and lift forces.

Newton's Second Law was now available for use for Equations 2.18 and 2.21. Before the equations of motion were finalized, the moment of inertia matrix *I* was developed. Given that for this case, the position of the CG was allowed to move, *I* was comprised of time-dependent equations that would allow each element to change over the course of the flight. The derivative of the matrix involved the chain rule for each element, and thus was simple denoted as $\dot{I}$. The original and derivative matrices were necessary for the following equations which are related to angular momentum.

$$\underline{h}_{CG} = I\left(\dot{\phi} - \dot{\theta}\right)\underline{\hat{e}}_3 \tag{2.24}$$

$$\underline{\dot{h}}_{CG} = \left[\dot{I}\left(\dot{\phi} - \dot{\theta}\right) + I\left(\ddot{\phi} - \ddot{\theta}\right)\right]\underline{\hat{e}}_3 \tag{2.25}$$

$$\underline{l}_{CG} = p\underline{\hat{e}}_1 \times L\underline{\hat{e}}_2 = pL\underline{\hat{e}}_3 \tag{2.26}$$

Then with Euler's Second Law tailored for this case, the final Equation 2.24 was derived that would allow for the equations of motion to be developed. These can be seen in the following, taking Equations 2.18, 2.21, 2.25 and 2.26.

$$\underline{\hat{n}}_1\colon\ F_1 = ma_1 \tag{2.27}$$

$$\underline{\hat{n}}_2\colon F_2 = ma_2 \tag{2.28}$$

$$\underline{\hat{n}}_3\colon \dot{I}\left(\dot{\phi} - \dot{\theta}\right) + I\left(\ddot{\phi} - \ddot{\theta}\right) = pL \tag{2.29}$$

These equations are still being analyzed and will need to be updated in order to fully comprehend how the rocket will fly. One of the reasons behind the "split" position vector for the CG was to allow for the expected change in distance between the CG and CP. The CP will be locked in place with the dimensions of the fins but the CG's location will shift forward over the course of the flight. The next step in the analysis will be to develop an appropriate time-varying equation for the area in Equations 2.22 and 2.23. This is due to the fact that as the rocket lifts off, there will be slight perturbations that expose the sides of the rocket to the drag force that the rocket is expected to experience. Further analysis will also be needed to properly develop the moment of inertia matrix and its derivative. At current, the above equations offer a significantly greater insight on how the rocket will perform throughout the course of its flight.

2.3. Stability

2.3.1. Layout of the Rocket

For the analysis, the reference line was placed at the base of the rocket. Figure 2.3 represents the preliminary layout for the rocket. While the layout was largely arbitrary, the payload was placed farther forward within the rocket because it makes up a significant portion of the weight.

The payload was placed further forward to push the CG forward and give the rocket a higher stability margin. Figure 2.3**Error! Reference source not found.** was generated using the rocket modeling software, Rocksim, which calculated the stability margin of 2.05. This is an acceptable margin of stability that is within our threshold and extremely close to the target margin.

Estimations of the center of pressure were made and verified using a team-developed Matlab script, and third party software Rocksim and RASaero. Using multiple input parameters, such as the nosecone and fin dimensions, each program was able to give us location estimate of approximately 78 inches from the nose cone, as shown in Figure 2.3. Further discussion of the theory behind the center of pressure can be found in Section 4.6.

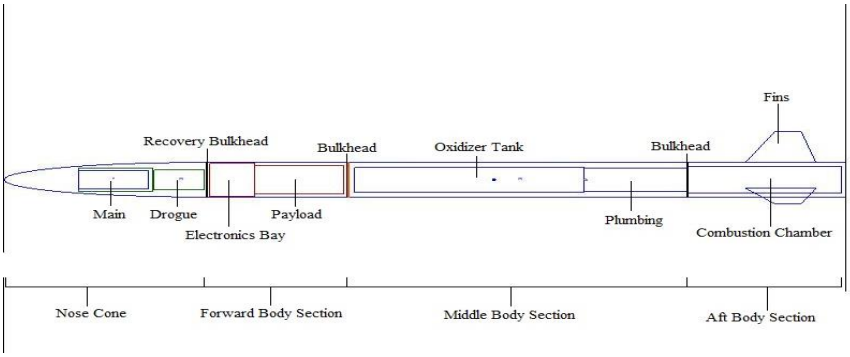

Figure 2.3. Preliminary layout of the rocket.

2.3.2. Center of Gravity

The center of gravity (CG) is defined as the point on a body that the gravitational force acts through. For this rocket, the CG was calculated using the weighted average of the CG locations of the individual components of the rocket. In Eq. 2.30[8], the value of $d_{component}$ represents the distance from the CG of each component to a reference line placed at the base of the rocket and $W_{component}$ represents the weight of the component. Equation 2.30 is given below.

$$Cg * W_{Rocket} = \sum W_{component} * d_{component} \qquad (2.30)$$

When rearranged, the formula gives the CG location for the rocket in inches with respect to the reference line.

To perform this calculation using Eq. 2.30, the component measurements and weight estimates were made. **Error! Reference source not found.** gives a list of each component and the distances used in the calculation of CG, as well as relevant dimensions that were used in the hand calculation of CG. The distances were measured from the midpoints of each individual component to the reference line.

Preliminary estimates for CG were found using Eq. 2.27. However, more accurate modeling was made available later using Solidworks. The data listed in **Error! Reference source not found.** reflects major components of the rocket with relative dimensions and weights. A complete Solidworks model produced a CG location of 69.77 inches from the nose cone of the rocket.

Table 2.1. Center of gravity distribution.

Component	Weight (lb.)	Relevant Dimensions
Fuel (tot. mass)	14.25	
Oxidizer Mass	12.25	
Solid Propellant	2.00	
Engine (All components)	30	length: 66.25 in
-Combustion Chamber	15.00	length: 21.25 in
-Oxidizer Tank	12.50	length: 31.00 in
-Plumbing	2.50	length: 14.00 in
Nose Cone (Elliptical)	1.04	length: 27.27 in., max diameter: 6.06 in
Main Parachute	2.60	
Drogue Parachute	0.60	
Payload	10.00	length: 12.00 in
Fins (3)	0.27	root chord: 9.5 in., tip chord: 3.5 in., span: 5.4in., LE sweep angle: 25°, TE sweep angle: 7.62°, NACA 65-006 airfoil
Recovery Bulkhead	1.52	
Bulkhead (2)	1.05	
Fire Resistant Panel	0.50	
Body Tube (3 sections; total weight)	3.16	total length: 85.795 in., outer diameter: 6.06 in., inner diameter: 6.00 in., density: 0.0643066 lb/in^3
-Forward Section	0.99	length: 24 in
-Middle Section	1.84	length: 44.92 in
-Aft Section	0.69	length: 16.875 in
Electronics Bay	2.00	length: 6.00 in.
Total Weight (using elliptical nose cone)	66.28	
Empty Weight	**54.03**	
Total Length		**116 in.**

2.3.3. Longitudinal Dynamic Stability

$M_{\dot{\theta}}$ is a damping moment which arises from the pitching velocity $\dot{\theta}$, as depicted in Figure 2.4. As a result of the rotation about the center of gravity, an angle of attack is induced on the aerodynamic components of the rocket (the nose and the fins on the tail). The resultant force causes a restoring moment. Because the motion opposes the disturbance, it is called a damping moment and manifests with a negative sign. Due to this restoring characteristic of the damping moment coefficient value is of utmost importance for a stable flight. Specifically, the longitudinal dynamic stability derivatives were analyzed.

For a simplified two-degree-of-freedom longitudinal dynamic analysis, with tail surfaces located near or at the end of the body, it is plausible to use Eq. 2.31 as the relation for the coefficient with respect to $M_{\dot{\theta}}$[10].

$$C_{m_{\dot{\theta}}} \approx \left\{2\left(C_{N_\alpha}\right)_b \left(\frac{x_b}{d}\right)_b^2 + 2\left(C_{N_\alpha}\right)_F \left[K_{F(b)} + K_{b(F)}\right]\left(\frac{S_{F_e}}{A_{ref}}\right)\left(\frac{x_t}{d}\right)_F^2\right\}.rad^{-1} \qquad (2.31)$$

Abbreviations in Eq. 2.31 are as follows:

- $\left(\mathrm{C_{N_\alpha}}\right)_\mathrm{b}$ and $\left(\mathrm{C_{N_\alpha}}\right)_\mathrm{F}$ are the normal force coefficients for the body and the force.
- x_b and x_t are the axial distances from rocket center of gravity to the body center of pressure and tail center of pressure, respectively.
- $K_{F(b)}$ *and* $K_{b(F)}$ are interference factors.
- S_{F_e} is the area of exposed fins in the horizontal plane.

It is important to notice that for most missiles and rockets, the tail surfaces contribute the greatest to the complete model damping. Thus, to increase stability, it is more effective to increase the distance of the fin from the CG than to increase the area of the fins.

This definition is also convenient because it is based on values which the Barrowman equations use to find the Center of Pressure, as depicted in Section 4. Further evidence is provided in Reference 10 validating this model.

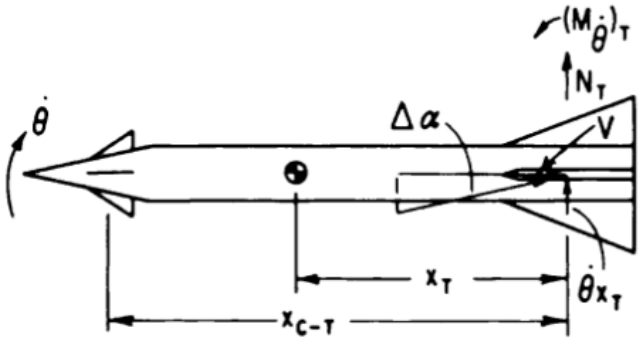

Figure 2.4. Tail contribution to damping pitch.

2.3.4. Non-linear Aerodynamics

Pitch damping is a function of C_{N_α}, the weathercock derivative, which may not be linear with the angle of attack. As a result, an assumption during the derivation for Equation 2.29 fails in precisely estimating pitch damping and thus some accuracy correction is necessary. Figure 2.5 depicts what can happen if the initial slope of C_N is used as the angle of attack is changed

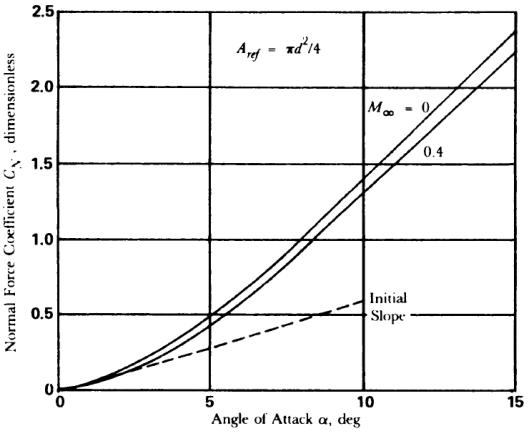

Figure 2.5. Normal Force Coefficient vs Angle of Attack.

Unfortunately, according to Reference 10, the $0 \leq M \leq 1$ range seems to be the most sensitive to this error. So it is important to consider that forequation 2.29 to remain valid the rocket cannot have a high angle of attack, which was already a necessary criterion for stability.

2.3.5. Consideration of Cant Angles

Cant angles were researched as a way to increase the overall stability. A cant angle is the angle at which the fin is offset from the rocket body as shown in Figure 2.6.

A NASA study[7] on single stage sounding rocket stability was found that explored the effects of cant angles on the flight of the rocket. The study showed that the longitudinal stability of the rocket was improved. However, it was believed that adding cant angles to the rocket would increase drag. To test this theory, a model rocket

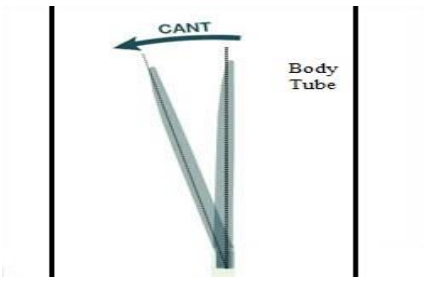

Figure 2.6. Illustration of cant angles.

with small cant angles was generated and run in Rocksim. It was found that the cant angles as small as 2 degrees caused a 10% drop in maximum altitude for multiple iterations. For this reason, the use of cant angles was abandoned.

2.4. Fin Design

When considering the fins, two driving design factors were the stability of the rocket and the reduction of drag. The stability of the rocket is primarily influenced by the geometry of the fin, such as sweep angle, root chord and span. Additionally, the drag can be substantially reduced by the airfoil choice. These design factors will be discussed further in the following sections

2.4.1. Geometry

There is not a unique geometrical solution for the fin because of several rocket properties (longitudinal stability, roll damping, stress concentration, drag) that are greatly influenced by the fin design. As a result, it was decided to utilize a simple program rather than a heavy optimization program. This program used contour plots to illustrate the value of the static margin based on a code structure from Reference 12.

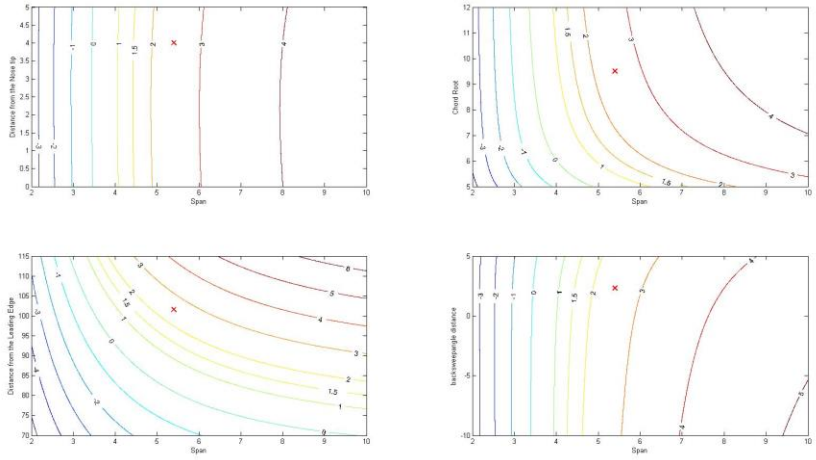

Figure 2.7. Contour plots of the static margin for different pairs of variables.

The program is a MATLAB code based on the Barrowman equations, also known as TAD (Theoretical Aerodynamics Derivatives) which is introduced in Section 4. The program used the equations for four different pairs of variables in a certain range of values, and plotted the contour lines for the Static Margin. Figure 2.7 depicts the results of this program. Through the combination of all the contour plots, choices were made based on aerodynamic factors previously mentioned. Changes were made to the initial guess and a desired result of 2.26 was obtained. The result, although satisfactory, was above the desired 1.5 Static Margin. In this case the results from MATLAB and the value of 2.2 given by Rocksim were quite close. However, since both values are within the satisfactory range for optimal stability, the configuration was considered optimal as well. The chosen geometry for the fins can be seen in Figure 2.8.

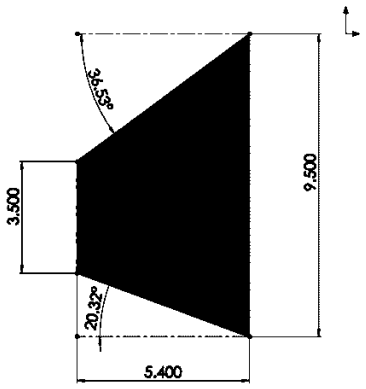

Figure 2.8. Current dimensions of the fin.

2.4.2. Airfoil

There were two initial options for the fin shape; a thin-flat plate or a thin, symmetric airfoil. With the thin-flat plates, the design would have been extremely simple. The dimensions and shape would have been relatively easy to develop for the rocket; however there would have been drawbacks. The flat edges of the fins would essentially be blunted and that would increase the drag on the rocket. Rounding the edges would help but compared to an airfoil, the drag would still be large. Ultimately, the choice for a thin, symmetric airfoil was made. This came from the fact that airfoils offered a number of advantages over the flat plates. They offered a greater amount of stability during flight and their shape allowed the rocket to correct itself in the event of a disturbance or perturbation. Airfoils also reduced the drag on the rocket significantly, allowing for faster and higher flight. With the stability from the airfoils assured, deciding on a specific airfoil shape that had low drag was the next key step.

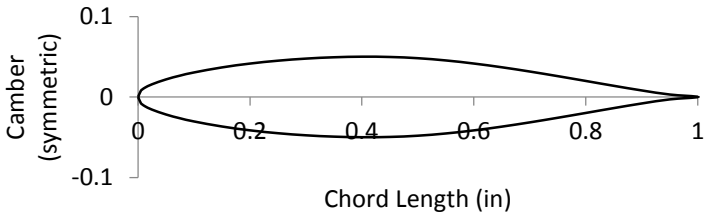

Figure 2.9. NACA 65-010 Profile[5].

Two previous rocket designs, the *Volare*[3] and *Horizon*[4], mentioned the use of the airfoil shape NACA 65-010. Research on the NACA 65-010[6] revealed that as a member of the "6-Series," the airfoil had a low drag range that was already less than one. If this were not true, there would be subscript after the number "5." The "1" in the -010 indicated that the airfoil had a ten percent thickness ratio to the root chord. The result of this would be that at the thickest point for an airfoil with a root chord of twelve inches, the thickness would be approximately 1.2". The NACA 65-010 made for a good choice given its properties and its symmetry as seen in Figure 2.9. The dimensions that were chosen at the time consisted of a root chord with a length of approximately 11.56", a span of approximately 9.27", a leading edge angle of 25° and a trailing edge angle of 7.62°.

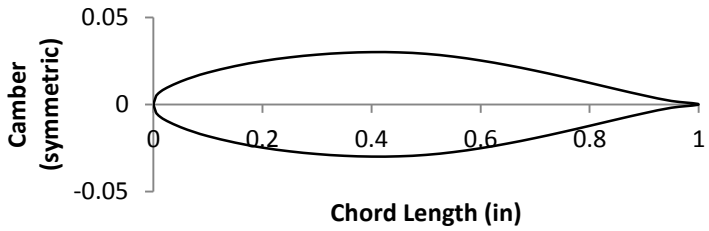

Figure 2.10. NACA 65-006 Profile[5].

However, with the initial dimensions, the thickness was considered to potentially be too thick. The static margin for the rocket with these dimensions was also very large. Reducing the drag was still a key design driver, and as such a thinner airfoil was selected. The NACA 65-006 had the same properties as the 65-010, but this particular airfoil was thinner. The thickness ratio would now be six percent of the root chord. In order to reduce the size of the static margin, the dimension of the fins would also have to change. The profile for the NACA 65-006 can be seen in Figure 2.10.

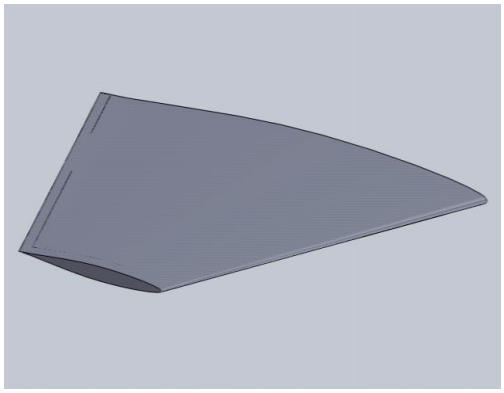

Figure 2.11. NACA 65-006 Orthographic View.

The dimensions presented in Figure 2.10 decreased the static margin to a size of two. This value was considered to be in the "safe" zone for the design parameters. The fins were designed to be hollow so as to decrease the potential mass at the tail-end of the rocket. The use of a foam core was tentatively decided upon to act as the filling for the fin. Figure 2.11 is an orthographic view of the rough model for the fin.

Further support for the NACA 65-006 was found from a NACA Research Memorandum[13] that detailed the comparison between the specified airfoil and a non-airfoil fin. The report stated that both fins were rectangular in shape and had their drag forces measured to determine which was more aerodynamically efficient. In Ref. 13, the non-airfoil fin (described as a symmetrical circular-arc with a similar thickness) had a greater amount of drag than the NACA 65-006, by approximately 16% at transonic speeds and 11% at supersonic speeds. Based on this information, the NACA 65-006 was deemed the appropriate choice for an airfoil due to its low drag range.

Ultimately, the NACA 65-006 airfoil proved to be an optimal choice for the fin design. The dimensions that are currently being used were also optimized and as such, the design was considered to be sound. The next step for the fin design process will be to refine the method in which the fins will be attached to the rocket. The current method will be to attach use an epoxy coating to attach the fin as well as using an overlay of carbon fiber.

2.4.3. Amount of Fins

From the Figure 2.12, we can observe that the amount of fins which lead to the least amount of drag is 3. Although it makes our Inertia calculations more complicates, due to the speed time of the calculations, its benefits were found to be worth the effort.

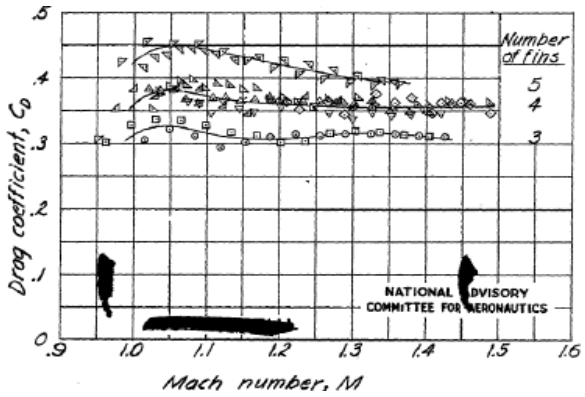

Figure 2.12. Drag coefficient for different fineness and designs.

2.5. Computer Modeling

The goal of a numeric methods computer model of our rocket was to get an accurate estimation of the rocket's performance given certain design parameters and launch conditions. Accurate estimations could then be used for design revisions as necessary to fulfill mission objectives. The computer model of the rocket was created in MATLAB, under ideal conditions using a one dimensional motion point mass model and utilizing Eq. 2.32.

$$\dot{v} = \frac{1}{m}\left(Thrust - mg - \frac{1}{2}C_D \rho A v^2\right) \qquad (2.32)$$

The simple differential equation is evaluated using the Runge-Kutta method in MATLAB for both burn and coast phases, and finds the burn time required to hit 10,000 feet. Burn time is calculated by running the script for several iterations and varying the burn time from an initial estimate until the altitude reached by the rocket varies by less than one foot from the previous iteration. The last iteration's burn time is the burn time returned. The program also returns graphs for height, velocity, and acceleration versus time. The results derived from the model are very similar to values calculated using the third party software Rocksim 9. The results and values are shown in Table 2.2 and Figure 2.13. The thrust equation and mass flow rate equation are given by Equations 2.33 and 2.34, respectively. These equations were derived by fitting a fourth order polynomial to engine data.

$$T = -0.0036t^4 - 0.1385t^3 + 0.5641t^2 - 13.669t + 330.61 \qquad (2.33)$$

Table 2.2. Values used in MATLAB Rocket Model and Results

Initial Launch Height	4,355 ft
Target Height	14,355 ft
Rocket Weight	51.98 lbs
Fuel and Oxidizer Weight	14.25 lbs
Thrust Max	330.61 lbf
Coefficient of Drag	0.4
Acceleration due to Gravity	32.185 ft/s
Diameter	6.06 in
Results	
Burnout Time	7.36 s
Max Velocity	775.4 ft/s

$$\dot{m} = 0.0002t^4 - 0.0046t^3 + 0.0406t^2 - 0.1665t + 1.6361 \quad (2.34)$$

The rocket is calculated to burn for 7.36 seconds and reach a max velocity of 775.43 feet/second at burnout, expending about 10 pounds of propellant. Apogee is reached shortly after 27 seconds at 14,355 feet ASL. If all fuel is burnt, the rocket burns for 8.58 seconds and reaches a max altitude of over 17,000 feet ASL, leaving room to adjust the burn time to compensate for approximations and weather effects.

There is some inherit error when using this model, as this is a one dimensional rocket launch, and the actual launch will be at an angle of five degrees. The model assumes that an initial five degree angle is negligible, and while false, it provides an accurate representation of whether or not the rocket is capable of reaching the goal height. In addition to the angling, wind conditions and humidity on the day of launch will significantly impact the way the rocket flies. Weather conditions are neglected in the simplistic model because they are unpredictable. While there are very few rocket parameters in the model that haven't been estimated with a large degree of accuracy, imperfect construction of the rocket and further changes to the design can reduce the model's accuracy. More accurate computer models are being developed to incorporate multiple dimensions, stability, and weather conditions, as they are vital to the simulation but difficult to incorporate into a model.

Given the error, however, the MATLAB model produces very similar flight results to the Rocksim 9 commercial rocket simulator when given the same initial launch values and angles. Comparison of the MATLAB model with Rocksim 9 under other various conditions also proved Rocksim 9's accuracy, and validated it as a useful tool for value confirmation during the design process.

A one dimensional point mass model was utilized for ease of calculation, and would allow for a fairly accurate representation and estimation of how the rocket will perform. The values used in the model were close approximates to design values for several of the rocket's parameters. For the model, thrust and mass flow rate were approximated from engine data using a polynomial. In addition, gravity was assumed to be constant and the coefficient of drag was calculated from SolidWorks. Also, the density of air was approximated for different altitudes and the diameter of the

rocket used in computational methods was the same diameter of the rocket design. Friction over the length of the launch rail was neglected, and it was assumed there is no launch angle in one dimensional analysis.

The computer model of the rocket went through several iterations before arriving at the current version used to estimate the rocket performance. The original scripts took preliminary estimates of possible rocket parameters and attempted to solve for any remaining unknown values (i.e.- average thrust, burn time, and fuel mass). As the results

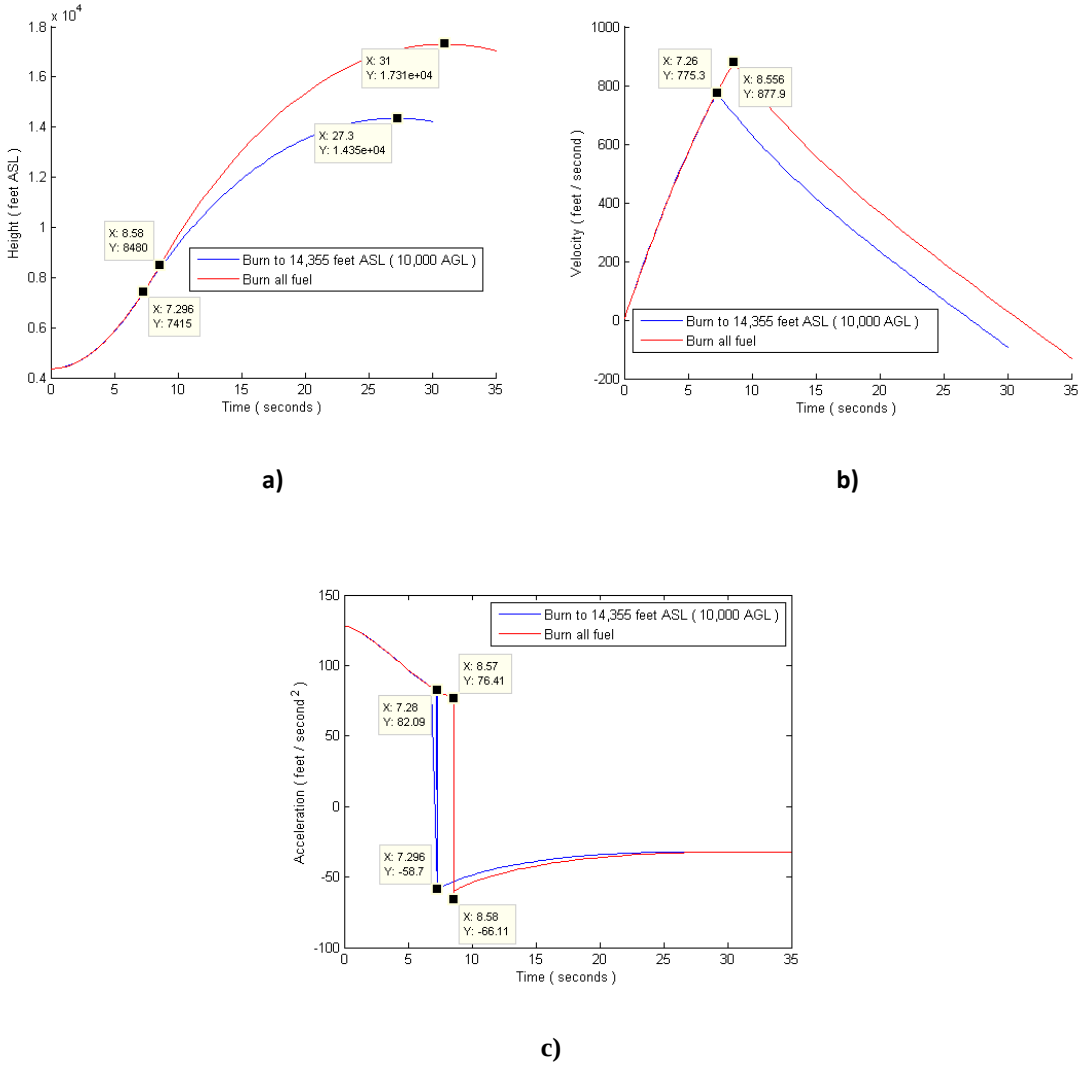

Figure 2.13 a) Height as a Function of Time b) Velocity as a Function of Time c) Acceleration as a Function of Time

of the model were analyzed and refined, more accurate estimations of rocket parameters could be used, which in turn brought the model closer to the desired rocket design. After thorough examination, many estimates were replaced with designed values, bringing the model to the current version.

2.5.1. Rocksim

Rocksim is an aerodynamic simulation software specifically for rockets. The software is licensed by Apogee Components, a rocketry component supplier based out of Colorado Springs, Colorado.

The software uses different variations of the Barrowman stability equations, as well as many of its own algorithms for determining stability and trajectory. The calculations are based on rocket dimensions, inputted atmospheric conditions, starting state, and thrust.

A major advantage of using Rocksim is that it saves time. Many variables change during the design process. Having a computer program work through the calculations with new inputs allows the team to analyze the results and quickly make recommendations. Rocksim's algorithms have been tested by thousands of users, and have been proved to be very accurate. This allows the team to able to make very strong estimations on almost every aspect of the flight of the rocket, which increases reliability and safety on launch day.

2.5.2. Simulation Verification

Simulations to verify the validity of the MATLAB model were done by the Rocksim 9 software. Table 2.3 shows the data processed by the software and the outputs. The input launch angle, C_d, and burn time were the same used in the MATLAB model, along with the same thrust curve. Given these parameters, Rocksim generated a projected altitude of 9,870.96 ft. and a max velocity of 757.28 ft/s. It should be noted that the gravity is not constant in Rocksim's calculations. Gravity starts at 32.075 ft/s^2 in the Rocksim model, which accounts for the discrepancy between Rocksim and MATLAB model.

Table 2.3. Verification Data

Launch Angle	0 Degrees
Cd	0.4
Burn Time	7.36 s
Projected Altitude	9870.96 ft
Velocity	757.28 ft/s

2.5.3. Independent Simulation

To obtain a more realistic prediction for the day of the launch, Rocksim was run with all capabilities enabled. Previously, certain functions of Rocksim were turned off to align more precisely with the MATLAB model for verification. For this simulation, the launch angle was set at 5 degrees and the coefficient of drag was left to the Rocksim calculation algorithm. The projected altitude during this simulation increased to 10,746.52 ft. The increase in altitude from the MATLAB verification simulation is attributed to the lower C_d, maxing out at 0.305, as calculated by the software's algorithm.

Table 2.4. Full Prediction

Launch Angle	5 Degrees
Cd	Max 0.305
Burn Time	7.36 s
Projected Altitude	10746.52 ft
Velocity	782.87 ft/s

2.6. References

[1]Anderson, John., *Introduction to Flight*, 7th ed., McGraw-Hill, 2011, Print.

[2]Hennin, Bart., "Why Should You Airfoil Your Rocket's Fins?," *Peak of Flight*., 31 Jan. 2012, URL: http://www.apogeerockets.com/downloads/Newsletter305.pdf [cited 8 November 2013].

[3]Benson, Andrew., "Volare: Spring-Fall 2010 Senior Design Project Final Report," 2010.

[4]Bennett, Trevor., "Horizon Aerospace Final Report," 2012.

[5]Carmichael, Ralph., "Public Domain Aeronautical Software," *Appendix 1 – Tables of Profiles*., 2010, URL: http://www.pdas.com/profiles.html [cited September 2013].

[6]Abbott, I., Von Doenhoff, A., and Stivers, L., "NACA Report No. 824: Summary of Airfoil Data," *NASA Technical Report Server*, National Aeronautics and Space Administration, 01 Jan. 1945, URL: http://naca.larc.nasa.gov/search.jsp?R=19930090976&qs=N=4294868711+4294448803 [cited 8 November 2013].

[7]Ferris, James, "Static Stability Investigation of a Single-Stage Sounding Rocket At Mach Numbers From 0.60 To 1.20", *NASA Technical Note D-4013*, Washington, D.C., 1967, pp. 8.

[8]Benson, Tom, "Rocket Center of Gravity," *Rocket Center of Gravity* [web page], URL: http://exploration.grc.nasa.gov/education/rocket/rktcg.html [cited 07 November 2013].

[9]RASAero, RASAero Aerodynamic Analysis and Flight Simulation Software, Software Package, Ver. 1.0.2.0, Rogers Aeroscience, Lancaster, CA, 2011.

[10]S. S. Chin, *Missile Configuration Design*, McGraw-Hill Book Company, Inc., New York, NY, 1961,pp. 130-53.

[11]Effect of Number of Fins on the Drag of a Pointed Body of Revolution at Low Supersonic Velocities; Mastrocola, N; NACA Research Memorandum L7A08; 1947.

[12]Ng, Andrew, "Machine Learning", Coursera online course.

[13]Thompson, Jim Rodgers, and Marschner, Bernard W., "Comparative Drag Measurements at Transonic Speeds of an NACA 65-006 Airfoil and a Symmetrical Circular-Arc Airfoil," *NACA Research Memorandum*, National Advisory Committee for Aeronautics, Washington, 06 Mar. 1947, pp. 1-9 URL: http://www.dtic.mil/dtic/tr/fulltext/u2/a801141.pdf [cited 14 January 2014].

[14]Rocksim, Rocksim Version 9 Apogee Components, Colorado Springs, CO, 2009.

3. Engine

3.1. Objective

The objective of the engine is to provide the required thrust as laid out by the theoretical trajectory. In order to do this, a variety of different fuels were analyzed along with a handful of oxidizers to find a combination that was cheap, efficient, and as safe as reasonably possible. From the onset, the propulsion team's main endeavor was to provide more thrust than necessary without exceeding the worst-case weight limit of 70 lbs. The engine is also designed to be reproducible, thus allowing a predictable thrust-time curve given specific initial conditions. By doing this, the engine will be programmed to shut off at a predetermined time, eliminating the need to precisely measure the amount of oxidizer put into the tank and allowing an accurate coast to altitude.

3.2. Oxidizer and Fuel

The oxidizer for the rocket was chosen to be nitrous oxide (N_2O) due to its stability at room temperature and its easy availability. The handling of nitrous oxide will be much safer than that of other potential oxidizers, such as liquid oxygen, because of its stability, nontoxic properties, and lack of need for a completely clean environment. Furthermore, nitrous oxide has been used extensively in hybrid rocket motors in the past, so there is a lot of information on its storage, filling, and use. Although N_2O is relatively stable, it is an oxidizer, which by nature means it is highly energetic. This means that it can be extremely dangerous if handled incorrectly. Nitrous oxide must be remotely operated when filling or draining. It must be pressurized, so that it stays in the liquid phase. Also, nitrous oxide's density changes significantly with temperature, as indicated in Table 3.1, so tanks should not be filled completely. The team is leaving 5% empty, which ideally should be more, but the volume is needed for a successful launch to altitude. Nitrous oxide's density variation with temperature is concerning considering there are no on-board cooling or heating units. Although there is an idea of what the temperature will be like on the day of the launch from data obtained from the farmer's almanac, there is no way to be entirely sure. For the rocket's design, a worst case scenario temperature of 85° F is assumed.

Table 3.1. Nitrous oxide properties at different temperatures.

Temperature degrees. C.	Vapour Pressure Bar Abs	ρ_{liquid} kg/m^3	ρ_{vapour} kg/m^3
—20	18.01	995.4	46.82
—15	20.83	975.2	54.47
—10	23.97	953.9	63.21
—5	27.44	931.4	73.26
0	31.27	907.4	84.86
5	35.47	881.6	98.41
10	40.07	853.5	114.5
15	45.10	822.2	133.9
20	50.60	786.6	158.1
25	56.60	743.9	190.0
30	63.15	688.0	236.7
35	70.33	589.4	330.4
T_{crit} 36.42	**72.51**	**452.0**	**452.0**

Different fuels were researched using the program Propep GDL to determine the flame properties of each reaction. The flame temperature, specific heat ratio, and average molecular weight were calculated at varying oxidizer-to-fuel ratios and a constant chamber pressure of 300psi. Each of these values contributes to the total possible thrust that the rocket can experience. Equation 3.1 describes the average exhaust velocity as a function of combustion chamber pressure, p_1, the specific heat ratio of the gas, γ, the adiabatic flame temperature, T_1, and the average molecular weight, M, as acting through the specific gas constant shown in Equation 3.2. The expanded nozzle pressure, p_2, was found by assuming a constant Mach number of 2.5, though this number was used just for comparison during preliminary

fuel selection. Using the isentropic relations in Equation 3.3 and the specific heat ratio, the pressure ratio could be solved for, thus eliminating the dependence of Equation 3.1 on the chamber pressure.

$$v_2 = \sqrt{[2k/(k-1)] * R * T_1[1 - (p_2/p_1)^{(k-1)/k}]} \quad (3.1)$$

$$R = R_u/\hat{M} \quad (3.2)$$

$$\frac{p_2}{p_1} = \left(1 + \frac{\gamma-1}{2}M^2\right)^{\frac{-\gamma}{\gamma-1}} \quad (3.3)$$

The lack of chamber pressure dependence in Eqs. 3.1-3.3 does not mean that the chamber pressure does not influence the system. In fact, the above process is incorrect in a number of different ways. First, the average exhaust velocity is only one term in the thrust equation. Equation 3.4 represents how thrust is dependent on the exit pressure, atmospheric pressure, mass flow rate, and exit area of the nozzle. For this exercise, the pressure differential in the second term was decided to be zero, since a nozzle geometry had not been decided. This allowed the second term to disappear and the function became a function of only mass and exit velocity. Since the goal of the analysis was to determine the fuel with the most thrust, mass was assumed to be one in order to get the best possible thrust per unit weight. This analysis is similar to calculating the specific impulse, as rearranged in Equation 3.5, but instead neglecting the gravity constant and taking the thrust in vacuum.

Using a constant Mach number is also misleading in the sense that each gas composition will have a specific optimally expanded nozzle area and the maximum thrust will correspond to different Mach numbers. This will be further discussed in Section 3.5.

$$F_t = \dot{m}V_e + (P_2 - P_a)A_e \quad (3.4)$$

Ultimately, the chamber pressure is one of the major design factors in the engine. When using Propep GDL, changing the combustion chamber pressure changes the exhaust characteristics very little, except for the major jumps in temperature. This is evident if one considers the ideal gas law, where, since the volume does not change and mass must still be conserved, the average density and the specific gas constant do not change. In this scenario an increase in pressure results in an increase in temperature. One of the other major factors the chamber pressure contributes to is making sure the nozzle maintains choked flow. As Section 3.5. will outline, the pressure inside the chamber must maintain a specific ratio with the atmosphere in order to properly expand. If this fails to occur, then the average exhaust velocity, and consequently thrust, drops exponentially.

Numerous different fuels were analyzed with Propep GDL and the Eqs. 3.1-3.3, yielding a comparison in the average exhaust velocities. However, this method became fairly unhelpful given that a temperature of 3000 K was a design constraint for the materials being used and the peak temperatures of the reactions went well beyond this number. Using the maximum temperature for each fuel, Propep GDL gave an optimum effective exhaust velocity, c, and specific impulse which was used to compare each fuel more accurately than the previously mentioned exercise.

After the initial analysis of approximately fifteen different fuels, they were gradually eliminated to a choice of three: nylon-6, paraffin wax, and hydroxyl-terminated polybutediene (HTPB). Their given performance, cost, oxidizer-to-fuel ratios, density, as well as previous experience of the materials were all taken into account in selecting the fuel. As displayed in Table 3.2, Nylon 6 has a higher specific impulse than the other two options, a lower total mass, and the lowest oxidizer to fuel ratio, which is preferred because it would require a smaller oxidizer tank. This seemed to be a clear choice, but the high density of Nylon 6 meant that a very small grain would be needed, posing a problem in keeping the oxidizer flux area larger than the nozzle throat. Because of the problems posed by manufacturing and the size of the grain, it was determined to rule Nylon 6 out. Paraffin wax yielded similar results to HTPB, but the oxidizer to fuel ratio was too high for the propulsion team to recommend as well as a very high regression rate and very low melting point. In the end, HTPB was selected due to a good track record with previous AERO 401/402 classes and promising numbers. The maximum specific impulse for HTPB just at the highest tolerable temperature and a chamber pressure of 300psia was 225.3 sec, resulting in an oxidizer-to-fuel ratio of 4.5:1. Using the average thrust (315.74 lbf) needed to propel the rocket to 10,000 ft and a 10 second burn time, the mass of the fuel required was determined to be 14.01 lbs, where ṁ is the mass flow rate of the oxidizer and fuel, F_{thrust} is the average thrust, I_{sp} is specific impulse and g is the acceleration of gravity.

Table 3.2. Comparison between the final three fuels.

	HTPB	Nylon-6	Paraffin
Ox-Fuel Ratio	4.5:1	3.5:1	5.8:1
Effective Exhaust Velocity (ft/s)	7254.7	7512.2	7367.36
Specific Impulse (s)	225.3	233.3	228.8
Fuel Mass (lbs.)	2.55	3.00	2.03
Oxidizer Mass (lbs.)	11.46	10.53	11.77
Total Propellant Mass (lbs.)	14.01	13.53	13.80
Density (lbs./ft^3)	58.06	71.17	56.19
Price ($/lb)	6.67	2.27	5.30

$$\dot{m} = \frac{F_{thrust}}{I_{sp} g} \tag{3.5}$$

Since the oxidizer-to-fuel ratio will be changing throughout the duration of the burn, the relationships between the flame temperature, specific heat ratio, and average molecular weight were characterized for HTPB and are represented in Figure 3.1.

Extra solid fuel will be added to burn fuel rich, even though fuel lean is preferable. The reason it was chosen to burn fuel rich is to protect the combustion chamber, and subsequently the body tube, from being burned through. A lot of these factors, such as surface area, regression rate, and flux change with time. The surface area can somewhat be held constant with different port designs as the fuel regresses, or it can change drastically. This change in surface area leads to a change in the thrust curve.

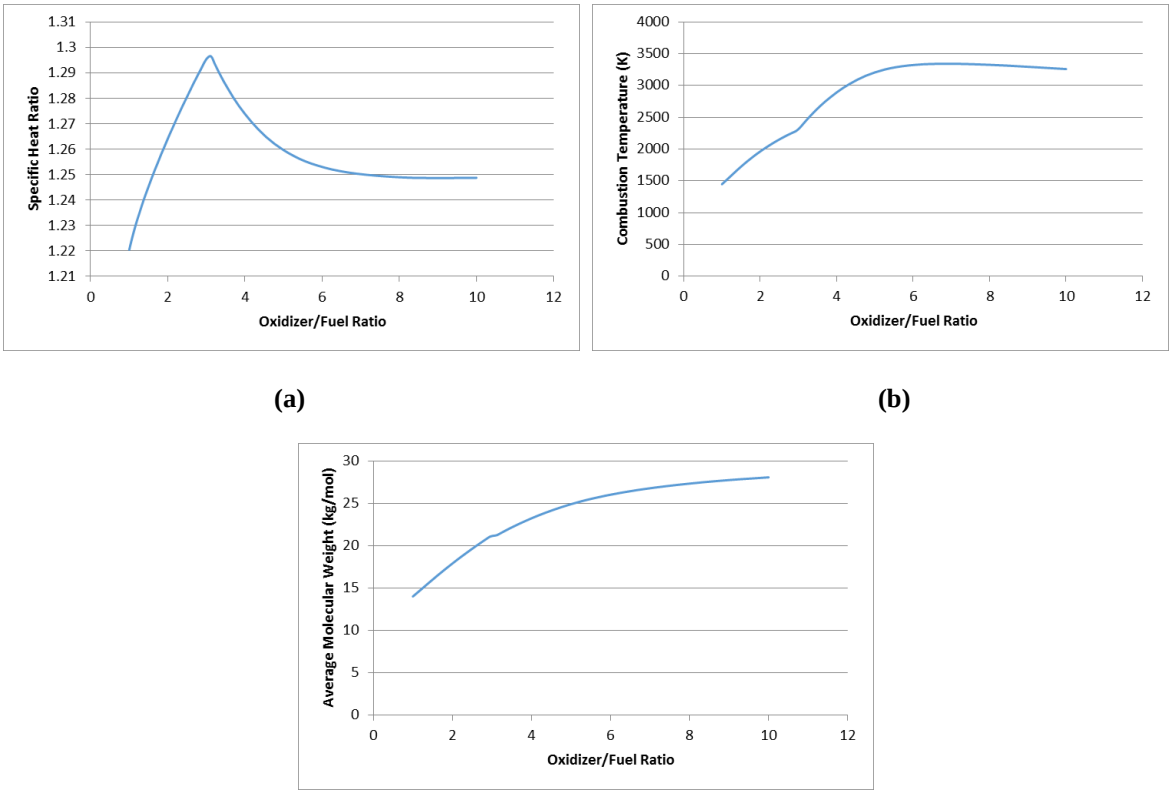

Figure 3.1. (a) Specific heat ratio versus O:F ratio, (b) Combustion temperature (Kelvin) versus O:F ratio, (c) Average molecular weight versus O:F ratio.

The mass flow rate of the fuel is calculated by utilizing Eq 3.6 where A_S is the surface area of the port, and ρ_f is the density of the propellant.[1]

$$\dot{m}_f = A_S \rho_f \dot{r} \tag{3.6}$$

A relationship between regression rate and the flux of the oxidizer was found to be:[1]

$$\dot{r} = 9.3368x10^{-8} G_{ox}^{1.6386} \tag{3.7}$$

Using Eqs 3.5-3.7, a regression rate of 0.069 in/s, a documented experimental value[2], an I_{sp} of 224 s, and a thrust of 315.74 lb_f, the flux, port area, port length and surface area can all be calculated. Using the recessed Rising Sun port shown in Figure 3.2, the results were calculated and are displayed in Table 3.3.

Table 3.3. Initial fuel grain specifications based on required thrust.

Regression Rate (in/s)	Oxidizer Flux ($lb/in^2/s$)	Port Area (in^2)	Surface Area (in^2)	Port Length (in)
0.069	0.7046	1.626	109.152	15

The initial specs of the fuel grain were used to create a regression profile, which tries to predict the geometric behavior of the port over the course of time. This then, coupled with the transient analysis of the oxidizer mass flow rate, can be used to solve for a thrust-time curve. The recessed Rising Sun port was chosen due to its larger surface area per length and its surface area changing at a slower rate than other ports.

In order to calculate the port area for this design, the area was modeled as two concentric circles with eight evenly spaced trapezoids inserted between them. The area was calculated by subtracting the eight trapezoidal areas from the area of the bigger circle. This is shown in Equation 3.8 where A_{port} is the area of the port, r_{outer} is the larger circle's radius, and A_{trap} is one trapezoidal area. The trapezoidal area is calculated as shown in Equation 3.5 using basic geometry where the bases are found as arc lengths of the inner and outer radii for a constant angle of 22.5 degrees. The regression rate, ṙ, varies with time and is a function of oxidizer flux as referenced in Equation 3.7. The inner and outer radii change according to the regression rate at that point in time. The inner radius changes at a full value of the regression rate, but the outer radius will change at a slower rate, which is not known. The two change at differing rates because the fuel grain closest to the center will be exposed to more oxidizer and a hotter flame. That rate is estimated as a "regression rate correction factor" in the calculation of the change of the outer radius. This relationship is shown in Equation 3.10, where h is the height of the trapezoid, and X represents the regression rate correction factor. The regression rate correction factor used in the calculations was determined to be 0.2 through trial and error. The data output from the transient analysis code was analyzed and the correction factor was changed until discontinuities in thrust and mass flux data were minimized.

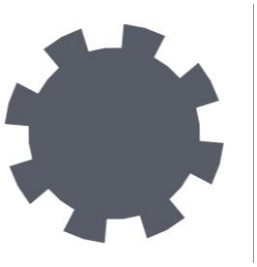

Figure 3.2. Recessed Rising Sun port configuration.

$$A_{port} = \pi r_{outer}^2 - 8 * A_{trap} \quad (3.8)$$

$$A_{trap} = [(r_{inner} * 22.5 - 2 * \dot{r} * \Delta t) + (r_{outer} * 22.5 - 2 * \dot{r} * \Delta t)] * h/2 \quad (3.9)$$

$$h = (r_{outer} - r_{inner})\, cos(22.5) - X * \dot{r} * \Delta t \quad (3.10)$$

3.3. Combustion Chamber

The combustion chamber consists of three parts: the pre-combustion, combustion, and post-combustion stage. The pre-combustion stage allows the oxidizer to expand into turbulent flow after leaving the injector[2]. This is important so that it creates a boundary layer across as much of the surface area of the fuel grain as possible in order to obtain an even burn. The combustion chamber will be where the fuel grain is stored and reacts with the oxidizer. The post-combustion chamber is necessary to ensure a complete mixing and combustion of the two fuels.

The size of the pre-combustion chamber was determined by first using the angle of impingement of the injector plate's holes to find where the four streams of oxidizer will meet inside of the combustion chamber. Flowsim was then used for a few different cases of how far away the fuel grain should be from the injector plate to find the case

which produces the most turbulent flow. After these simulations, it was determined that the pre-combustion chamber would have a length of 1.125 inches.

The volume of the combustion chamber can be calculated using Equation 3.11 where V_c is the chamber volume, q is the propellant mass flow rate, v is the average specific volume, and t_s is the propellant stay time[2]. Since the cross sectional area of the combustion chamber remains constant, the length required for the combustion chamber can be acquired by finding V_c. Stay time must be found experimentally, so results from past experiences of the senior design class will be used to estimate stay time of HTPB when reacting with N2O. If a stay time of 0.12 seconds is taken to be near correct, then dimensions described later in this section along with a mass flow rate of 1.57 pounds per second, given by the dynamics team, and an average specific volume of 0.0065 cubic feet per pound can be used to yield a post-combustion chamber length of 0.6 inches, but the post combustion chamber will be 0.5 inches because it was determined that post combustion chamber that was too short would be preferable to one which was too long.

$$V_c = q * v * t_s \tag{3.11}$$

The combustion chamber assembly will consist of three main pieces; an aluminum outer tube, an insulating tube, and the fuel grain. The insulating tube is needed to protect the outer, load bearing tube from the high temperatures experienced in the combustion chamber. Phenolic tubing was considered for this purpose because it is easily obtainable and has been used reliably before. The phenolic tubing is 0.125 inches thick, and based upon available sizes, has an inner diameter of 2.75 inches. The three different kinds of phenolic considered were G-7, G-10, and G-11. After getting quotes for these products, however, alternative insulators were sought. Cost was an important factor because a new section of phenolic will be needed for each engine since the fuel grain will be cast inside of the insulation. One very promising substitute was silica. Table 3.4 is a table of the materials' costs and properties which pertain to the analysis. As evidence by the information contained within the table, silica far exceeds the phenolic tubes in every way. One thing not mentioned though is the silica sheet's lack of rigidity. This problem was solved by using a thicker sheet (0.25") and possibly casting it in a high temperature epoxy. Graphite inserts will be used at the pre and post combustion chambers, and an extra thickness of solid fuel will be casted inside of the silica to keep the sheet from melting and further protect the outer tube from the combustion process.

Table 3.4. Property comparison of phenolics and silica.

Classification	**Phenolic**			**Silica**
Type	G-7	G-10	G-11	N/A
Max Operating Temp (°F)	430	284	329	2000
Thermal Conductivity (BTU-in/ft^2-hr-°F)	2.0	2.0	2.0	0.78
Coefficient of Linear Thermal Expansion	0.90	0.66	0.83	0.55
Cost (USD/foot)	61.15	37.75	38.82	6.05

The outer tube is the main pressure bearing tube, and it will also serve as a means to connect the lower engine assembly to the body of the rocket. Aluminum 6061 was chosen for this piece because of its high tensile strength, low weight, availability, and machinability. The inner diameter of this tube was determined based upon available outer

diameters of the insulating tube being used. A 0.25 inch thickness was available for an inner diameter of three inches. Solving for hoop stress using Eq 3.12 where σ_θ is hoop stress, p is pressure, r is radius, and t is the thickness of the chamber, at a pressure of 300 psi, and given the dimensions of our tube (3 inch inner diameter and 0.25 inch thickness), the pressure that the aluminum will encounter is much lower than its maximum allowable pressure and yields a safety factor of 16.7.

$$\sigma_\theta = \frac{p*r}{t} \tag{3.12}$$

In order to connect the combustion chamber to the liquid fuel injector and the bulk head, a 0.75 inch thick flange will be welded to the aluminum tube to extend the outer radius to 5.875 inches, and holes will be drilled from the top of the flange as well as threads drilled into the sides. The injector will connect to the combustion chamber by bolting the pieces together from the top, and the bulk head will be connected by screwing a bolt in through the side of each piece. Keenserts will be used for the pieces being screwed into place in order to avoid wearing down the threads placed in the aluminum. The bottom of the combustion chamber will connect to the nozzle and the bulkhead in the same way, except no holes are needed in the side of the flange, allowing the thickness to be reduced to 0.625".

3.4. Injector System

In a hybrid rocket engine, the injector serves as the main interface between the oxidizer tank and the combustion chamber. The purpose of an injector is to provide a pre-determined oxidizer mass flow rate to the combustion chamber. The engine's total mass flow rate and its time dependence is what will determine the engine's thrust-time curve. An effective injector introduces a liquid oxidizer into the combustion chamber with a speed and trajectory that generates enough turbulence to ensure that it reacts with the entire fuel grain. Another criterion the injector will need to meet is the ability to withstand both dynamic temperatures and pressures due to the pressurized nitrous oxide flowing through it as well as the heat emanating from the combustion chamber beneath it.

The injector consists of two main parts: an injector plate and an injector plate holder, both of which are made of aluminum 6061, as shown in Figure 3.3. (a) The removable injector plate will slide into the holder and will seal with the holder utilizing a male O-ring located on the upstream side of the injector plate as seen in Figure 3.3. (b). Originally the injector plate was going to thread into the holder, but that design was eliminated because it would require an expensive 360 brass plate to prevent galling and also because it would be extremely difficult to machine threads inside the holder. To solve the problem of the aluminum welding together in the presence of extreme heat radiation, the new plate will incorporate a radial silica insulation sheet to protect it from direct contact with the holder.

Additionally, the plate will feature a set of three radially symmetric angled holes and a single center hole. The purpose of the center hole is so that the mass flow rate of the injector can easily be increased by drilling this single hole out larger without disrupting the symmetry of the pattern. The four holes will impinge the oxidizer at a point inside the pre-combustion chamber 1/8 in above the fuel grain. This will create a turbulent nitrous oxide flow field inside the fuel grain which will ensure that the nitrous oxide atoms come into contact with the walls of the fuel grain before they exit the nozzle. The injector holder serves two functions: to house a reservoir of above the plate to ensure

an even nitrous oxide pressure across each injection orifice and to serve as a way to mount the injector plate to the lower engine assembly.

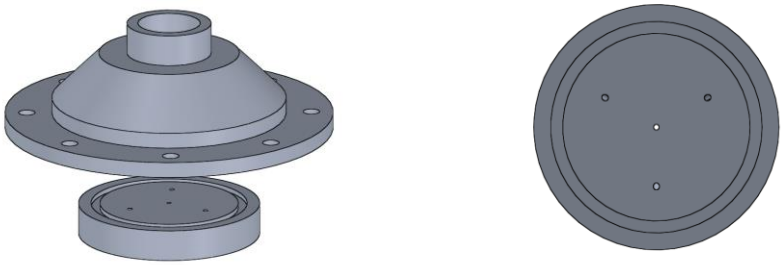

(a) **(b)**

Figure 3.3. (a) Exploded view of the Injector (b) Upstream side of Injector Plate.

The rocket's injector orifice size was calculated using two different approaches. The orifice size was initially determined through the direct use of Eq. 3.13. which can be derived using a combination of Bernoulli's equation and the continuity equation.

$$\dot{m} = AC\sqrt{2\rho(P_1 - P_2 + a\rho z)} \qquad (3.13)$$

In Eq. 3.13. $\dot{m}$ is the oxidizer mass flow rate which will be steadily falling as the vapor pressure of the nitrous oxide falls, the term "A" represents the total area between all of the injection orifices, "a" is the acceleration of the rocket which is assumed constant at an average value, "z" is the "hydrostatic head," P_1 and P_2 are the tank and combustion chamber pressures respectively, ρ is the density of nitrous oxide which is also taken to be constant, and "C" is a flow coefficient that accounts for flow losses through the plate due to friction. According to one of Dr. Pollock's PowerPoint's on injectors, a reasonable range for the flow coefficient is anywhere from 0.35 to 0.55. For the initial design it was assumed that C= 0.55 and a worst case scenario of 85° F to underestimate the orifice size. A chart listing the densities of nitrous oxide at different temperatures can be found in Table 3.1. Using Equation 3.13 and the assumption that C= 0.55, it was determined that each hole of the injector would need to have a diameter of 0.045" to achieve an initial combustion chamber pressure of 300 psi. For purposes of a static engine test, the $a\rho z$ was ignored because it will be zero, but the team will anticipate this extra induced pressure when launching the rocket.

After a static firing of the engine, the actual value of C will be calculable. At this time the center orifice area will be adjusted to more closely produce the rocket's target thrust. The second way the orifice size was determined was through the use of a Matlab code that the team has spent the previous semester developing and will be discussed in further detail in section 3.7. This code provides a transient analysis on the combustion process of the engine and therefore provides a more accurate orifice size. Without going into too much detail, the iterative code is able to determine instantaneous mass flow rates by focusing on the heat removed from the liquid nitrous oxide as the tank empties. The program only requires an initial nitrous oxide temperature to run. Using this code it was found that each

orifice would need to be about 0.0725” in diameter in order to produce an initial oxidizer flow rate of 1.25 lbm/s and the teams’s target initial thrust of 350 lbs. in Utah. This size hole will require a number 49 drill bit which is 0.073”.

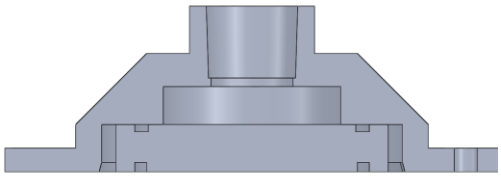

Figure 3.4. Section view of injector system.

In order to generate the largest amount of turbulence, it has been determined that the angle of impingement with respect to the face of the injector plate should be 64˚based on the location of the pre-combustion chamber and the diameter of the plate.

3.5. Nozzle

This section details the design specifications for the nozzle of the rocket. The topics covered will be the purpose of the nozzle, a technical description of how the nozzle was designed, and finally a description of the proposed parameters and specs to be used on the rocket.

The nozzle of the rocket can be said to be the final stage of the entire propulsion system. The propellants are fed from their respective tanks at a specified thermodynamic state and fuel/oxidizer ratio into the combustion chamber. Upon leaving the combustion chamber, the mixed propellants are then fed into the nozzle. At this stage, the nozzle acts to convert the high pressure of the propellants into high kinetic energies at the nozzle exit, which results in a net force (termed as thrust) in the direction opposite to the propellant flow. Overall, the nozzle can be said to have the purpose of converting the high energy content of the pressurized propellants to produce the thrust for the launch vehicle.

To achieve supersonic flow at the exit of the nozzle, a Converging-Diverging (CD) nozzle must be implemented. This fact is a direct result of the following equation:

$$\frac{dP}{dA} = \left(\frac{\gamma M^2}{1-M^2}\right)\frac{P}{A} \qquad (3.14)$$

where A is the area, P is the pressure, M is the Mach number, and γ is the ratio of specific heats. It should be noted that this equation assumes an isentropic flow condition. As can be seen from the equation, if the Mach number of the flow is less than one, the infinitesimal change of the pressure with respect to the area is positive. Since decreasing the pressure increases the velocity of the flow, this shows that the velocity of subsonic flow can increase with a decreasing area, i.e. a converging nozzle. However, in the case of supersonic flow, the equation shows just the opposite. The end

result is that sonic flow can only be sped up by increasing the area. Hence, the objective of a CD nozzle is to increase the velocity of subsonic flow to speeds well above the speed of sound.

The first step taken in the nozzle design process was to find the correct areas at the throat and exit of the nozzle to produce the desired amount of thrust. To accomplish this, the mass flow rate, stagnation temperature T_0, stagnation pressure P_0, and specific heat ratio γ are required. Equation 3.15 shows the relation between these parameters and the throat area that is required for choking (A*).

$$\dot{m}_{max} = P_0 A^* \sqrt{\frac{\gamma}{RT_0}} \left(\frac{2}{\gamma+1}\right)^{\frac{\gamma+1}{2(\gamma-1)}} \tag{3.15}$$

where $\dot{m}_{max}$ is the maximum flow rate, i.e. the flow rate at choked conditions. The specific heat ratio is a function of the propellants used, as well as the OF ratio, and was determined to be approximately γ=1.2296 for the desired OF ratio of 4.5 (verified using ProPep software). The stagnation conditions were determined from the conditions in the combustion chamber which have been designed to yield an approximate stagnation pressure and temperature of 300 psi and 3010 K, respectively. These values will be assumed to be constant through this analysis; however, this will not actually be the case throughout the burn. The engine performance section details the analysis done to account for changing combustion chamber pressure; combustion chamber temperature, propellant mass flow rate, and specific heat ratio (see section 3.7).

To determine the expected mass flow rate $\dot{m}$, a desired thrust and altitude is needed. The equation for the thrust F_t was shown in Equation 3.4 of Section 3.2 and is shown again below.

$$F_t = \dot{m}V_e + (P_e - P_a)A_e \tag{3.4}$$

V_e is the exit velocity of the propellants, P_e is the pressure at the nozzle exit, P_a is the atmospheric pressure at a given altitude, and A_e is the exit area of the nozzle. The exit velocity of the propellant V_e is dependent upon the ratio of the stagnation pressure P_0 and the back pressure P_a according to the isentropic relation shown in Equation 3.3.

$$\frac{P_0}{P_e} = \left[1 + \left(\frac{\gamma-1}{2}\right)(M_e)^2\right]^{\frac{\gamma}{\gamma-1}} \tag{3.3}$$

M_e is the Mach number at the exit of the nozzle and P_e is the pressure at the nozzle exit. This exit pressure will be designed to be slightly larger than the atmospheric pressure P_a since an underexpanded nozzle is desired. It is general practice to design the nozzle for an altitude of two-thirds of the maximum expected operating altitude. The ambient pressure P_e was then found by determining the atmospheric pressure at this altitude. Using the previously stated ideal values of stagnation pressure and specific heat ratio, M_e yields a value of M_e=2.65 at the launch altitude of 4355 ft. Since the Mach number at the exit is simply the velocity of the propellants V_e divided by the speed of sound at the exit of the nozzle, V_e can be solved for and was found to be approximately 7194 ft/s. Next, the isentropic relation for the mass flow rate $\dot{m}$ at the exit of the nozzle was determined and solved for the exit area A_e. Equation 3.17 shows the resulting equation.

$$A_e = \frac{\dot{m}}{P_o M \sqrt{\frac{\gamma}{RT_0}}\left[1+\left(\frac{\gamma-1}{2}\right)M_e{}^2\right]^{\frac{\gamma+1}{2(1-\gamma)}}} \tag{3.16}$$

Plugging Equation 3.16 into Equation 3.4, the mass flow rate can be solved for to yield Equation 3.17.

$$\dot{m} = \frac{F_t}{\left[V_e + \frac{P_e - P_b}{P_0 M \sqrt{\frac{\gamma}{RT_0}}\left(1+\frac{(\gamma-1)}{2}M_e{}^2\right)^{\frac{\gamma+1}{2(1-\gamma)}}}\right]} \tag{3.17}$$

For a desired thrust and given altitude, all values are known in Eq. 3.17 and, hence, the desired mass flow rate can be determined.

Table 3.5. Final Nozzle Design Parameters

Nozzle Parameters

Throat Diameter, D_T [in]	1.038
Exit Diameter, D_e [in]	1.95
Weight [lbs]	0.96

Once the flow rate is determined, this value can be used as $\dot{m}_{max}$ in Equation 3.15 to determine the throat area A* necessary for choking. Also, with knowledge of the exit Mach number M_e, the corresponding area ratio can be found using the isentropic relations between area ratio and Mach number. It was determined that at an altitude of 4355 feet and with a desired thrust of 315.74 lb_f, the corresponding mass flow rate was 1.57 lb_m/s. This then corresponds to a throat diameter D_t of 1.038 inches and a nozzle exit diameter D_e of 1.95 inches. These values were used as an excellent preliminary design and starting points when analyzing the performance of the entire engine (see section 3.7). Further analysis of the engine performance and varying engine characteristics led to the finalized numbers for the nozzle. These values are shown in Table 3.5. With these area values known, the next step taken in the design process was determining the contour of the nozzle both at the entrance and the exit. Figure 3.5 shows a sectioned view of the nozzle in its current state.

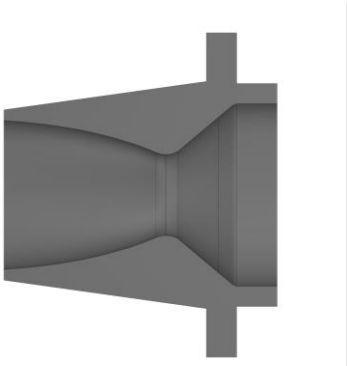

Figure 3.5. Cross-section of the nozzle.

Referencing Figure 3.5, the right side is the entrance of the nozzle and the left side is the exit. Note that the protrusion on the entrance side will act as a graphite insert at the exit of the combustion chamber. The contour of the entrance is generally insignificant to the performance of the nozzle, so the selected contour was based mainly on manufacturability. The contour of the exit, on the other hand, is very significant to the performance and efficiency of the nozzle. According to nozzle calculations provided by Dr. Tom Pollock, the

ideal nozzle exit contour is a cubic contour with a departure angle between 15 and 19 degrees. This type of contour is beneficial because it reduces the necessary length of the nozzle and, correspondingly, decreases the weight of the nozzle, as well as increases the efficiency of the nozzle. For these reasons, this type of contour, as can be seen by Figure 3.5, was utilized for the exit of the designed rocket nozzle.

3.6. Plumbing

The engine plumbing transports the nitrous oxide to the injector plate. The oxidizer tank and fittings must survive high pressures while also ensuring the system interfaces correctly. The plumbing must satisfy three design requirements: throughout the operation of the engine, the plumbing must be able to withstand 1000 psi; transport a minimum initial oxidizer flow rate of 1.25 lb_m/s to ensure the injector is supplied with the target flow rate; and the system must also minimize the amount of pressure loss.

3.6.1. Oxidizer Tank and Fittings

The upper engine, as laid out in Figure 3.6, consists of the oxidizer tank, fittings, and injector plate. The purpose of the upper engine is to control the input and output of nitrous oxide by either active control (servo) or designed orifice constriction (tubing diameter and injector coin).

Figure 3.6. Upper engine arrangement from oxidizer tank (left) to injector plate (right).

The oxidizer tank was one of the main challenges in the overall engine design. Since the density of nitrous oxide varies drastically with temperature, a worst-case filling temperature of 85°F was chosen when approximating volume requirements. Using a constant oxidizer-to-fuel ratio, the required mass of oxidizer came out to be around 11.46 lbs. for a rough burn time of 10s. Based on the density of nitrous oxide at the given temperature, this resulted in a required container volume of 461 cubic inches.

At first, the idea was to use aluminum cylinders to hold the oxidizer, but with such a large volume required for a burn that long other solutions were explored to decrease the weight. Composite cylinders seemed to be the best alternative due to their extreme pressure applications and lighter masses. A few vendors were looked at, including Luxfer and Catalina Cylinders. Each manufacturer sold a variety of different cylinders ranging from 122 to almost 5500 cubic inches. The model which suited the team's needs the most was T84A from Luxfer, even though the specs listed on their website were not accurate. The cylinder provides 550 cubic inches of space, weighs only 12.5 lbs, and

is capable of operating at pressures up to 4500 psi, which is well above what the nitrous oxide will ever experience on the launch rail. Even so, each cylinder has a minimum burst pressure of 11,250psi, making it exceptionally safe. Ideally, the excessive pressure rating would be traded in for a lighter tank, but all tanks that met this trend tended to be overly large in diameter and length.

The T84A is tapped on one end with a 7/8" UNF female fitting. From this, a 7/8" UNF-to-3/4" NPT adapter will be utilized to transition to pipe fittings. A 7/8" MNPT to compression tube fitting will connect to tubing, which will be used to place the center of gravity either higher or lower as needed. Another compression-to-MNPT fitting leads into an aluminum tee capable of withstanding approximately 3000 psi. Originally, the aluminum tee was going to be made out of stainless steel but with the cost and weight reduction that aluminum the team decided to move in that direction. Depending on what type of instruments will be used during the static engine tests, an aluminum cross may be used to allow another outlet opposite of the fuel line. Either way, the tee/cross will grant access to the "fuel" line which simply leads to an elbow which points toward the nose of the rocket. This will permit the installation of t

3.6.2. Flow Analysis

Flow Analysis was performed to evaluate and measure how well the plumbing satisfied the design requirements. The first objective toward that goal was to ensure an oxidizer flow rate of 1.25 lb_m/s. To fulfill this requirement, the density of nitrous oxide was calculated for a predicted maximum temperature of 85° F on the phase boundary between gas and liquid.

$$d = \sqrt{\frac{4\dot{m}_{ox}}{\pi\sqrt{2\rho\Delta P}}} \tag{3.18}$$

Equation 3.18 combines Bernoulli's equation and the mass conservation principle to calculate the diameter, d, required to transport liquid oxidizer through the plumbing at the desired a mass flow rate, $\dot{m}_{ox}$. When the nitrous oxide density, ρ, decreases, the diameter increases, and the liquid density decreased as the temperature rose. 90° F was the highest expected temperature, so Equation 3.183 was used with the density associated, 43.34 lb_m/ft^3.

Considering the $\dot{m}_{ox}$ constant, the required diameter was calculated as 0.38 inches when ΔP was the maximum pressure gradient (615 psi), and 0.50 inches for the final pressure difference (200 psi). The plumbing was designed to accommodate the 200 psi difference for the final condition. The assumption of a constant oxidizer flow rate for this calculation actually overestimates the required diameter as can be seen in Eq. 3.18 because the oxidizer flow rate decreases over the operation of the engine, but to be safe the plumbing was chosen to be greater than ½ inches in diameter.

The flow analysis is used to evaluate pressure loss within the plumbing. The components that affect the pressure are two male NPT nipple adapters, one ball valve, a piece of four inch stainless steel tubing, one aluminum tee joint, one 7/8 inch male UNF to ¾ inch female NPT adapter, and two compression tube fitting-to-male NPT adapters. The

pressure loss calculations are integrated into the engine simulation code, but a test case is shown below at 90° F and at a 1.57 lb_m/s oxidizer flow rate to display the calculations involved.

Table 3.6. Pressure losses through the plumbing.

Types of Plumbing	Qua.	Pressure Losses(psi)
¾" OD stainless steel tubing	4 in	0.173
Aluminum Tee	1	0.691
Ball Valve	1	0.221
7/8 UNF to ¾ NPT	1	0.170
Hex nipple	2	0.706
Compression Fitting to ¾	2	0.706
Total Pressure Loss		2.67

As seen in Table 3.6, the aluminum tee causes the largest pressure drop across the system. The total pressure loss in the system was evaluated to be 2.67 psi, which was deemed acceptable for the system considering that it was around 0.3 percent of the initial pressure gradient (615 psi).

$$\Delta P = \lambda \left(\frac{L}{D_h}\right)\left(\frac{\rho v^2}{2}\right) \tag{3.19}$$

$$\frac{1}{\lambda^{0.5}} = -2\, log_{10}\left(\frac{2.51}{Re*\lambda^{0.5}} + \frac{k}{3.72D_h}\right) \tag{3.20}$$

$$Re = \frac{\rho D_h v}{\mu} \tag{3.21}$$

$$ln(\mu) = 1.09 + \frac{50.2}{T} - 0.01134 * T + (-9.8409999 * 10^{-6}) * T^2 \tag{3.22}$$

Equations. 3.19-3.22 were used to calculate the pressure drop across the tubing. Most of the inputs for Eq. 3.19, the Darcy-Weisbach equation, are already defined or solved for except the Darcy-Weisbach friction coefficient, λ. This friction coefficient is calculated with Eq. 3.20, also known as the Colebrook equation. The Colebrook equation describes the turbulent region of the Moody Diagram, which in turn shows the relationship between the Darcy-Weisbach friction coefficient and Reynolds number. To determine the friction coefficient and if the flow is turbulent, the Reynolds number is calculated with Eq. 3.21. Given these results, all of the inputs for Equation 3.21 are defined, except for the kinematic viscosity coefficient. This is ultimately found using Eq. 3.22.

For the test case, the temperature of 90° F was converted into Kelvin then substituted into Eq. 3.22. The kinematic viscosity was calculated as 0.044 centipoises or $2.46*10^{-6}$ lb/in/s. This kinematic viscosity was then used in Eq. 3.21 with the density of the nitrous oxide, ρ, the hydraulic diameter of the tubing, D_h, and velocity of the fluid, v. Most of these values are known properties of the system besides the kinematic viscosity, and the velocity of the fluid. The kinematic viscosity was calculated using Eq. 3.22, and the velocity was solved using the conservation of mass. In the test case, the inner diameter, density, and velocity were 0.63 inches, 0.023 pound/inch^3, and 216.4 inches/second respectively. The Reynolds number was $1.291 * 10^6$, a relatively high Reynolds number, so the flow is predicted to

be turbulent. This fulfills the condition to use Equation 3.22. The friction factor is found through iteration by isolating and solving for the friction variable on the left hand side of Eq. 3.20, and substituting an initial value for the friction coefficient. The iterations continued until the friction factor converged onto a value of $1.92*10^{-2}$ for the test case with a hydraulic diameter,D_h , of 0.63 inches. This friction factor is then substituted into Eq. 3.19. For the test case the density, hydraulic diameter, and velocity are the same as substituted into Eqs. 3.20, and 3.21, and the length, *L*, is 4 inches. The pressure drop due to the tubing is 0.173 psi.

The pressure drops in the ball valve is calculated using Eq. 3.23.

$$\Delta P = S(\frac{q}{C_v})^2 \qquad (3.23)$$

This equation uses the specific gravity, *S*, of the liquid, the volumetric flow rate, *q*, and the flow coefficient, C_v, to calculate the pressure drop through the ball valve. The pressure drop across the ball valve is 0.221 psi. The flow coefficient is 30 gal/min*psi. The volumetric flow rate is 17.5 gal/min, and the specific gravity is 0.657.

The pressure drop in the aluminum tee was calculated using Eqs. 3.24 and 3.25. Equation 3.24 is a method to estimate the *K* value for equation Eq. 3.24.[18] The head loss,h_L, was then converted into pressure loss by multiplying it by gravity and density.

$$K = \frac{K_1}{Re} + K_\infty(1 + \frac{K_d}{D_n^{0.3}}) \qquad (3.24)$$

$$h_L = \frac{Kv^2}{2g} \qquad (3.25)$$

In Equation 3.24, the K_d, K_∞, and K_1 were 4 $in^{0.3}$, 200, and 0.091 . These values along with the already calculated Reynolds number were used to find the *K* value of 0.490. This *K* value was then used to calculate a head loss of 29.7 inches. This head loss was converted into pressure loss of 0.691 psi.

The 7/8 inches to ¾ inch adapter's *K* value was calculated through equation 3.26.

$$K = (1 + 0.8\lambda) * \left[1 - (\frac{D_1}{D_2})^2\right]^2 \qquad (3.26)$$

The friction factor used is the same as for the tubing, and the first diameter is 0.51 inches. The second diameter is 0.63 inches. These values are plugged into Equation 3.24. The *K* value found was 0.121. The head loss is 7.31 inches, and the pressure loss was 0.170 psi.

The other fittings used a *K* value of 0.25, and the head losses were 15.16 inches each.[17] The corresponding pressure losses were 0.353 psi each.

3.6.3. Quick Disconnect

The quick disconnect system allows the oxidizer line to attach to the fill tank outside the rocket. Safety is a major concern when filling up the tank, so it is recommended that the hose be detached remotely. In order to do this, a quick disconnect coupling plug is used as a permanent part of the plumbing assembly. The plug travels up the plumbing stem from the aluminum tee where there is a hole in the bulkhead for access to the quick disconnect body. The body is then remotely unplugged using a pneumatic air cylinder mounted to the locking sleeve of the body. Figure 3.7 shows the plug and body from Swagelok.

Figure 3.7. Quick disconnect system. (Right) plug (Left) body.

3.7. System Modelling

This section details the analysis that was performed on the propulsion system of the rocket. To begin, an overview of the engine will be presented, followed by an in-depth analysis of the engine during operation. This analysis was then implemented using MATLAB software to ultimately predict the performance of the engine throughout the burn. The overarching goal of the analysis was to create a reliable thrust vs. time curve for the engine and compare this to the total Impulse required for mission success.

3.7.1. Analysis of Engine Performance

The current engine configuration consists of an oxidizer tank, injector plate, combustion chamber, a converging-diverging nozzle, a pyrotechnic igniter, and necessary plumbing to connect separate portions of the engine. In order to simulate the performance of the engine, it was first determined how the conditions in the oxidizer tank altered throughout engine operation. Since the tank is pressurized solely from the vaporized nitrous oxide present in the tank, altering the thermodynamic state of the oxidizer will affect the pressure in the tank. This, in turn, directly affects the overall performance of the entire propulsion system. Therefore, it is critical to accurately predict how the pressure in the oxidizer tank will change throughout operation. Figure 3.8 shows how the different parameters of the propulsion system are interconnected throughout engine operation.

To begin the analysis, we must first know the initial pressure in the tank. This can be determined by specifying an initial temperature for the oxidizer tank and finding the vapor pressure of nitrous oxide at this temperature. To initiate operation of the engine, a valve will be opened that will allow the nitrous to flow from the nitrous tank to the combustion chamber. While the tank empties, liquid nitrous oxide will begin to vaporize to sustain the high pressure in the tank. This vaporization of the nitrous oxide results in heat lost from the liquid nitrous remaining in the tank. This heat loss ΔQ can be modeled as shown in Equation 3.27.

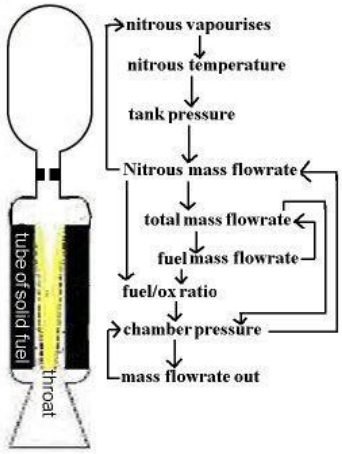

Figure 3.8. Interdependency of parameters in hybrid rocket engines. (courtesy: Aspire Space)

$$\Delta Q = m_v H_v \qquad (3.27)$$

where m_v is the amount of liquid mass vaporized and H_v is the heat of vaporization at the current nitrous temperature. We can then determine the drop in temperature ΔT of the liquid nitrous in the tank due to this heat loss. This drop in temperature can easily be calculated by Equation 3.28.

$$\Delta T = -\frac{\Delta Q}{m_l C_l} \qquad (3.28)$$

where m_l is the mass of liquid nitrous in the tank and C_l is its specific heat capacity at the current temperature. The pressure in the tank can then be determined by finding the vapor pressure of the nitrous oxide at this new temperature. The next step is to then model the flow rate of the oxidizer to the combustion chamber given this new tank pressure. According to Aspire Space, the mass flow rate of the liquid oxidizer $\dot{m}_l$ can be determined from Equation 3.29 below.

$$\dot{m}_l = N A_{inj} \sqrt{\frac{2\rho_l \Delta P}{K}} \qquad (3.29)$$

where ρ_l is the density of the liquid nitrous, ΔP is the total pressure drop from the oxidizer tank to the combustion chamber, A_{inj} is the area of the injector holes, N is the number of injector holes, and K is a loss coefficient. The value of ΔP will change throughout the operation of the engine, and these effects will be analyzed later in this section. For the initial simulation, however, this pressure drop can be calculated by finding the difference between the tank pressure and the local atmospheric pressure. Also, the presented loss coefficient attempts to account for other pressure losses in the system and can be more accurately determined through engine testing. According to Aspire Space, a value of 2 for this loss coefficient is a good starting, and this has been implemented in the actual analysis.

With the mass flow rate known of the liquid oxidizer known, the amount of liquid nitrous that has left the tank in time Δt can be found by integrating over this time interval. However, in order to determine the correct mass of liquid nitrous left in the tank, we must also account for the loss of liquid nitrous in the tank due to vaporization. This

can be done by first recognizing that the contents in the tank are constricted to the volume of the tank V_{tank} itself, represented mathematically by Equation 3.30.

$$V_{tank} = V_{liquid} + V_{vapour} \tag{3.30}$$

Rewriting this equation on a mass and density basis and solving for the liquid mass, this can be written as Equation 3.31.

$$m_l = \frac{\left(V_{tank} - \frac{m_{tank}}{\rho_v}\right)}{\left(\frac{1}{\rho_l} - \frac{1}{\rho_v}\right)} \tag{3.31}$$

where m_{tot} is the total mass in the tank, ρ_v is the density of vaporized nitrous, and ρ_l is the density of the liquid nitrous. It should be noted that all these values are calculated at the current temperature in the tank. Next, the amount of vaporized nitrous oxide m_v can then be determined by subtracting this value from the previously calculated value of liquid nitrous. With this new value of m_v, we can now return to Equation 3.27 to perform another iteration by calculating a new, lower tank temperature and running through the calculations once more. Before doing this, however, we must determine the new value for ΔP. To accomplish this, we must first calculate the total mass flow rate through the system; that is, both the mass flow rate of the nitrous oxide and the solid fuel (HTPB).

In order to determine the total mass flow rate, it is readily apparent that we must determine the fuel mass flow rate of the HTPB $\dot{m}_f$. In order to calculate this value, it is necessary to simulate the fuel regression throughout the burn. To begin, the initial regression rate was first found from experimental data[3]. With this regression rate, the initial port area and surface area can be determined as described in Section 3.2. A step in time can then be moved forward and the new port dimensions calculated using equations 3.8-3.10. With the new port dimensions, the oxidizer flux can be calculated. Using the oxidizer flux, the new regression rate is found using Equation 3.9. The mass flow rate of the fuel is then calculated using Equation 3.10 for each time step.

With both the oxidizer and fuel mass flow rates known, we can calculate the two important quantities of total mass flow rate $\dot{m}_{tot}$ and the oxidizer-to-fuel (OF) ratio. This OF ratio is found using Equation 3.32.

$$OF = \frac{\dot{m}_l}{\dot{m}_f} \tag{3.32}$$

This ratio has a significant impact on the performance of the engine as it can alter the molecular weight (M.W.) and the specific heat ratio λ of the propellant mixture, as well as the temperature in the combustion chamber T_{comb}. As a result, the characteristic velocity c* of the propulsion system, which is dependent upon the molecular weight, λ, and T_{comb}, can significantly change with different OF ratios. The dependence of c* on these factors can be seen in Equation 3.33.

$$c^* = \frac{\sqrt{\gamma R T_{comb}}}{\gamma\sqrt{\left(\frac{2}{(\gamma+1)}\right)^{(\gamma+1)/(\gamma-1)}}} \tag{3.33}$$

where R is the specific gas constant for the propellant mixture and can be evaluated by dividing the universal gas constant R* by the molecular weight. The values for the molecular weight, λ, and T_{comb} for different OF ratios were determined and verified by using ProPep software.

As stated previously, the pressure drop between the oxidizer tank and the combustion chamber will vary throughout the operation of the engine. Since we know the pressure in the oxidizer tank for each iteration from the analysis above, in order to determine the pressure drop we must now find the pressure in the combustion chamber P_{comb} in order to determine the pressure drop ΔP. Assuming choked flow at the nozzle throat, this pressure can be determined using Equation 3.34.

$$P_{comb} = \frac{\dot{m}_{tot} c^*}{A^*} \tag{3.34}$$

where A* is the desired nozzle throat area. Finally, we can return to the beginning of the analysis and perform an iteration for the next time interval Δt. Using this iterative solving process, we can accurately determine the conditions in the propulsion system until burnout, i.e. until the oxidizer tank has completely emptied of liquid nitrous.

With the conditions in the combustion chamber now known for all times during the operation of the engine, an analysis can be performed on the flow through the nozzle to determine the resulting thrust produced by the rocket at a given altitude. This analysis is very similar to that done in the nozzle section (section 3.4). This nozzle analysis was implemented into the simulation code to produce the final engine performance characteristics. The following section presents the results from the implementation of this analysis.

3.7.2. Engine Simulation Results

As stated previously, the analysis of the engine performance was implemented into MATLAB software which allowed an iterative solving method and simulation of the engine throughout the length of the burn. This simulation code took the inputs of the initial altitude, nozzle parameters, initial oxidizer tank properties, initial fuel grain geometry, and the total area of the injector holes. These values were then used to simulate the engine in its specified design state. Table 3.7 presents the values of the inputs used in the simulation code.

Table 3.7. Inputs used for engine simulation.

Inputs	Values
Nozzle Throat Diameter [in]	1.038
Nozzle Exit Diameter [in]	1.950
Initial Altitude [ft]	4355
Initial Oxidizer Tank Temperature [F]	85
Initial Fuel Grain Geometry	See Section 3.2
Volume of Oxidizer Tank [L]	9
Initial Ullage in Oxidizer Tank [%]	5
Injector Hole Diameter [in]	0.0725
Number of Injector Holes	4

Using the analysis presented in the previous section and the inputs from Table 3.7, the simulation was carried out and the corresponding results were plotted. The resulting Thrust vs. Time curve can be seen in Figure 3.9.

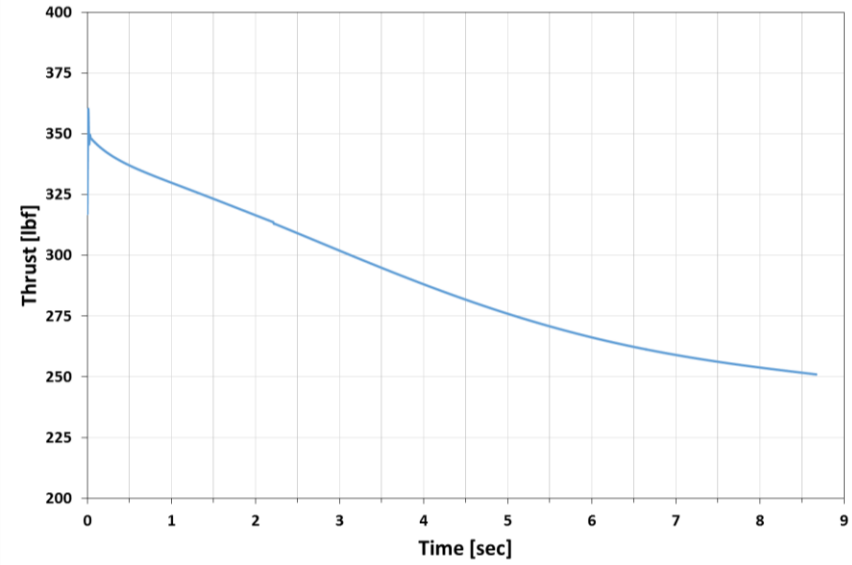

Figure 3.9. Theoretical Thrust vs. Time curve

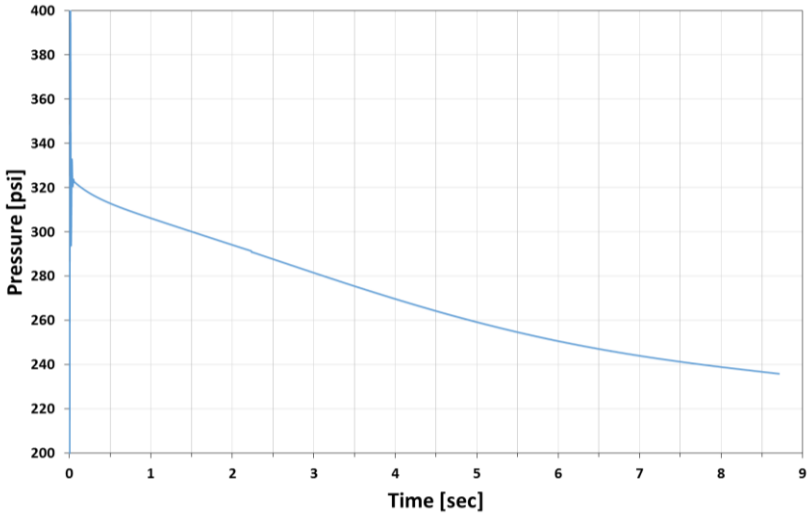

Figure 3.10. Theoretical Combustion Chamber Pressure vs. Time curve.

As can be seen from the plot, the thrust peaks at liftoff with a maximum value of approximately 350 lbf and slowly decays to approximately 250 lbf at burnout. This decay in thrust was expected and is due largely to the decreasing combustion chamber pressure and alternating OF ratios throughout the burn. The corresponding burn time is approximately 8.66 seconds. Next, the change in combustion chamber pressure throughout the burn was plotted and is shown in Figure 3.10.

By comparing this plot to Figure 3.9, it is readily apparent the thrust is strongly related to the combustion chamber pressure. This result agrees well with theory, which predicts a direct correlation between the combustion chamber pressure and the exit Mach number according to equation 3.13. It should be noted that since the altitude of the rocket will be changing during operation, the ambient pressure will also change throughout the operation of the engine. This was accounted for in the simulation.

3.8. Fabrication Analysis

For the fuel grain, a metal piece will be machined to match the shape of the port. A hole will be place in the center of the metal piece to help keep it centered. A piece of wood will be machined so that the silica sheet will slip down into it 0.5 inches for the post-combustion chamber, which is discussed in Section 3.3. A hole the same size as the center of the metal piece will be cut out in the center of wood piece and a rod will be inserted in the hole to keep it in place. Both the wood and the metal piece will be covered in wax paper to keep them from sticking to the HTPB. The HTPB will be cast into this mold using R45a and Papi 94, a room temperature curing agent. The mixture will be 88% R45a and 12% Papi 94, by weight. The kit that makes 9 pounds of HTPB costs $90.

The injector consists of two main parts: an injector plate and an injector plate holder as shown in Figure 3.3. (a). The plate will slide into the holder and seal utilizing a male O-ring on the top of the 3" diameter plate. In addition to this, the plate will feature a set of three radially symmetric angled holes, and a single center hole. The four holes will impinge the oxidizer at a point 1/8" inside the pre-combustion chamber Figure 3.3. (b). The purpose of the center hole is so that the mass flow rate of the injector can easily be increased by drilling this single hole out larger without disrupting the symmetry of the pattern. All four injection orifices also have a .09" deep counter bore on the bottom face of the plate to insure a smooth and linear flow. Without this counter bore the Nitrous oxide would tend to follow the surface of the plate which would result in flow dispersion.

The plate holder features a reservoir on top of where the plate will slide into, a flange for interfacing with the lower engine assembly, a cavity to house a portion of an insulating silica sheet, and a 3/4" threaded female appendage to connect to the oxidizer fuel line Figure 3.3. (a). The reservoir is there to ensure an even pressure across each injector orifice. The flange will contain a radial pattern of eight 1/4" holes so that the injector can bolt into the combustion chamber beneath it. When the injector is fully assembled as seen in Figure 3.4, the injector plate will be held in place between the combustion chamber flange and the injector holder body. Consequently the system will only seal when the bolts are tightened. To prevent galling between the injector holder and the combustion chamber flanges, there will be a PTFE gasket sandwiched between them This gasket will also double as a way to ensure that the upper engine will be sealed off from the rest of the rocket.

The injector will consist of Aluminum 6061, which was chosen for its unreactive nature, strength, and machinability. Ideally the entire injector would be made out of 360 Brass because of brass's lower thermal expansion coefficient, higher strength, and machinability. The only fault with 360 Brass is that it is over five times more expensive than 6061 aluminum and that it is over three times as dense. The team has determined that it is possible and

much more cost effective to make the entire injector out of aluminum by using an insulating silica sheet to protect the plate from fusing to the holder in the presence of extreme heat radiation.

Table 3.8. Material properties of brass and aluminum.

Material	360 Brass	6061-T6 Aluminum
Density	0.307 lb/in^3	0.0975 lb/in^3
Melting	1630 °F	1080 °F
Cost	\$3.45 per in^3	\$ 0.59 per in^3
Yield strength	45 KSI	40 KSI
Young's Modulus	14,000 KSI	10,000 KSI
Machinability rating	100%	50%
Thermal Expansion Coef.	11.4 ppm/ °F	13 ppm/ °F

The nozzle has to survive the most extreme temperatures in the entire rocket, outside of the fuel which is supposed to burn. Since temperatures reach extremely high values in the nozzle (on the order of 3000 K), the material of the nozzle is a very important parameter. Graphite has been selected as the most appropriate choice for the nozzle material as it has the highest melting point of any structural solid. This is important because operating at temperatures above the melting point of the nozzle material will cause erosion of the throat, and this will result in a loss of choked flow and a correspondingly large loss of thrust. In addition, graphite is relatively lightweight when compared to many other structural solids, which aids in reducing overall engine weight. A disadvantage of using graphite, however, is its brittle nature. Since the nozzle will be subjected to extreme conditions and high loads, analysis and testing must be performed to ensure an appropriate level of confidence in the design of the nozzle.

3.9. Testing

Testing of the engine will be the most time-consuming aspect of the spring semester. There are several different tests that will be conducted to ensure safety and reliability of equipment. Some of the smaller tests that will need to be done before the static tests include pressure testing the combustion chamber and oxidizer fill line, possibly stress-bending the injector plate, and simulating the fuel motion for the silica.

The combustion chamber will undergo a great deal of pressure when burning, so ideally a hydro test would verify the target pressures are well within the structural strength of the aluminum tube. Additionally, the welds need to be checked for any type of leaking during this test since a small puncture in the seam of the flange could potentially be catastrophic. At the same time the steel braided hose will be pressure tested to confirm that the hose-to-NPT fittings are sealed correctly.

The injector plate is another item which is being changed up from conventional methods, so some time will be spent trying to validate the effectiveness of the new design. Although the experiment will not be able to replicate the extreme temperatures of the combustion chamber, it will at least provide a good idea of whether or not the coin will break by sitting on the upper flange of the combustion chamber as seen in Figure 3.11.

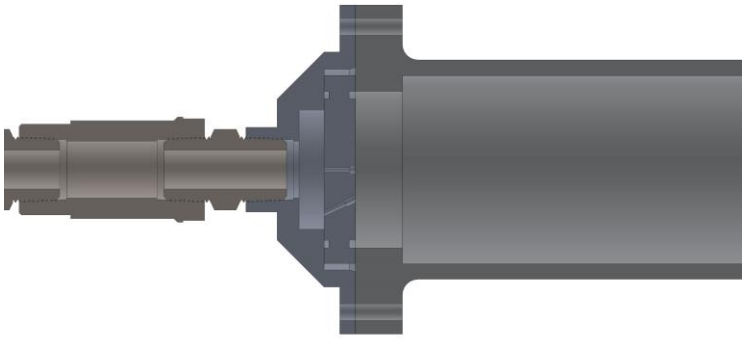

Figure 3.11. Aluminum injector coin sandwiched between the plate and combustion chamber.

Another major concern for the team is the use of silica insulation as a substitute for phenolic. Silica sheets are better in regards to temperature, thermal expansion, cost, thermal conductivity, and density, but it is the advantage in density that costs it in the area of rigidity. Phenolic makes a very versatile fuel mold casing in which to cast the grain, but silica lacks the firmness of its composite counterpart. One way around this is to cast the silica around a tube of the proper outer diameter and then coat the shell in epoxy to stiffen it up. The seam of the sheet has to be sealed in some way and epoxy was already the best answer for this. Even so, it becomes advantageous to try to simulate combustion and attempt to force the fuel grain out of place. The worst case scenario that could happen is that the epoxy disintegrates as fuel and the silica sheet loses rigidity. In this case the fuel grain should still be held into place by the graphite inserts and nozzle, but precautions will be taken to insure that this is indeed the case.

The goal is to have the first engine test by February 22nd and do roughly eight engine tests over the following few weeks. The engine should be fully characterized at different initial conditions and compared to theoretical values for consistency. If an accurate pattern can be assessed than the likelihood of achieving a thrust capable of reaching a target altitude is maximized.

3.10. References

[1]Rajesh K.K. "Thrust Modulation in a Nitrous-Oxide/Hydroxyl-Terminated Polybutadiene Hybrid Rocket Motor", 42nd AIAA/ASME/SAE/ASEE Joint Propulsion Conference & Exhibit.

[2]Martin J. Chiaverini, Nadir Serin, David K. Johnson, Yeu-Cherng Lu, Kenneth K. Kuo, and Grant A. Risha. "Regression Rate Behavior of Hybrid Rocket Solid Fuels", Journal of Propulsion and Power, Vol. 16, No. 1(2000),pp. 125-132.

[3]Robert A. Braeunig, 2012, Rocket Propulsion, Basics of Space Flight, www.braeunig.us/space/propuls.htm (November 5, 2013)

[4]Boedeker Plastics, Inc., 2013, Typical Properties of Glass Laminates, Industrial Laminate Specifications Glass-Based Phenolics, http://www.boedeker.com/ilamg_p.htm (November 5,2013)

[5]Pollock, T, "Injector Lecture Notes," Texas A&M Senior Rocket Design Class

[6]Prometheus Team. "Final Report," Texas A&M Senior Rocket Design Class

[7]Volare Team. "Final Report," Texas A&M Senior Rocket Design Class

[8]Speedy Metals, "Speedy Metals Material Information." www.speedymetals.com/information/materialframe.htm

[9]McMaster-Carr, "Raw Materials" www.mcmaster.com/#metals/=q4mwi8

[10]Engineering Toolbox, "Orifice, Nozzle and Venturi Flow Rate Meters" www.engineeringtoolbox.com/orifice-nozzle-venturi-d_590.html

[11]Pollock, Tom. Analysis of a Rocket Nozzle. N.p.: n.p., 2013. Web. 29 Sept. 2013

[12]John, James, and Theo G. Keith. Gas Dynamics. Upper Saddle River, NJ: Pearson Prentice Hall, 2006. Print.

[13]Humble, Ronald, Gary N. Henry, and Wiley J. Larson. Space Propulsion Analysis and Design. New York: McGraw-Hill, 1995. Print.

[14]Newlands, Rick M. "Modelling the Nitrous Run Tank Emptying." Aspire Space. N.p., n.d. Web. 08 Jan. 2014. <http://www.ricknewlands.webspace.virginmedia.com/pages/technical-papers/techpapers.htm>.

[15]"Major Loss in Ducts, Tubes and Pipes." Major Loss in Ducts, Tubes and Pipes. Engineering Toolbox, n.d. Web. 13 Jan. 2014. <http://www.engineeringtoolbox.com/major-loss-ducts-tubes-d_459.html>.

[16]"Pipe Flow Calculators." Calculators for Pressure Drop, Pipe Diameter, Flow Rate, Venturi Tube, Orifice Plate and Much More. N.p., n.d. Web. 13 Jan. 2014. <http://www.pipeflowcalculations.com/pipe-value-fitting-flow/flow-in-values-fitting.php>.

[17]"Hydraulic Design for PE Pipes." Vinidex. Vinidex, n.d. Web. 13 Jan. 2014. <http://www.vinidex.com.au/technical/pe-pressure-pipe/hydraulic-design-for-pe-pipes/>.

[18]"Summary." Pressure Loss from Fittings in Pipe – Neutrium. Neutrium, n.d. Web. 18 Jan. 2014. <http://neutrium.net/fluid_flow/pressure-loss-from-fittings-in-pipe/>.

4. Aerodynamics

4.1. Objective

The aerodynamic objectives were to design a rocket that was stable and with low drag. In the following sections, a method for finding the center of pressure, designs for aerodynamically optimal nose and fins, and simulations for other aerodynamic properties are presented.

4.2. Theoretical Aerodynamics

According to approximate velocity values found in the Computational Methods section, the rocket will have a maximum flight speed exceeding Mach 0.5. For flows with a Mach number higher than 0.3, the flow cannot be considered as incompressible. A subsonic compressible approach is necessary.

Two subsonic compressible flow analysis options that were utilized in the aerodynamic considerations of this project were experimental databases and Computational Fluid Dynamics (CFD). Due to the relatively simple configuration of the rocket, it was believed that related databases, such as NACA, would provide useful aerodynamic stability information. Unfortunately, there were no databases that dealt with a spectrum of rocket designs, only for specific rockets that did not resemble the SRT-1 Valor. The other option, CFD, can use numerical simulations to predict aerodynamic forces. Further CFD analysis is discussed in Section 4.7.

As alternative model, the Prandtl-Glauert transformation was considered. Although it is an accurate model for compressible flows at subsonic velocities, it is only valid for 2D flows, which have no physical meaning for the rocket. There is a format of the Prandtl-Glauert transformation for 3D flows, but due to the complications intrinsic to the model, it was not considered a viable solution.

A final solution was found with the Theoretical Aerodynamic Derivatives (TAD) depicted in "An improved Theoretical Aerodynamic Derivatives Computer Program for Sounding Rockets"[1]. For this method, the following assumptions are made in the publication:

1. The angle attack is very small;
2. The flow is inviscid and steady;
3. The vehicle is a rigid body;
4. The nose tip is a sharp point;
5. The flight number is a subsonic or supersonic. The TAD does not embody transonic or hypersonic aerodynamics.
6. The wings are unbanked and do not have sweptback trailing edges or swept forward leading edges.

Analyzing each assumption for the specifications of the rocket, the research showed that:

1. The rocket will be launched with the smallest angle of attack possible given weather conditions on the day of launch. For the purposes of aerodynamics, the angle of attack was considered negligible, because the rocket should be stable enough to have small angles of attack .According to *Topics in Advanced Model*

Rocketry the viscous effects can be neglected on the nose cone and body Due to the unknowns represented by weather conditions, it is impossible to affirm if the flow is steady, but by considering a small uncertainty due to the viscosity, it becomes feasible to make such an assumption;

2. It has been assumed that the rocket does not suffer noticeable bending momentums during the flight;
3. Since the rocket will not be using a blunted nose cone, assumption 4 of TAD is applicable;
4. Due to the complications associated with sonic and trans-sonic regions, the rocket has been designed to not exceed 0.8 Mach, and thus assumption 5 of TAD will hold.
5. It fails to correspond to Valor's design, but since sweepback angles are small, it is tolerable

After verification of TAD's assumptions, it has been shown that TAD is a useful, accurate method for aerodynamic analysis.

One of the advantages of the TAD model is that it deals with the interferences of all the elements on the rocket. For example, the wing-tail interference is treated by assuming one completely rolled-up vortex per wing panel and evaluating the tail load by strip theory.

For TAD to be applicable the rocket needs to be separated into different elements; body elements, and fin elements.

4.3. Body Aerodynamics

For the rocket, it is only necessary to work with two body elements: the nose cone and the body tube. For both elements, the equations for determining their properties at subsonic conditions are the same:

$$(C_{N\alpha})_B = 2\frac{A_B}{\beta A_r} \tag{4.1}$$

$$\bar{X}_B = l_o - \frac{V_B}{A_B} \tag{4.2}$$

$$(C_{m\alpha})_B = \frac{2}{\beta A_r L_r}[l_o A(l_o) - V_B] \tag{4.3}$$

Where, $(C_{N\alpha})_B$ is the Normal Force Coefficient for the body component, A_B is Base Area, β is $\sqrt{1-M_2}$ for subsonic flows, A_r is the reference area, $\bar{X}_B$is the x coordinate of the center of pressure of the body component, l_o is the total body length, V_B is the body volume, $(C_{m\alpha})_B$ is the pitch forcing moment coefficient derivative of the body component, $L_r$is the reference length, and $A(l_o)$ is the area at l_o.

For the body tube, due to its geometry, it can be seen through the equations above that its effects are negligible.

4.4. Fin Aerodynamics

The total normal force coefficient due to the tail, including dihedral effects, is given by:

$$(C_{N\alpha})_T = \frac{N}{2}(C_{N\alpha})_l \tag{4.4}$$

$$(C_{N\alpha})_l = \frac{2\pi AR}{2+\sqrt{4+(1-M^2 cos^2 \Gamma_C)\frac{(AR)^2}{(cos\Gamma_C)^2}}} \tag{4.5}$$

$$\begin{cases} \bar{X}_T = l_T - \frac{x_T}{3}\left(\frac{c_r+2c_t}{c_r+c_t}\right) + \frac{1}{6}\left(c_r + c_t - \frac{c_r c_t}{c_r+c_t}\right) \\ \bar{Y}_T = r_t + \frac{1}{3}\left(\frac{c_r+2c_t}{c_r+c_t}\right) \end{cases} \tag{4.6}$$

Where, $(C_{N\alpha})_T$is the total tail normal force coefficient, $(C_{N\alpha})_l$is the single fin normal force coefficient, AR is the aspect ratio of exposed fin, Γ_C is the mid-chord line sweep angle, c_r is the fin root chord, c_t fin tip chord, $x_t = s * tan\,\Gamma_L$, s is the maximum semi-span of wing or tail in combination with body, and Γ_T is the trailing edge sweep angle.

4.5. Nose Cone

4.5.1. Subsonic Nose Cone

The nose cone shape will not significantly affect the Center of Gravity/Center of Pressure relationship relative rocket's design (i.e. overall length, fin size and location, weight distribution of components, etc.). Due to this, nose cone can be treated as a separated component.

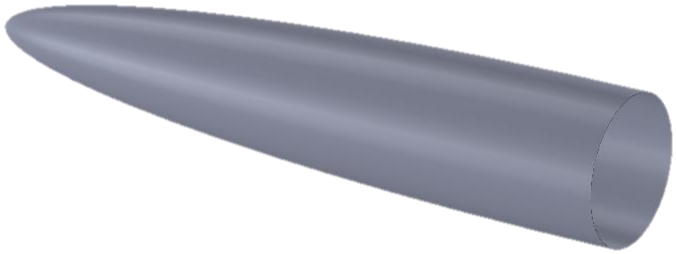

Figure 4.1. Elliptical nosecone design concept.

At speeds below critical Mach, one of the primary forms of drag is skin friction. To minimize this drag, the aircraft should be designed to minimize the exposed skin area, or "wetted surface", which generally implies the fuselage should be somewhat "egg shaped", with a fineness ratio about 4.5. According to some references, a ratio of 2 would be ideal, but significantly greater ratios are of greatest interest. This is often due to the competing need to place the tail control surfaces at the end of a longer moment arm to increase their effectiveness. Reducing the length of the fuselage would require larger controls, which would offset the drag savings from using the ideal fineness ratio.[2]

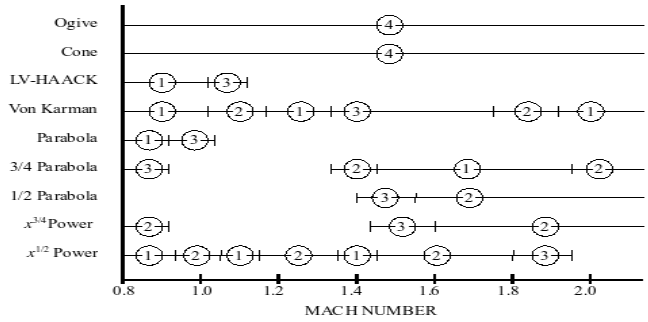

Figure 4.2 Performance for different nose cones and Mach numbers

$$Finnese\ ratio = \frac{L}{D} \tag{4.7}$$

4.5.2. Nose Cone for Transonic Flight

The Figure 4.2 shows the performance for different nose cones and the numbering is a follows: 1 is superior, 2 is good, 3 is fair and 4 is inferior.

It can be concluded that in the range of the transonic flow, the Von Kármán, LV-Haack, parabola and ¾ parabola designs are the most efficient.

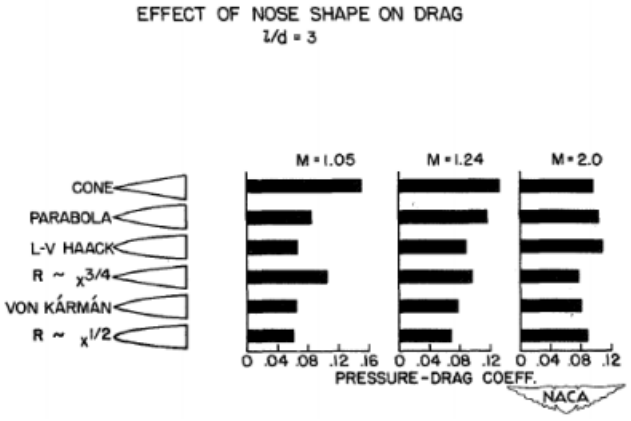

Nose shapes	$\frac{C_{D_f}}{C_f}\frac{l}{4l/d}$	$\frac{\text{Volume}}{\pi d^2 l/4}$
Cone	0.500	0.333
$x^{3/4}$	.571	.400
$x^{1/2}$	.667	.500
Parabolic	.667	.534
$\frac{3}{4}$P	.600	.445
$\frac{1}{2}$P	.556	.393
L-V Haack	.700	.562
Von Kármán	.653	.500

Figure 4.3 Drag Coefficients for different nose cone designs.

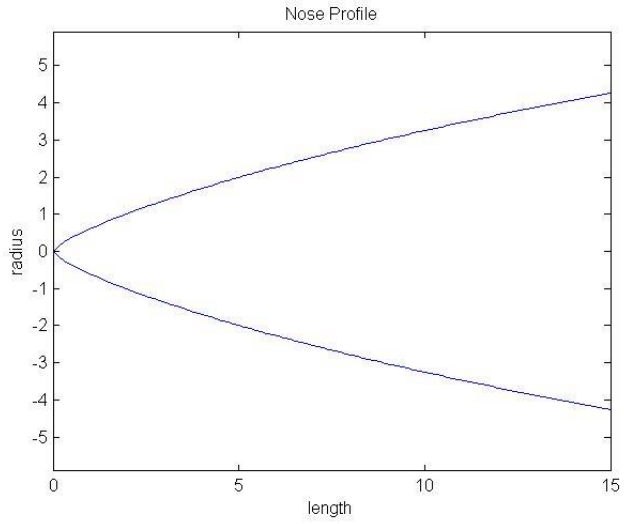

Figure 4.4. 2D plot of Von Kármán nose cone design

The results of references 3 and 4 depicted in Figure 4.2 indicate that the Von Kármán and the $x^{1/2}$ noses have the lowest drag over the Mach number range (M=0.8 to 2). While the $x^{1/2}$ nose had a low initial drag rise, its drag continues to rise slowly over most of the Mach number range shown. The drag of the Von Kármán nose, however, peaks at about M=1.4. The Von Kármán nose has the further advantage of tapering smoothly into the body behind it which is a factor in obtaining low subsonic drag and high rise in drag relative to Mach numbers. It is also assumed that the smooth tapering would reduce the interference drag of the nose on an after-body.

Due to all of these considerations, the Van Kármán design was found to be optimal for rockets flying at speeds in the transonic region. The system of equations that constitute the design is depicted in Equation 4.8, where x is the distance from the tip of the nose cone, y is the distance from axisymmetric axis of the rocket, L is the length of the nose cone, and R is the radius at the base of the nose. Figure 4.4 depicts a 2D plot of the nose.

$$\begin{cases} \theta = arccos\left(1 - \frac{2x}{L}\right) \\ y = \frac{R}{\sqrt{\pi}}\sqrt{\theta - \frac{sin(2\theta)}{2}} \end{cases} \quad (4.8)$$

The results presented in Figure 4.4 is for a fineness ratio of 3, but it is assumed that for low fineness ratios (approximately 5 or 6), where the pressure drag will be fairly high, the comparisons will be essentially correct. Above fineness ratios of 5 or 6, the pressure drag becomes less important and so does the nose shape.

At supersonic speeds, the fineness ratio has a significant effect on nose cone wave drag, particularly at low ratios; but there is very little additional gain for ratios increasing beyond 5:1. As the fineness ratio increases, the wetted area, and thus the skin friction component of drag, is also going to increase. At the minimum drag fineness ratio, there is ultimately going to be a tradeoff between decreasing wave drag and increasing friction drag.

From the Ref 3, and all the theory presented before, it has been concluded that the optimal fineness ratio for transonic flight is near to 5.

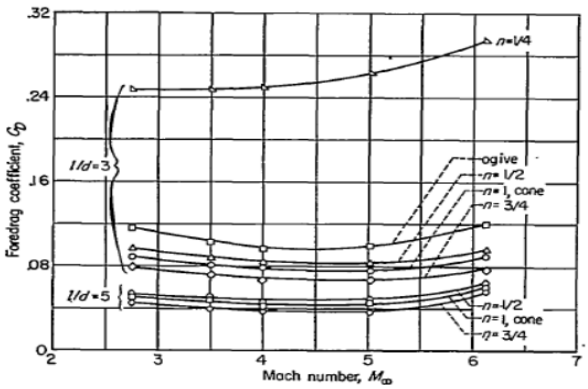

Figure 4.5. Drag coefficient for different fineness and designs

4.5.3. Choice of Nose cone

Since it was found that the rocket will operate in the transonic region, the elliptical nose cone was selected with the following dimensions: L=27.27in and Fr=4.5.

4.6. Total Vehicle Aerodynamics and Center of Pressure

TAD can also be used for calculating the values for a rocket with wings, but since the desired rocket does not have such wings, all the components related to them are omitted.

Calculation of the Normal Coefficient:

$$C_{N\alpha} = (C_{N\alpha})_B + \sum(C_{N\alpha})_B + \sum(C_{N\alpha})_{T(B)} + \sum(C_{N\alpha})_{B(T)} \quad (4.9)$$

Where,

$(C_{N\alpha})_B$ = Normal Force Coefficient for the Body component;

$\bar{X}_B$ = x coordinate of the center of pressure of the body;

$(C_{N\alpha})_{T(B)}$ = Normal Force Coefficient for the Tail in presence of the body;

$\bar{X}_{T(B)}$ = x coordinate of the center of pressure of the tail in presence of the body;

$(C_{N\alpha})_{B(T)}$ = Normal Force Coefficient of the body in presence of the tail

$\bar{X}_{B(T)}$ = x coordinate of the center of pressure of the body in presence of the tail;

$$(C_{N\alpha})_{T(B)} = (C_{N\alpha})_T K_{T(B)} \tag{4.10}$$

$$(C_{N\alpha})_{T(B)} = (C_{N\alpha})_T K_{T(B)} \tag{4.11}$$

For the subsonic case:

$$K_{T(B)} = \frac{2}{\pi\left(1-\frac{1}{r}\right)^2}\left\{\left(1+\frac{1}{r^4}\right)\left[\frac{1}{2}tan^{-1}\left(r-\frac{1}{r}\right)+\frac{\pi}{4}\right]-\frac{1}{r^2}\left[\left(r-\frac{1}{r}\right)+2tan^{-1}\left(\frac{1}{r}\right)\right]\right\} \tag{4.12}$$

$$K_{B(T)} = \frac{\left(1-\frac{1}{r^2}\right)^2}{\left(1-\frac{1}{r}\right)^2} - K_{T(B)} \tag{4.13}$$

Calculation of the center of pressure:

$$\begin{cases} \bar{X} = \frac{\bar{X}_B(C_{N\alpha})_B+\sum \bar{X}_{T(B)}(C_{N\alpha})_{T(B)}+\sum \bar{X}_{B(T)}(C_{N\alpha})_{B(T)}}{C_{N\alpha}} \\ \bar{Y} = 0; \end{cases} \tag{4.14}$$

Where,

$$\bar{X}_{T(B)} = \bar{X}_{T(B)} \tag{4.15}$$

$$\bar{X}_{B(T)} = l_T + \frac{c_r}{4}\left[\frac{\sqrt{s^2-{r_t}^2}cosh^{-1}\left(\frac{s}{r_t}\right)-s+\frac{\pi}{2}r_t}{\sqrt{s^2-{r_t}^2}cosh^{-1}\left(\frac{s}{r_t}\right)+\frac{s}{r_t}-\frac{\pi}{2}} - r_t\right]tan\left(\Gamma_{1/4}\right) \tag{4.16}$$

l_T = Location of Fin Leading Edge Intersection with Body;

r_t = Body radius at Tail;

$\Gamma_{1/4}$ = Quarter Chord Sweep Angle;

For the moment this model is only being used to find the Center of Pressure, however it can also be used for calculating lift.

4.7. Computational Fluid Dynamics

For the computational fluid dynamics (CFD), the SolidWorks Flow Simulation[7] was used to generate approximate values for the forces that are expected to be seen during flight. The program itself used the rough model created with SolidWorks. For the rocket, global goals were initially used to find values for dynamic pressure, normal force, and shear force. These values were found at standard atmospheric values, defined as 2,116 $\frac{lb_f}{ft^3}$ and 68.09 °F. The values for the normal force were found to be fairly consistent throughout the simulation, with a range from approximately 150 lb_f to 200 lb_f. The CFD simulator was also used to calculate approximate values for the coefficient of drag. The

primary goal of this was to assist in the minimization of drag on the rocket. A SolidWorks Tutorial[8] guide was sought out for assistance. The tutorial contained detailed instruction on how to calculate the drag coefficient (C_d) for a cylinder. Below is the reconstructed cylinder that was used in the tutorial.

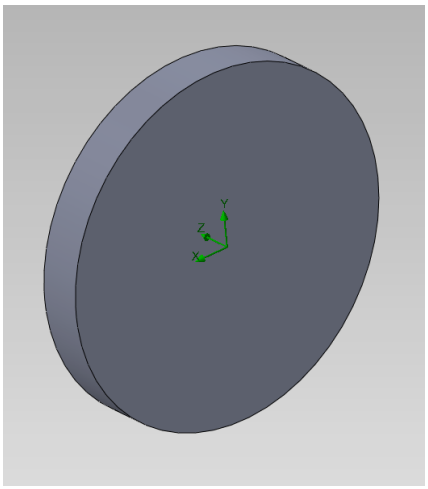

Figure 4.6. Cylinder Test Case Replica[7,8]

The values from the tutorial were closely reproduced, with slight differences in the exact numerical values. The method that the tutorial used for C_d calculation involved finding the velocity by using the Reynolds number. The formulas the tutorial used can be seen below:

$$V = \frac{Re * \mu}{\rho * Length} \tag{4.17}$$

$$C_d = \frac{Y\text{-}Component\ of\ Force}{\frac{1}{2} * \rho * V^2 * A} \tag{4.18}$$

In Equation 4.17, the Reynolds number was represented as "Re" and the dynamic viscosity was represented as "μ." The density of air was represented as "ρ" and the length of the rocket was used for the "Length." In Eqn. 4.18, the "Y-Component of Force" was the SolidWorks representation of the drag force, and the area A was considered to be the projected surface area of the rocket. With the knowledge from the tutorial, several new flow simulations were performed on the rocket model. The simulations yielded an approximate value for the C_d, using the above equations. The value was found to be approximately $C_d = 0.4$ with a drag force of approximately 130 lb_f. The simulation was run several times, and each time, the values were consistently similar. The program was also used to run a simulation for the fins to find the amount of force that can be expected to act on the rocket. Below are images that were the results of the flow simulation.

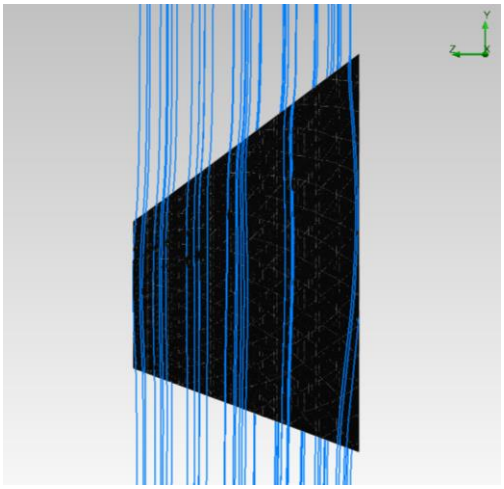

Figure 4.7. 65-006 CFD results.[7]

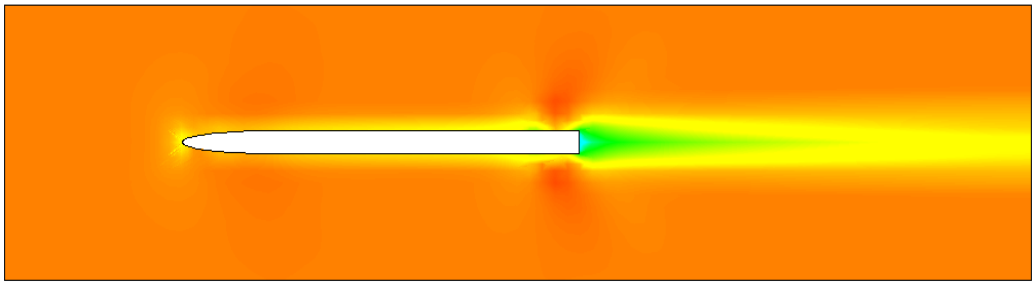

Figure 4.8 Dynamic Pressure using Eqns. 4.7.1. and 4.7.2.[7]

The CFD simulations were successful in developing approximate values for the drag coefficient, and the forces that may be experienced by the rocket during flight. A future goal of the CFD would be to develop a coefficient of lift and analyze "side" forces. This information may prove to be critical in ensuring the rocket flight is successful. Further analysis from Wind Tunnel testing will also help in bringing clarity to the CFD analysis.

4.8. References

[1]Barrowman, J. S., et al. "An Improved Theoretical Aerodynamic Derivatives Computer Program for Sounding Rockets." *Sounding Rocket Technology Conference, 5th, Houston, Tex., March 7-9, 1979, Technical Papers. (A79-25751 09-12)* New York: American Institute of Aeronautics and Astronautics, 1979. 111-120. *Aerospace Research Central.* Web. 9/26/2013.

[2] Mandell, Gordon K.; Caporaso, George J.; Bengen, William P.,"Topics in Advanced Model Rocketry"; The MIT Press; 1973

3Stoney,William.., "Transonic Drag Measurements of eight body-nose shapes", NACA RM l53K17, 5 February 1954

[4] Perkins, Edward. Jorgensen, Leland. **"**Investigation of the drag of various axially symmetric nose shapes of fineness ratio 3 for Mach numbers from 1.24 to 3.67", NACA RM A52H28, 6 November 1952

[5]Military Handbook: "Design of Aerodynamically stabilized free rockets".

[6]MATLAB , 2013 ed.

[7]SolidWorks, 2012 ed.

[8]SolidWorks., "SolidWorks Flow Simulation 2012 Tutorial," 2012.

[9]Benson, Tom., "Size Effects on Drag," *National Aeronautics and Space Administration*, NASA, 28 Jul 2010, URL: http://www.grc.nasa.gov/www/k-12/airplane/sized.html [cited 8 November 2013].

[10]"The Aerodynamics of Model Rockets Part 2 – Parasite Drag and Airflow Types,"*Sigma Rockets*, Sigma Rockets, May 2011, URL: http://www.sigmarockets.com/blog/2011/05/the-aerodynamics-of-model-rockets-part-2-parasite-drag-and-air-flow-types/ [cited 8 November 2013].

5. Recovery

5.1. Objective

The recovery system is designed to safely return the rocket to the ground after apogee. The system must have multiple descent retardation devices as per the rules because the main device cannot be deployed at the apogee.

Parachutes were chosen for the recovery system due to their dominance for rocket recovery. Other recovery options would require extra fuel, power, or would not slow the rocket down and merely display its location. The simplest multi-stage parachute system consist of a drogue and main parachute

5.2. Drogue

The essential parameter for the decent calculations is the weight of empty rocket, which is estimated to be 47 pounds.

$$Force\ Drag = \frac{1}{2} C_D \rho V^2 A = W \qquad (5.1)$$

where ρ is the density of the air at apogee, 10,000 feet, V^2 is the terminal velocity of the rocket, A is the flat sheet area of the parachute, C_D is the coefficient of drag of the 2D layout of the parachute, and W is the rocket weight without fuel. An important parameter to note is that the drag coefficient is for the flat pattern of the parachute, not the open diameter. This flat pattern diameter, d_o, can be calculated from area with Equation 5.1.

$$\sqrt{\frac{4A}{\pi}} = d_o \qquad (5.2)$$

Area can be calculated with the use of all the other parameters in Equation 5.1 and through Equation 5.2 diameter can be deduced. These parameters and the solution for area can be seen in Table 5.1 for the drogue parachute.

Table 5.1. Parameters for the Drogue Rotafoil Parachute

Parameter	Units	Value
C_D		0.85
V	ft/s	55
ρ	$slug/ft^3$	0.001756
W	lb	47
A	**ft^2**	**20.8**
D_o	**ft**	**5.15**

A rotafoil style parachute was chosen for the drogue because it produces a high coefficient of drag with a low oscillation angle, 0 to 3 degrees. Figure 2.3.1 displays the sizing of a rotafoil gore, or section of the parachute. 8 gores were chosen for the rotafoil as less number of gores increases the effectively of the drag. The slot shown in Figure 5.1 is approximately 80% of the area of the gore.

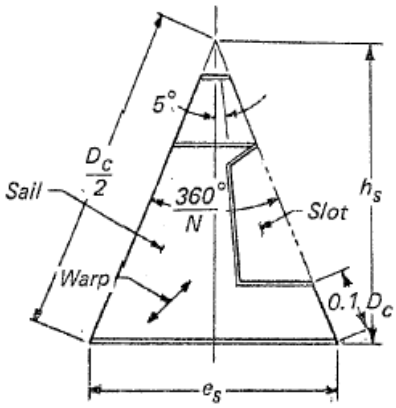

Figure 5.1. Gore layup template. [4]

Equations 5.3 and 5.4 are used to calculate the parameters for the gore, with N being the number of gores.

$$h_s = \sqrt{\frac{A}{N\ tan(\frac{180^\circ}{N})}} \tag{5.3}$$

$$e_s = 2h_s\ tan\left(\frac{180^\circ}{N}\right) \tag{5.4}$$

The vent hole gore length, e_v, is 20% of the outer gore length, e_s. Sizing for this gore can be seen in Figure 5.2.

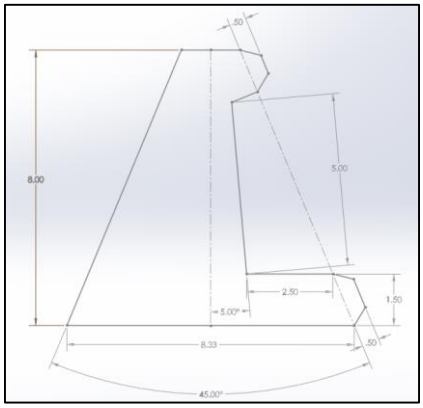

Figure 5.2. Rotafoil gore sizing.

5.3. Main

The main parachute will be a conical extended skirt, which will deploy at 800 feet, giving 300 feet for full opening to allow a safety margin of slow descent. As large rotafoils are not feasible, a conical parachute with an extended skirt was chosen for its high coefficient of drag. Parameters for this parachute can be seen in Table 5.2.

Table 5.2. Parameters for the Main Parachute.

Parameter	Units	Value
C_D		0.85
V	ft/s	18
ρ	$slug/ft^3$	0.00233
W	lb	47
A	**ft^2**	**146.5**
D_o	**ft**	**13.66**

The size of the main parachute can be obtained by plugging in the values from Table 5.2 into Equations 5.1 and 5.2 to get a diameter of 14.8 feet. This diameter is the flat-pattern diameter of the parachute, with the open diameter being much lower. Figure 5.3 displays the data this drag coefficient is from.

TYPE	CONSTRUCTED SHAPE PLAN	CONSTRUCTED SHAPE PROFILE	$\frac{D_c}{D_o}$	INFLATED SHAPE $\frac{D_p}{D_o}$	DRAG COEF C_{D_o} RANGE	OPENING FORCE COEF C_X (INF MASS)	AVERAGE ANGLE OF OSCILLATION, DEGREES	GENERAL APPLICATION
FLAT CIRCULAR			1.00	0.67 TO 0.70	0.75 TO 0.80	~1.7	±10 TO ±40	DESCENT, OBSOLETE
CONICAL			0.93 TO 0.95	0.70	0.75 TO 0.90	~1.8	±10 TO ±30	DESCENT, M < 0.5
BICONICAL			0.90 TO 0.95	0.70	0.75 TO 0.92	~1.8	±10 TO ±30	DESCENT, M < 0.5
TRICONICAL POLYCONICAL			0.90 TO 0.95	0.70	0.80 TO 0.96	~1.8	±10 TO ±20	DESCENT, M < 0.5
EXTENDED SKIRT 10% FLAT			0.86	0.66 TO 0.70	0.78 TO 0.87	~1.4	±10 TO ±15	DESCENT, M < 0.5
EXTENDED SKIRT 14.3% FULL			0.81 TO 0.85	0.66 TO 0.70	0.75 TO 0.90	~1.4	±10 TO ±15	DESCENT, M < 0.5

Figure 5.3. Typical infinite mass force-time history of a solid cloth parachute in a wind tunnel.[2]

Since the shock of deploying the parachute will not be significant, 12 gores were chosen as to give a large enough safety factor without having an extremely high probability of the cords getting tangled. Further analysis will need to be done on this exact safety factor and gore material. A preliminary look at materials leans towards Ripstop for the parachute, but there are lighter, less strong materials that might also work with an acceptable factor of safety. A gore for the main parachute can be seen in Figure 5.4.

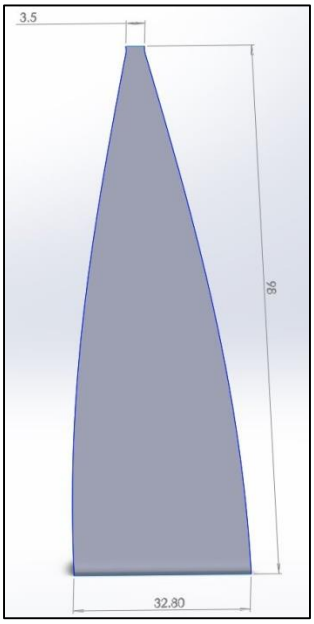

Figure 5.4. Gore for main parachute.

5.4. Deployment

After multiple design iterations, it was decided to use and explosive cup charge for the initial deployment of the drogue chute. This cup charge will be made from two different sized brass shell casings: 45 and 40 caliber ACP shells. 6 or 7 grains of black powder will be used for initial ground tests. The reasoning behind using a cup charge is that this system will provide a way to direct all of the ejection forces from black powder detonation onto one concentrated area at exactly the same time. This will ensure more consistent nosecone ejection and full deployment of the drogue and subsequently the main chute.

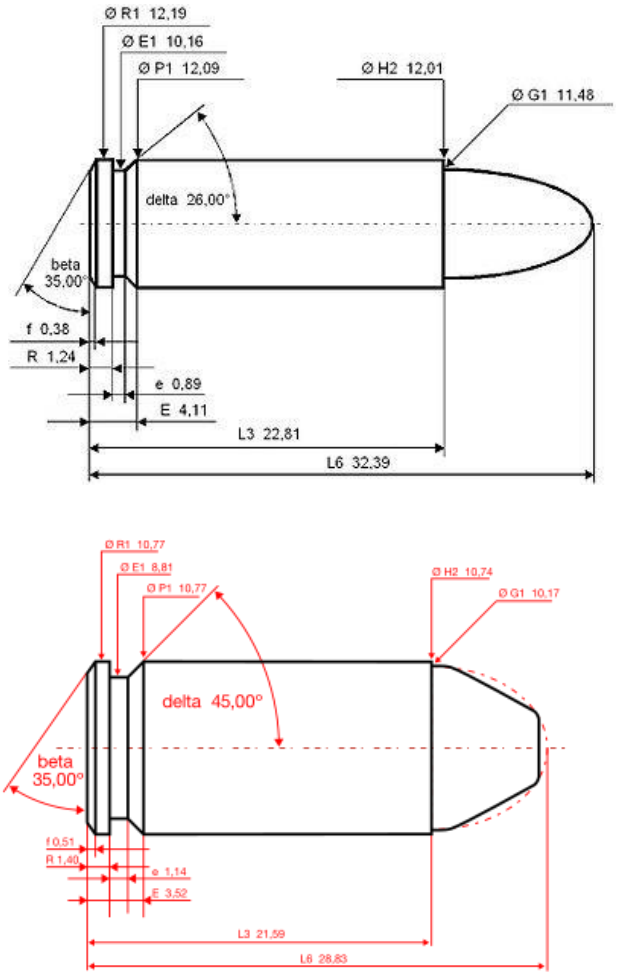

Figure 5.5. Bullet Casings

A sheet of birch plywood approximately 5/8 of an inch thick will be placed between the cup charge and the parachute to protect it from heat produced by the explosion. Ejection forces will be directed against the recovery bulkhead, resulting in normal forces against the birch plywood which will push the nosecone and parachute assembly out of the body tube.

5.4.1. Two-Stage Deployment

Parachute deployment will consist of two stages: the drogue and main chute. The drogue will be deployed at apogee, ideally 10,000 ft. The explosive cup charge will initiate the first stage deployment. The second stage will be deployed through use of drag on the drogue chute. The defy gravity tether will be used to hold the paracord together, until a predetermined altitude at which a small directed charge will separate the links, allowing the main chute to leave the body tube.

Figure 5.6. Defy Gravity Tether

5.4.2. Deployment Forces

The cords and material for the parachute are determined based off of the stress induced when the parachute is opening. Initial calculations based off horizontal opening equations put this opening force of the main parachute, which will be the largest decrease in speed, at 775 pounds. This value seems large; however, it is for a parachute opening within 0.14 seconds when the rocket is traveling at 55 ft/s. The recovery bulkhead is therefore being designed to handle 1000 pounds, which should factor in the discrepancies between horizontal and vertical opening forces. The largest opening force comes after the parachute is fully opened, as seen in Figure 5.7.

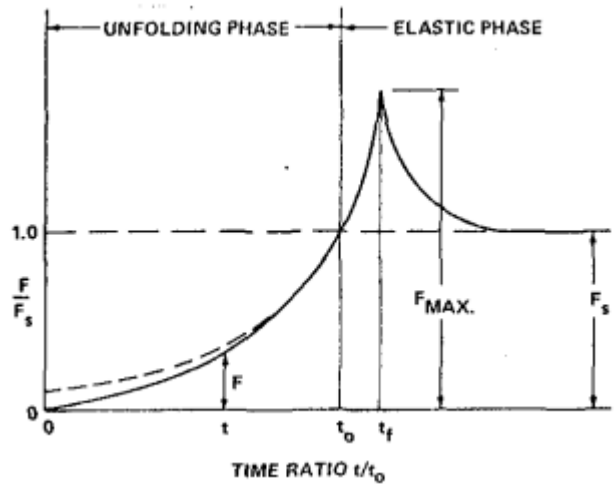

Figure 5.7. Opening Forces of a Parachute

The equations used to calculate this force can be seen below. As previous stated, these are for horizontal opening force. Vertical opening forces are slightly greater but more difficult to converge too and are still being analyzed.

Equation 5.5 represents the steady-state drag force of the fully open parachute at the line stretch velocity, V_s [3]. This velocity will still be the velocity the drogue parachute is keeping the rocket at the moment the main parachute is deployed.

$$F_s = \frac{1}{2}\rho V_s^2 C_D A \tag{5.5}$$

To calculated the ballistic mass ratio which will be used to scale the opening force, the inflation time, t_o, must be calculated as seen in Equation 5.6.

$$t_o = \frac{2W}{\rho g V_s C_D A}\left[e^{\frac{g\rho V_o}{2W}\left[\frac{C_D A}{A_{Mo} - A\,k\sqrt{\frac{C.P.\rho}{2}}}\right]} - 1\right] \tag{5.6}$$

V_o is the steady-state canopy volume of the air to be collected, A_{mo} is the canopy mouth steady-state area, k is the canopy cloth airflow coefficient, and C.P. is the average pressure coefficient. The values for k and C.P. are estimated to be 1.46 and 1.7 respectively from MIL-C-7020 material, a type of Ripstop Nylon [3]. The equation to calculate V_o is Equation 5.7.

$$V_o = \frac{2}{3}\pi \bar{a}^3 \left[\frac{b}{\bar{a}} + \frac{b'}{\bar{a}}\right] \tag{5.7}$$

The parameters for this equation are estimated the flat circular, 12 gore row seen in Table 5.3 [3].

Table 5.3. Summary of Parachute Shape Test Results. [3]

Parachute Type	No. of Gores	Suspension Line Length inches	Velocity mph	Velocity fps	Scale Factor, K $\frac{2\bar{a}}{D_o}$	$\frac{2\bar{a}}{D_F}$	$\frac{2\bar{a}}{D_R}$	$\frac{2\bar{a}}{L}$	$\frac{N}{\bar{a}}$	Axes Ratio $\frac{b}{\bar{a}}$	$\frac{b'}{\bar{a}}$	$\frac{b}{\bar{a}}+\frac{b'}{\bar{a}}$	Volume in^3 V_H	V_C	V_o	$\frac{V_o}{V_H}$
Flat Circular	12	34	50	73	.645	.650			.856	.6115	.8817	1.4932	4476	4481	6980	1.56
	16	34	50	73	.663	.669			.820	.5558	.9039	1.4597	4450	4100	7325	1.65
10% Extended Skirt	12	34	100	147	.663	.652			.881	.6424	.8860	1.5284	3928	4400	6783	1.73
	16	34	17	25	.654	.640			.785	.5580	.8502	1.4082	4051	3920	6197	1.53
Elliptical	12	34	75	110			.916		.812	.5626	.9657	1.5283		3322	5405	
	16	34	17	25			.875		.800	.6169	8163	1.4332		2726	4405	
Hemispherical	12	34	125	183			.996		1.254	1.0005	.9080	1.9085		6224	8666	
	16	34	75	110			.994		1.185	.9129	.9380	1.8509		5921	8370	
Ringslot 16% Geometric Porosity	12	34	25	37	.607	.654			.853	.6566	.8735	1.530	3800	3650	5903	1.55
	12	34	100	147	.616	.663			.922	.6566	.8735	1.530	3800	4198	6196	1.62
	12	34	200	293	.637	.686			.918	.6566	.8735	1.530	3800	4624	6826	1.90
	16	34	25	37	.611	.658			.827	.6004	.8890	1.4894	3800	3763	5685	1.50
	16	34	100	147	.617	.664			.864	.6004	.8890	1.4894	3800	3985	6030	1.59
	16	34	200	293	.645	.695			.844	.6004	.8890	1.4894	3800	4430	6897	1.82
Ribbon 24% Geometric Porosity	12	34	25	37	.586	.632			.859	.6558	.8768	1.5326	3800	3323	5335	1.40
	12	34	100	147	.615	.663			.837	.6558	.8768	1.5326	3800	3714	6163	1.62
	12	34	200	293	.632	.681			.877	.6558	.8768	1.5326	3800	4280	6883	1.76
	16	34	25	37	.603	.650			.797	.5570	.8578	1.4148	3800	3438	5358	1.41
	16	34	100	147	.626	.674			.791	.5570	.8578	1.4148	3800	3804	5983	1.57
	16	34	200	293	.648	.698			.781	.5570	.8578	1.4148	3800	4164	6656	1.75
Cross Chute W/L = .264		34	25	37	.710			.543	1.242	.8867	1.2776	2.1643	1928	3768	5798	3.01
		34	100	147	.707			.540	1.270	.8867	1.2776	2.1643	1928	3810	5712	2.96
		34	200	293	.716			.547	1.285	.8867	1.2776	2.1643	1928	4212	5925	3.07
		47	25	37	.759			.580	1.113	.8494	1.2512	2.1006	1928	4052	6868	3.56
		47	100	147	.729			.557	1.205	.8494	1.2512	2.1006	1928	3973	5958	3.09
		47	200	293	.775			.592	1.110	.8494	1.2512	2.1006	1928	4292	7303	3.79

REPRODUCED FROM REFERENCE (6)

Using the above parameters, the area of the mouth can also be found from Equation 5.8.

$$A_{Mo} = \pi\bar{a}^2\left[1 - \left(\frac{N/\bar{a} - b/\bar{a}}{b'/\bar{a}}\right)^2\right] \quad (5.8)$$

The above variables can be used to calculate the inflation time which comes out to be around 0.14 seconds. This is then used to find the ballistic mass ration which leads to the scaling factor for peak force seen in Equations 2.3.9 and 2.3.10.

$$M = \frac{2W}{\rho g V_s t_o C_D S_o} \quad (5.9)$$

$$X_{i_{max}} = \frac{16}{49}\left(\frac{21M}{4}\right)^{6/7} \quad (5.10)$$

This finally leads to calculating the maximum opening force for horizontal deployment as seen in Equation 2.3.11.

$$F_{max} = X_{i_{max}} F_s \quad (5.11)$$

For this application, Ripstop Nylon was chosen as the material for the parachute. With a weight of 0.015lbs/square foot, the parachute weights are shown below in Table 5.4.

Table 5.4. Parachute Weights

Parachute	Weight
Main	3.4
Drogue	0.5

The cords connecting the gores of the parachute to the main shock cord of the parachute are the other important item. These lines will be made of nylon rope, with a length of twice the diameter of the respective parachute, as shown effect in Figure 2.3.6.

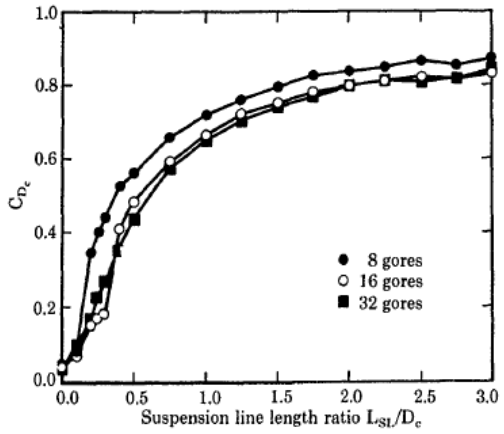

Figure 5.8. Optimal Line Lengths for Coefficient of Drag of Parachute [4].

With these parameters chosen, the parachute can cut out and double stitched for strength, and attacked to the rest of the recovery system after more analysis is done on vertical parachute opening forces.

5.5. Fabrication and Testing

Fabrication of the recovery system will begin as soon as possible after school starts on January 13th. Guidelines given by Doctor Pollock about deciding the amount of black powder needed include beginning with 6 or 7 grains of Unique brand gun powder and increasing or decreasing the test amount by one grain for subsequent tests. Another important consideration during body tube fabrication for the area underneath the nosecone is to ensure that it is properly ventilated. This means drilling holes in the tube itself using a dremel with conical cone Redstone. Epoxy will be needed to reinforce the holes and prevent further shearing, as well as tape on the inside and outside of each hole. Currently, two holes are being planned for insertion on opposite sides of the body tube.

Ground testing will begin as soon as possible after fabrication of the body tube, cutting of the plywood, and construction of the cup charge. The goal for the first ground test has been set for February 7th, with testing taking place every weekend for the rest of that month with the goal of finalizing the design and sizing of the black powder by early March.

5.6. References

[1]Knacke, T.W. *Parachute Recovery Systems*. Santa Barbara, CA: Para Publishing, 1992. Print.

[2]Ludtke, W.P. *AIAA 4th Aerodynamic Deceleration Systems Conference Palm Springs, CA*. Silver

[3]Spring, MD: American Institute of Aeronautics and Astronautics, May 21-23, 1973. Print.

[4]Ludtke, W.P. *Notes On A Parachute Opening Force Analysis Applied To A Vertical Toward-The-Earth Trajectory*. Underwater Systems Department, Naval Surface Weapons Center, May 1987. Print.

[5]Peterson, C.W. and Maydew, R.C. *Design and Testing of Higher-Performance Parachutes.* North Atlantic Treaty Organization. Nov. 1991. Print.

6. Electronics and Instrumentation

6.1. Objective

There are three main objectives that must be met by the electronics system constructed. First, the system must be able to control engine cutoff and fully deploy all parachutes at key altitudes. Second, the system must be able to transmit and record the rocket's trajectory therefore providing the location for recovery. Lastly, there will be a set of independent electronics such as camera and strain gauge for payload study.

6.2. Instruments

6.2.1. Configuration

Following a fail-safe approach commonly used in industry, the rocket utilized redundant sensing systems. Additionally, these systems adhere to strict requirements from the ESRA (Experimental Sounding Rocket Association). Based on researched configurations and power restraint analysis, the optimal balance between reliability and power consumption was found to be a dual altimeter configuration with separate power circuits. In addition, a tracking system will also be used for the purpose of locating the rocket for retrieval. A GPS device was decided to be the optimal choice, as opposed to the transmitter provided by the ESRA.

Regarding the altimeters, research and analysis narrowed down hardware options to three components. One of the components used will be the PerfectFlite Stratologger. This altimeter is cheaper than the alternatives, and requires one less battery than the other two, which reduces weight. The second altimeter used will be the G-wiz HCX, with the G-wiz LCX as an acceptable alternate. These altimeters are similar, with the HCX being slightly more advanced, but also more expensive. Keeping efficiency in mind, the HCX was chosen as the primary altimeter and the Stratologger as the secondary. A programmable computer (BeagleBone BeagleBoard Black) will be included as well to join and control several of the electronic devices. These components were found to have the greatest reliability in their class and fulfilled the necessary constraints stated in the objective.

6.2.2. Altimeters

6.2.2.1. PerfectFlite Stratologger

The Perfectflite Stratologger is a relatively cheap and reliable barometric altimeter/flight computer. It provides two pyrotechnic outputs for the charges of the drogue and main parachute deployment. The downside to this system is that there is only one power input for both the pyrotechnic charges and the flight computer. Due to this, there is a possibility that the pyrotechnic charges could consume most of the power causing the flight computer to malfunction. Since this component is used as a back-up flight computer, the battery will be tested to ensure the power level, and ultimately, the reliability of the component. The user interface is designed to be simple, utilizing a USB adapter to change deployment altitudes and view recorded data.

Table 6.1. PerfectFlite Stratologger specifcications.

PerfectFlite Stratologger	
Primary Sensing Method	Barometric
Secondary Sensing Method	N/A
Samples per second	20
Required Voltage	4-16 Volts (9V nominal)
Dimensions	2.75"L x 0.9"W x 0.5"H
Price	$71.95

6.2.2.2. G-wiz LCX

The G-wiz LCX is a mid-tier flight computer that combines certain reliability features of an upper-tier flight computer with the affordability and simplicity of a lower-tier altimeter. The G-wiz LCX has three pyrotechnic outputs. It also has two separate inputs for the pyrotechnic and CPU batteries. This allows the CPU to be completely independent of the pyrotechnic power usage. A main feature of this flight computer is the use of a barometer to determine altitude, while utilizing an accelerometer to verify the barometric measurements. To verify launch, the CPU gives priority to the accelerometer engaging the barometer once the rocket has accelerated past a certain threshold. A similar procedure occurs during the horizontal orientation at apogee.

Table 6.2. G-wiz LCX specifications.

G-wiz LCX	
Primary Sensing Method	Barometric
Secondary Sensing Method	Accelerometer
Samples per second	20-500
Required Voltage	9V (max 15V)
Dimensions	3.9” x 0.7” 0.5"H
Price	$134.95

The accelerometer requires the entire device to be positioned vertically in order to function correctly. The user interface of this unit contains many options for data transfer, recording, and storing, which makes it slightly more complicated than the PerfectFlite Stratologger. Also, altitudes for the deployment of the pyrotechnic charges can be configured. To access the altimeter data, an external device connects to the altimeter and then is connected, using an adapter, to a computer via USB.

6.2.2.3. G-wiz HCX

The G-Wiz HCX is a high-end altimeter/flight computer capable of data logging, thrust characterization, and optional telemetry downlink capabilities. Another feature is the four pyrotechnic outputs, which provides back-up charges, which would ensure that the ejection charge will ignite. This method does not protect against an altimeter malfunction, but it adds a second level of reliability to the altimeter/flight computer. The HCX and LCX are manufactured by the same company, creating similarities between them. The user interface, two power inputs, and sensing relationship of these two units are similar. This allows for simplicity when dealing with a primary altimeter and a secondary altimeter.

Table 6.3. G-wiz HCX specifications.

G-wiz HCX	
Primary Sensing Method	Barometric
Secondary Sensing Method	Accelerometer
Samples per Second	66.67-500
Required Voltage	9V (Max 12V)
Dimensions	5.5" L x 1.1" W x 0.903" H
Price	$234.95

6.2.2.4. Atlus TeleMetrum

The Atlus TeleMetrum is a very capable flight computer. This device includes a barometer, accelerometer, GPS, and a telemetry transmitter. At the basic level, the TeleMetrum can function as a dual-deploy altimeter that is similar to the PerfectFlite Stratologger, G-wiz LCX and HCX. The telemetry transmitter allows the ground team to record data, track the rocket on a directional basis, and send commands to the CPU for emergency shut-off or user-prompted parachute deployment. The safety benefits this provides cannot be overstated.

Table 6.4. Atlas TeleMetrum specifications.

TeleMetrum	
Primary Sensing Method	Barometric
Secondary Sensing Method	Accelerometer
Tertiary Sensing Method	GPS
Required Voltage	9V (Max 12V)
Dimensions	1" W x 2.75" L X 0.62" H
Price	$400.00

To operate the radio downlink/uplink, a member of the ground team would need a HAM radio license. The receiver used is a 70cm ham-band for frequencies of 144 and 440 MHz. It transmits 10 samples per second back to the ground team. As for the GPS capability, this would allow for extreme ease and reliability when recovering the rocket. The CPU records one GPS sample per second. This is not entirely useful for telemetry tracking. However once the rocket has landed and is not moving, one sample per second for finding the rocket is feasible. The CPU also generates a KML file so that the trajectory of the rocket can be viewed in Google Earth.

6.2.3. Programmable Computer

6.2.3.1. BeagleBone BeagleBoard-Black

This computer is one of the cheapest and most reliable boards on the market. At $45, this device can be upgraded to perform as well or even better than commercially made altimeters/flight computers. The native operating system is Ubuntu; however this system can also run on Android 4.0. The BeagleBone Black sports an AM335x 1GHz ARM®

Cortex-A8 processor allowing Ubuntu to boot in less than 10 seconds. The board contains two 46 inch pin headers, an HDMI output, and USB connectivity. This programmable computer will be used to manage several of the electronics used on the rocket such as the shutoff servo, strain gauge for the payload, camera for the payload, and any future electronic additions.

6.2.4. Tracking device

6.2.4.1. Transmitter

As mentioned in 6.2.1, the ESRA supplies a transmitter through the Bridgerland Amateur Radio Club. The transmitter they use is the BeeLine Transmitter. They collect a $75 deposit fee that is returned when the undamaged transmitter is returned to them. They also supply other components used to track the rocket such as an antenna and receiver. The entire unit is less than 1" x 2" and weighs less than one ounce. The transmitter can be programed to operate on any frequency between 420 and 450 MHz. This system has been proven to work in the past, does not require a radio license, and is reliable.

6.2.4.2. GPS

The BRB 900 consists of a 900 MHz spread spectrum transmitter and matching receiver with a USB interface. With this system it is possible to monitor the GPS data stream in real-time. The transmitter has a non-volatile memory to record in-flight data that can be viewed later in Google Earth. The rate for data can be chosen, and up to 2 ½ hours may be saved at a frequency of 1Hz. This system costs $230. This option has an advantage of being able to be tested prior to the competition.

6.3. Power

There are different kinds of batteries that will be used to power the electronics onboard the rocket. There are two main constraints that limit the choice in powering the electronics. First, the Aerospace Department has a restriction that does not allow for the use of lithium polymer batteries. Secondly, the ESRA rules states that each electronic component that is "critical to safe operation and recovery of the rocket" must have its own independent power source. In light of this, altimeters, the GPS unit, and the BeagleBoard will each run on independent power sources. The PerfectFlite Stratologger will run on a single 9-volt battery. The G-wiz LCX and G-wiz HCX would both run on two 9-volt batteries. The transmitter and GPS are both constructed to run on one 9-volt battery. The BeagleBoard requires a power source of 5V, 500 mA. There are several different ways to supply this power. However, the easiest and more efficient way is through the USB port. There are several battery/battery packs that can be purchased to supply this power. The most advantageous option for this is the Minty Boost, which takes the power from two AA lithium batteries and sends it through a USB connection. The Minty Boost conserves space as it is small in size and costs approximately $25. In total, the batteries required to power the altimeters, GPS, and BeagleBoard are four 9-volt batteries and a Minty Boost adapter with two AA lithium batteries. An additional advantage to using disposable batteries is that they are inexpensive, and having brand new batteries that are sure to be undamaged and fully charged for each launch would be a benefit for the operation of the rocket.

6.4. Electronics Bay Assembly and Wiring

6.4.1. Assembly

The final altimeters chosen to be used were the Perfectflite Stratologger and G-wiz HCX. This combination works very well together. Both of the altimeters will be completely independent and will have separate electric initiators to ignite a black powder ring that will be the ejection charge. The HCX is the most accurate altimeter and should read the apogee first due to its accelerometer. The system will be programed to have the main chute deployed slightly before the Stratologger registers apogee. This way the more accurate altimeter will determine the deployment times, but if it fails, the secondary altimeter will signal for its electric initiator to set off the charge. Both altimeters record altitude and speed for analysis of the flight.

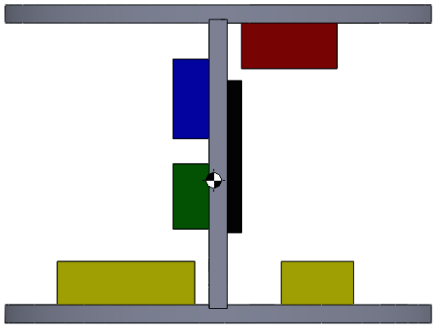

Figure 6.1. Electronics Bay with Center of Gravity.

The final decision was made to use the GPS instead of the transmitter for tracking. The GPS and corresponding battery will be attached to the shock cord that is deployed at apogee with the drogue chute. The GPS must be placed outside of the carbon fiber body so that the RF signals transmitted will not be lost. Because of this we will not be able to track the rocket before apogee; however after apogee it will be "visible". The 9-volt battery connected to the GPS will be attached to the shock cord to eliminate chances of the wire being broken. Both the GPS and battery will be wrapped in ½ inch foam padding to ensure it will not be damaged during ejection or impact with the ground.

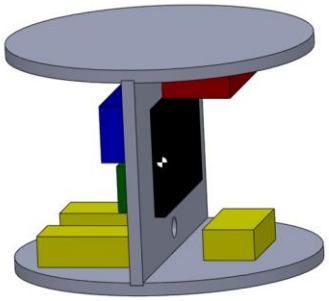

Figure 6.2. E-Bay Ortho-view.

The electronics bay will be the compartment dedicated to holding the majority of the electronics. The design for the "E-Bay" can be seen in **Error! Reference source not found.** and Figure 6.2. The bay will contain both of the altimeters, the BeagleBoard, and all of the batteries other than the 9-volt battery for the GPS. The electronics bay is composed of a circular base of aircraft plywood and a rectangular plate that intersects through the base. The electronics Bay will be screwed to a bulkhead. Electronics outside of the electronics bay include the strain gauge for the payload, camera for the payload, and engine cutoff servo. These three components will be connected to the BeagleBoard. The engine cutoff servo will be located in the plumbing between the oxidizer thank and combustion chamber. The strain gauge and camera will be located in the payload area.

A schematic diagram of how the components (sensors, power supplies etc) will relate to each other can be found in Figure 6.3 and a list of the corresponding components in Table 6.5.

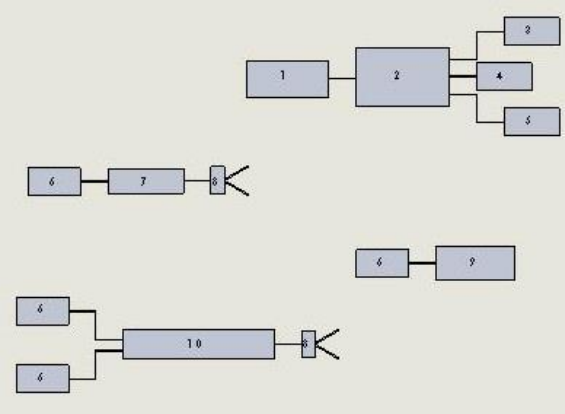

Figure 6.3. Schematic Diagram

Table 6.5. Components of the electronics bay.

Number	Component	Dimensions (in)	Mass (oz)
1	Minty Boost	2.99 x 1.32 x 0.63	1.764
2	Beagleboard Beaglebone Black	3.4 x 2.1 x 0.25	1.4
3	Engine Cutoff Servo	--	--
4	Payload Straingauge	--	--
5	Payload Camera	--	--
6	9-Volt Battery	1.9 x 1.0 x 0.68	3.527
7	PerfectFlite Stratologger	2.75 x 0.9 x 0.5	0.45
8	Electric Initiator	--	--
9	BRB 900 GPS	2.85 x 1.25 x 0.5	1.058
10	G-wiz HCX	5.5 x 1.1 x 0.90	1.587

6.4.2. Wiring

The wiring connecting all of the electronics must conform to the extensive list of requirements given by the Experimental Sounding Rocket Association. Some of these requirements are that 22 gauge wire or larger shall be used, all connections must be insulated, and no soldering is allowed. Wiring that attaches permanently to the structure of the rocket will be installed between the electronics bay and electronic components located in other parts of the rocket. Quick connections will be used at all joints where the rocket disassembles and where each electrical component attaches to the wiring. This will allow for the wiring to stay in place while the rocket will still be able to disassemble. The electronics bay will also be attached to the wiring by quick connections so that it may be taken out to analyze data recorded.

6.5. Testing

Testing of the instruments and their corresponding systems will be a crucial step before the overall rocket is declared launch capable. System testing will take place in stages. Initially, each altimeter will be directed through a series of diagnostics to verify specific components of the altimeter are functioning within acceptable parameters. The pyrotechnic outputs should have a test current of 3.5 mA and a maximum continuous current at initiation of 8 amps per pyrotechnic channel. To test the barometric sensor and accelerometer, simple pressure and movement exercises will be used to confirm the functionality of the sensors. GPS sensors will be tested by comparing their measurement precision to off-the-self devices. After each altimeter/flight computer sub-system is thoroughly tested, a complete system analysis will take place about a month and a half before the first test launch. In this analysis, current and voltage measurements will be acquired at key points in the circuit. These points are before current entrance into the CPU and at the site of the analog ejection charges. If the wiring successfully passes these tests, a full scale ground test will be approved. In the ground test, the rocket will be fully loaded with parachutes, ejection charges, and analogous masses for the motor and payload. The rocket will be placed at a 30 degree angle to the ground and the altimeters will be manually connected to a computer operated by the testing team. A command will be sent by the testing team to the onboard altimeter/flight computer initiating the drogue parachute ejection charge and then the main parachute ejection charge. The testing team will be looking at the processing time of the CPU and the functionality of the ejection charge current. The team will then verify the accuracy of ejection charge and shock cord length calculations.

6.6. References

[1]Lynch-Freshner, M., "G-Wiz HCX User Manual," *G-wiz Website* [Website], URL: www.**gwiz**-partners.com/**G-Wiz_HCX**_User_Manual_1dot1.**pdf** [cited 7 January 2014].

[2]G-Wiz Partners, "G-Wiz LCX User Manual," *G-wiz Website* [Website], URL: www.**gwiz**-partners.com/**LCX**_Manual_v1.1.**pdf** [cited 7 January 2014].

[3]PerfectFlite Partners, "StratoLogger SL100 Users Manual," *PerfectFlite* [Website], URL: http://www.perfectflite.com/StratoLogger%20manual.pdf [cited 7 January 2014].

[4]Coley, Gerald, "Beagleboard:BeagleBoneBlack," *BeagleBone* [Website], URL: http://elinux.org/Beagleboard:BeagleBoneBlack [cited 8 January 2014].

7. Payload

The payload contributes a significant portion of the available points when scoring the rocket; therefor, every effort was made to maximize the payload score. The main goal was to find a way for the payload to be scientifically and technologically significant. This was accomplished by designing the payload to perform a compression/buckling test on a material specimen.

7.1. Design Considerations

There were several design criteria that had to be met to qualify the vehicle for competition. First, the payload must weigh at least 10.0 lbf. Judges will weigh payloads to verify this criterion is met. Second, the payload must be removable. Access to the payload must be accommodated such that the payload can be removed from the rocket. Additionally, the payload must be able to be replaced with a ballast of the same mass and form factor without affecting the rocket's trajectory or altitude. Third, the payload must not separate from the vehicle and must survive launch and recovery loads. These constitute the non-negotiable requirements set for the payload by the competition.

The payload judging sheet has several categories of evaluation, shown in Figure 7.1. These criteria do not represent non-negotiable requirements for the payload; an inability to capture all the points in each category will not disqualify the vehicle. However, a high degree of success in each evaluation criterion is obviously desirable.

Criterion	Maximum Points
Scientific/Technical Objectives Scientific or technological relevance, how well experiment will provide answers, number of different experiments/objectives	250
Professional Construction Quality construction methods, aerospace-grade wiring and hardware	100
Deliverables Poster, handouts	150
Student Design and Construction How much of payload is designed and built by student team versus purchased/built by others	100
Flight Objectives Met Payload provided the desired data	200
Organizational Backers/Sponsors Did an external sponsor propose the experiment, have an interest in the outcome, and/or provide resources to help the team build the experiment?	100
Readiness "Turnkey" operation or lots of last-minute adjustments/modifications?	100
Bonus for K-12 Payload University students as mentors only	100
Total + Bonus	1000+100

Figure 7.1. The judging sheet for the official evaluation of the payload is shown.

7.2. Fabrication Analysis

To fabricate the payload, the aluminum plunger sleeve would be created first. This would be machined out of a 5-inch diameter, 6-inch long rod. This rod would be cut to a length of 4.5 inches. The outer diameter would be turned down to a diameter of 4.75 inches, and the ends of the rod would be faced off. A hole of 0.75 inches in diameter would be drilled into the middle of the part, and the outer profile of the part would be created.

After this, the loading platform to be connected to the buckling specimen would be fabricated. Again, this would be created out of a 5-inch diameter rod. Again, the outer diameter would be turned down to the dimension of the plunger sleeve. The majority of the depth of the center of this rod would be bored out leaving a long lip. The center of this lip would be grooved for a piston-seal ring.

A piece of aluminum shim stock would be folded into a cylinder around the loading platform and the aluminum plunger sleeve. This would be coated in Alodine to mitigate galvanic corrosion with the carbon fiber. Carbon fiber would then be laid up on top of this aluminum piece to create a large cylinder with caps. A window would be cut out of this aluminum piece using a Dremel tool. The seam in the aluminum shim stock would be sealed using epoxy, then excess would be sanded off to leave a perfect cylinder. Then, mounting holes would be drilled into the bottom of the payload to mount the payload to the bulkhead.

7.3. Instrumentation

Instrumentation is needed to collect data for the experiment. Ideally there will be a strain gauge on the specimen that will be connected to an onboard computer to collect the data.

7.4. Testing

The objective of testing of the payload will be to ensure we can capture data from the experiment and that the payload will not jeopardize the structure and performance of the rest of the rocket. In flight the g forces from the rockets accent on the free weight will apply a force to the specimen. To simulate this, the payload will be setup with strain gauge attached and force will be manually applied by hand to the free weight. This will not necessarily account for all the vibrations present in actual flight, but that is difficult to simulate.

The main hazard with the payload system is the piston assembly. To ensure the piston assembly does not leak at all, 1.5 times the loading expected to see in flight will be applied to the free weight.

The payload is a non-critical system, and as such it will be fabricated and tested after other more important rocket systems. There is a preliminary testing date of February 28, 2014.

8. Vehicle Structure

8.1. Objective

The vehicle structure needs to withstand all loads from take off, flight, and parachute deployment. The main structure of the rocket is the body tube that surrounds all the internal components. Between the body tube sections are connectors to keep it all together. In addition to the connectors, there are also several bulkheads to help transfer the loading from take off and recovery to the body tube.

8.2. Body Tube

The body tube is the structural skeleton of the rocket, of paramount importance and critical to mission success. This structure must survive the forces at launch of 350 lbf in compression, as well as the main chute deployment of 1000 lbf in tension. Each segment of the body tube must be less than 36 inches in length to allow accessibility of the interior components. The cross-section shape is circular due to aerodynamic considerations.

8.2.1. Structural Analysis

In order to avoid buckling the structure during launch, hand calculations were used to determine a preliminary thickness of the body tube cylinder wall. Due to the high slenderness ratio, the Eulerian buckling formula shown below was used.

$$F_C = \frac{\pi^2 EI}{(KL)^2} \tag{8.1}$$

An inner diameter of 6.0 inches and a thickness of 0.030 inches were assumed. The modulus of elasticity was assumed to be that of +45/-45 carbon fiber. This material was selected for the airframe due to its higher tensile and compressive loading capacities compared to those of fiberglass. Using this equation, the critical load was determined to be 7,450 lbf. This seemed to be an abnormally high value, so a finite element analysis buckling study was run to provide further insight. Since carbon fiber properties are nuanced, the buckling study was run with aluminum as the choice material to determine if such a thin structure is actually as strong as the hand calculations seemed to indicate. With a factor of safety of 8.1 (resulting from an applied load of 315 lbf), an aluminum structure with the aforementioned geometry would more than suffice.

Another failure-mode considered was compression. Assuming a compressive strength of 230 ksi[*], the critical load was found to be 122 kip. This is larger than the compressive force the rocket will experience at launch, and thus the assumed thickness dimension exceeds the design requirements with significant margin of safety.

8.2.2. Manufacturing Plan

In order to manufacture the body tube, Toray T700SC 24k carbon fiber tow will be used. This will be laid up on a steel tube with a 6-inch outer diameter serving as the mandrel in a filament winder. The filament winder, a Little Hornet filament winder shown in Figure 8.1, is property of Dr. Creasy of the Texas A&M Mechanical Engineering Department.

The mandrel will be sprayed with dry Teflon mold release, wrapped in a sheet of mylar, and then a final coat of mold release will be applied. The layup of the carbon fiber would be performed on top of this coating; once the body tube has been cured in an autoclave, the body tube and mylar sheet should be able to be cleanly pulled off the steel tube mold. Testing must be done to ensure the mylar sheet can survive the bake (research indicates it can).

Figure 8.1. The Little Hornet filament winder is shown with one layer of yarn partially laid up.

[*] Toray T700S Semi-Toughened 350°F Epoxy Resin. Normalized to 60% fiber volume.

The autoclave has a depth capacity of approximately 32 inches. This would be the maximum length of the stainless steel tube used as the mandrel. Approximately 3 inches of this tube would be unused to accommodate the filament winder and handling post-cure. Additionally, the machine lays approximately 3 inches of material on each end that is below 30° of orientation. After the curing process, these excess regions will be cut off using a diamond-coated Dremel cutting wheel. The Dremel tool will be fixed to the tool-holder of a lathe, and the mandrel will be manually spun in the lathe. The depth of cut will be graduated several thousandths of an inch at a time by dialing the tool-holder of the lathe, capable of extreme precision.

A small stand would be manufactured to elevate the tube during the bake, minimizing the length of the autoclave consumed by the stand.

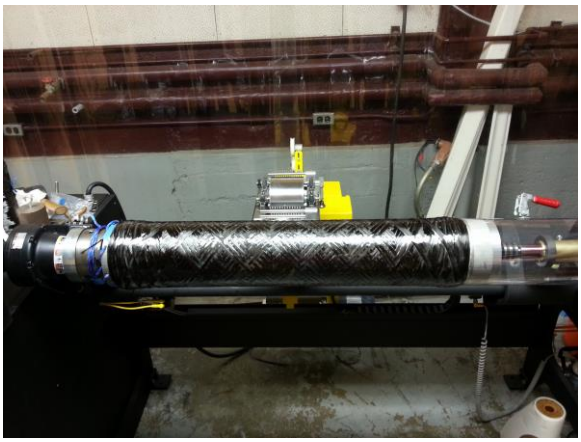

Figure 8.2. Carbon fiber tube laid up and epoxied.

8.3. Body Tube Connectors

The body tube sections of the rocket need to be easily disassembled to allow for access to the payload, engine, oxidizer tank, parachutes, and electronics bay, and the placement of the bulkheads takes these into consideration. The body tube sections of the rocket need to be easily disassembled to allow for access to the payload, engine, oxidizer tank, parachutes, and electronics bay, and the placement of the bulkheads takes these into consideration.

Figure 8.3. Body Tube Connector

The inner diameter of the body tube sections will be adhered to the outer diameter of the body tube connection pieces at the locations specified in Figure 8.3. The two connector sections will then slide inside on another and bolts will secure the two pieces together. The flange and the top of the combustion chamber

that is holding the injector plate will have bolt holes on the outer diameter that will align with the holes seen in Figure 8.3. Bolts will then go through the two connector rings and into the combustion chamber flange. This enable the engine to transfer the thrust through the connector rings into the body tube. A similar connecter will be near the top of the rocket in between the payload and the electronics bay. An important design feature to notice: the bolts will be flush with outer diameter of the ring. They will not be interacting with the air flow across the body tube. The total weight of both pieces of the body tube connection when made of aluminum 6061-T4 is 1.25 lbs.

The adhesive being considered to bond the connector to the body tube is PC-7 epoxy, and it has a tensile shear strength of 2150 psi [1]. The total exposed area of the connector that is being bonded is 18.8 square inches. This gives a total shear strength of 40420 lbs which is much more than the maximum recovery load of 1000 lbs.

8.4. Bulkheads

8.4.1. Engine Bulkhead

The engine bulkhead will be transferring the majority of the thrust to the lower body tube section. The bulkhead can be seen in Figure 8.4. The outer edge will be bonded to the inside of the carbon fiber tube using PC-7 epoxy which has a shear strength of 2150 psi [1]. The eight holes will be bolted to the lower part of the combustion chamber. Analysis of the bolts shows they can withstand the thrust force at takeoff and FEA shows the bulkhead itself will not yield.

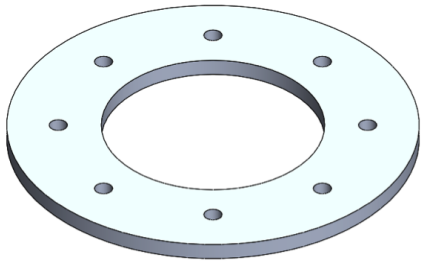

Figure 8.4. Lower Engine bulkhead

8.4.2. Recovery Bulkhead

The recovery bulkhead needs to withstand the impulsive load that the drogue and parachute will create at apogee. Special consideration needs to be made into the connection of the parachute lines to the bulkhead. Failure of this connection would mean detachment of parachutes and most likely the destruction of the rocket. Figure 8.5 show the design of the recovery bulkhead. It is based on recovery bulkheads seen in similar rockets.

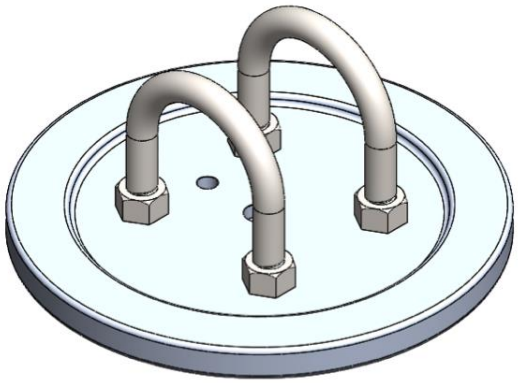

Figure 8.5. Recovery Bulkhead

The parachute lines will be attached to the two steel U-bolts seen in Figure 8.5 The U-bolts are then attached to the bulkhead itself by a thin steel rectangle at the bottom of the bulkhead. The bulkhead will be epoxied to the inside of the body tube.. The adhesive being considered is PC-7 epoxy, and it has a tensile shear strength of 2150 psi [1]. The bulkhead shown in Figure 8.5 has an outer surface area of 5.6 square inches which will corresponds to a shear strength of 12040 lbs assuming a perfect bond. The estimated maximum load on the recovery bulkhead at parachute deployment is 750 lbs., so an estimated factor of safety is about 16. The holes in the middle of the bulkhead provide a potential pathway for any wires that may need to connect electronic components from the nose cone to the lower portion of the rocket. The bulkhead will be machined from Aluminum 6061-T4. The entire estimated weight of this assembly is 1.42 lbs.

Figure 8.6 shows a stress contour map of half of the recovery bulkhead under the maximum expected parachute load of 1000 lb. Half of the load was applied as a pressure over the area of the thin steel rectangle at the bottom of the bulkhead with the other half being taken care of due to the symmetry of the model. A maximum stress of about 8700 psi was seen in the hole at the center of the bulkhead. The yield strength of Al-6061-T4 is 18000 psi [2], so the recovery bulkhead has a factor of safety of about 2.

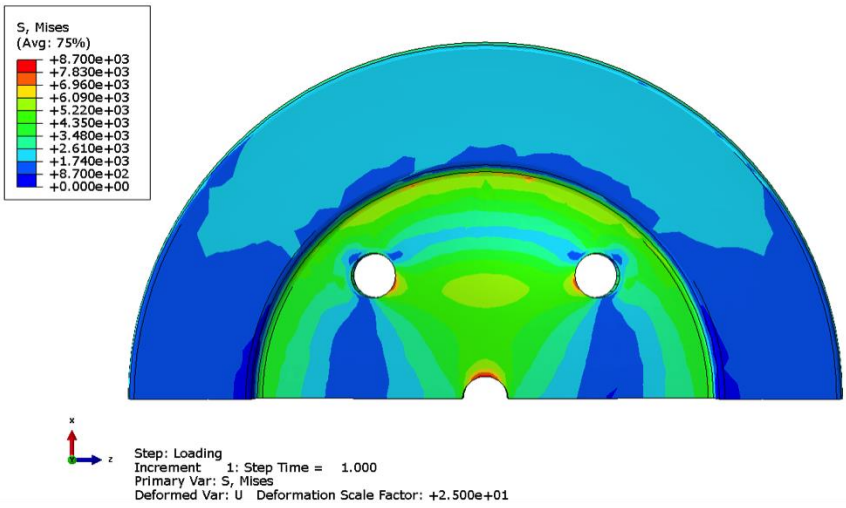

Figure 8.6. Recovery Bulkhead Stress Contours

8.5. Vehicle Fastener Analysis

The highest load seen by this connector is estimated to be 1000 lbs during recovery due to the impulse of the parachutes opening. Analysis has been done on the size, location, and number of bolts used to secure the two connectors together. There will be eight ¼”-20 black oxide steel socket head cap screws which have an ultimate tensile strength (Fu) of 180000 psi [3]. These bolts will primarily be under shear loading, and the allowable shear stress these bolts can withstand is governed by the following equation 8.2.

$$Rn = m\left(0.5Fu\right)Ab \tag{8.2}$$

Where *Rn* is the shear load, *m* is the number of bolts in the configuration, and *Ab* is the area of the bolt exposed to shear. The exposed area is 0.0368 square inches for each bolt. The total shear load this configuration can withstand is 26468 lbs giving a factor of safety of 26.

The aluminum also has the possibility of failing in recovery. The equation used to determine failure criteria is the following equation which governs the bearing limit state[4]:

$$Rn = 2t\left[Le - \frac{d}{2}\right]Fbru \tag{8.3}$$

Where *Rn* is the shear load, *t* is the thickness, *Le* is the length from the center of the bolt hole to the edge of the part, *d* is the diameter of the hole, and *Fbru* is the ultimate bearing strength. The ultimate bearing strength is 48000 psi [4]. For the connector, the shear bearing strength of each hole is 2745 lbs, and each hole will be taking about one eight of the load. Therefore, the factor of safety is 21.

8.6. Fabrication Analysis

For fabrication methods for the body tube, see Section **Error! Reference source not found.**. The filament winder is the best method to creating a smooth outer profile. Hand-laying carbon fiber cloth would likely result in a dimpled and imperfect surface with frayed edges. The autoclave will be used in conjunction with high temperature curing epoxy for superior mechanical properties. A diamond-coated Dremel cutting wheel will be used to provide a clean cut, disrupting as few of the fibers as possible. Coolant will be employed to ensure the epoxy does not melt, and the cutting line will be wrapped in tape to minimize splintering. Room temperature epoxy could be applied to the cut edges to re-laminate them. Total cost for fabricating the body tube would be approximately $91, assuming the high-temperature curing epoxy can be acquired at no cost.

Primary bulkheads will each be fabricated from a 6061 aluminum rod, 6.5 inches in diameter and 3.0 inches in length. Fabrication will begin by turning down the outer profile to appropriate dimensions, flipping the piece in the lathe chucks. Once this is complete, the ends of the piece will be faced off. Then a large hole will be drilled into the center of the work piece, large enough to fit a boring bar inside. A boring bar will then be used to turn down the inner profile to proper dimensions. With sleeve-fitting pieces, one piece will be fabricated then measured; these measurements will then be used to fabricate the second piece for a better fit. A mill will be used to match-drill the fastener holes. Fasteners used will be *fine* threaded to ensure minimal loosening during handling or flight. Plywood bulkheads will be laser-cut.

The lips on the pieces that will be in contact with the body tube will be sanded with coarse-grit sand paper to improve adhesion to the body tube; these surfaces will also then be coated with Alodine then primed to resist the galvanic corrosion between the carbon fiber and the aluminum. Bulkheads will cost approximately $315 to fabricate.

Fins will be fabricated by first purchasing blue-foam cores from a manufacturer. On top of these cores, carbon fiber tow will be hand-wrapped in both 45° orientations and the 90° orientations. Then this composite would be baked in the autoclave. Fins will cost about $100 to fabricate.

The fabrication of the nosecone will begin by first 3-D printing a mold in segments that will sleeve-fit onto each other. These pieces will then be bonded to each other. This mold will then be lightly sanded with fine-grained sand paper until the seams are blended. The mold will then be sprayed liberally with dry Teflon mold release. The projected area of the nose cone will be used to create a stencil with a 5/16 inch border around the outline. This stencil will then be used to cut out nine equal shapes of 3K, plain-weave carbon fiber cloth. Three of these shapes will cover the mold with minimal overlap, constituting the first layer of the nose cone. Two additional layers will be applied, covering the seams of the layer underneath. This could be room-temperature cured. After wet sanding and applying a spray of clear coat, fabrication of the nosecone would be complete. The nosecone will cost approximately $135 in total.

Shared tools and materials would cost approximately $82, bringing the total cost of structures fabrication to $723.17.

8.7. Testing

The critical test for the vehicle structure is the adhesive for connecting aluminum parts to the body tube. To test this, portion of the carbon fiber body tube needs to be made. An aluminum piece with 6 inch diameter will then be bonded to the body tube section and a test will be performed to determine the load required to separate the two.

8.8. References

[1]http://www.pcepoxy.com/our-products/paste-epoxies/pc-7.php
[2]MIL-HDBK-5J
[3]http://www.mcmaster.com/#socket-head-cap-screws/=paoynz
[4]https://engineering.purdue.edu/~jliu/courses/CE470/PPT_PDF/ce470bolts_S11.pdf

9. Safety

9.1. Objective

Safety is of utmost importance to the members of the Sounding Rocketry Team. Due to the risks associated with constructing a high altitude rocket, team member safety will be addressed at all stages of the design, testing, and launch. One of the team members will be designated as the Safety Engineer. His/her main responsibility is to ensure the team performs all building and testing in a safe manner that follows university and department regulations. This includes coordinating necessary training for all team members. In addition, the Safety Engineer is responsible for completing Project Safety Analysis (PSA) documents for the engine test, recovery test, launch, and any other testing where it is deemed necessary. It is his/her responsibility to be familiar with the PSA's and to be prepared with a course of action in the event of an emergency.[1]

9.2. Documentation

Prior to creating a PSA, the test procedures need to be outlined and approved by an appropriate faculty member. Each team member involved in the test will be required to be familiar with all nominal and contingency procedures. Once the test procedures have been approved, the PSA documentation can began. Allow this process to take place at least 1-2 weeks prior to testing, as the required PSA signatures may take time to receive. Once the necessary signatures are obtained, a copy of the PSA should be mailed to the TAMU Environmental, Health, and Safety Department (EHSD). Once this step has been completed, the team is cleared for testing. There should be at least one copy of the PSA on site during testing in the event of an emergency.[1]

In addition to the PSA's, each applicable vehicle component will have its own Standard Operating Procedure (SOP) that outlines how it is to be used and operated under normal operating conditions. Contingency and troubleshooting procedures should also be attached for team reference. This will prevent systems from being used in ways that could lead to unsafe situations. Moreover, all hazardous materials will be accompanied by the appropriate Material Safety Data Sheets (MSDS).

9.3. Training Requirements

All team members are required to complete the necessary safety training. In order for students to use machine shop tools, training in the safe handling of machinery, tools, and materials is required. In addition, basic lab safety is expected at all times when students are in the lab. This includes but is not limited to closed toe shoes worn at all times, safety googles and gas masks worn when working with airborne particles, and no food or drink brought into the lab space. Furthermore, all students will complete the fire extinguisher training provided by TAMU EHSD. This training is imperative for launch and engine testing. The Safety Engineer is responsible for coordinating all team training and for ensuring that the lab and testing sites remain safe for team members at all times. Any safety concerns will be brought to the Safety Engineer and appropriate faculty and handled immediately.

9.4. Testing Authorization

Testing of the rocket and its subsystems prior to launch at the competition is critical to ensuring a safe and successful launch. Ground or flight testing of the recovery system must be videoed and submitted to the Experimental Sounding Rocketry Association (ERSA) no later than March 31, 2014. In addition, all wiring associated with recovery and safe operation of the rocket must conform to the wiring rules provided by the ERSA competition.[2] Full scale test launches prior to competition will ensure safe and proper integration of all rocket subsystems and will abide by the Tripoli Rocket Association of Waco.[3]

9.5. References

[1]Benson, A., et al., "Volare Senior Design Project Final Report," Texas A&M University, Aerospace Engineering Department, May 2010.

[2]"Intercollegiate Rocket Engineering Competition Rules." Experimental Sounding Rocket Association [online], URL: http://www.soundingrocket.org/rules.html [cited 30 Jan 2014].

[3]"Safety." Tripoli Rocketry Association, Inc. [online], URL: http://www.tripoli.org/Launches/Safety/tabid/182/Default.aspx [cited 30 Jan 2014].

10. Registration and Finance

10.1. Registration Deadlines

The 2014 Intercollegiate Rocket Engineering Competition team application must be submitted by November 15, 2013. Three update applications must be submitted by January 15, March 15 and May 15, 2014. The update applications must detail only the information that changes from the original application.

10.2. Budget

The current budget is set for $25,000. Of this, $6,700 is allotted for the subsystems, with $1,200 allocated to Structures, $1,500 allocated to Dynamics and Operations, $3,000 allocated to Propulsion and no more than $1,000 allocated to the payload construction. This will cover the material costs for each team to build their components of the rocket. A portion of the Propulsion budget is set aside for launching costs, including fire department fees.

Secondly, $1,050 is allotted for IREC registration costs. Basic registration costs $400 per school (for up to eight students/advisors). There is a $50 charge for each extra student and $55 charge for each extra advisor. With our current 21 person team, an additional $650 must be spent on registration fees for the additional 13 people, assuming the entire team is eligible and willing to go to the competition.

An estimated $4,680 is allotted to transportation and lodging costs (based on a worst-case scenario approximation) for renting two vans from Enterprise for $2,100, with an approximated $600 allocated for gas expenses. The cheapest motel rates found in Green River, UT were at the Motel 6 for $60 a night, housing two people per room. This brings the lodging expenses up to $1,980 for three nights.

The remaining $12,080 is budgeted as a buffer for any extra unexpected expenses. Any unused money will be set aside for the 2014-2015 Sounding Rocketry Team to use. The following table illustrates the budget set for the 2013-2014 year.

Table 10.1. Budget layout for the academic year.

Budget Breakdown 2013-2014

Building Costs	
Structures	$1,200.00
Dynamics and Operations	$1,500.00
Propulsion	$3,000.00
Payload	$1,000.00
IREC Registration	$1,050.00
Transportation/Lodging	$4,680.00
Extra (Buffer)	$2,570.00
Tumlinson ’51 Fund	***$2,500.00***
Student Engineers Council	***$900.00***
ASME	***$500.00***
Profit Share 12/10 (Panda Express)	***$205.34***
Total	**$10,894.66**

10.3. Fundraising/Sponsorships

The Sounding Rocketry Team has been granted $2,500 from the Tumlinson ’51 Leadership Fund in Aerospace Engineering, $900 from the TAMU Student Engineers Council, and $500 from the American Society of Mechanical Engineers. The Sounding Rocketry Team raised $205.34 at a profit share with Panda Express on December 10, 2013 and has another profit share planned with Panda Express for March 31, 2014. A profit share with Chick-fil-A has also been planned for March 5, 2014.

Two Reed Arena clean up events have been planned, each yielding $600 profit for the Sounding Rocketry Team. Raising Cane’s supports many local organizations through hosting fundraisers and by sponsorship. The Sounding Rocketry Team has contacted Raising Cane’s about obtaining a sponsorship and is currently awaiting a reply.

Several local and national organizations have also been contacted to help with financial assistance, including the TAMU Student Organization Advisory Board, American Institute of Aeronautics and Astronautics (both local and national chapters, including the Technical Committee for Hybrid Rockets), Society for the Advancement of Materials and Process Engineering (both local and national chapters), as well as engineering companies like Capstone Natural Resources.

11. Conclusion

Team evaluations were conducted at the conclusion of the second preliminary design review of last semester. Each team member’s performance was rated and critiqued, though for the most part members stayed very active in participating. This opportunity was also used for members to honestly comment on the leadership ability of the managers. This holds everyone accountable to their actions, including leaders, and diminishes the likelihood of

members getting all the recognition without the work. So far, everyone who has started out on the team has been retained. Originally, there were two Brazilian students who were collaborating with the team, though one dropped out roughly two weeks into the fall semester.

Fabrication of the rocket begun over the winter break with the investigation into the filament winder. Right now, the engine team has ordered parts to start construction of the combustion chamber and cast the fuel grain. One carbon fiber tube was attempted and, for the most part, was successful outside the problem of getting the tube off of the stainless steel mandrel. This problem has been since resolved and more materials have been ordered. The dynamics and operations team has begun the scaling of the rocket in SolidWorks for wind tunnel testing. One stabilizer fin has already been rapid prototyped and the other parts are pending in the queue while some things are fixed.

Financially, the funds are available to build the rocket in its full form. This will occur over the next few weeks. Testing will begin immediately as items become available. The challenge lies within sending the entire team to Utah, but this shouldn't be a huge problem considering a number of individuals will not be able to attend.

The team will continue to prepare for the competition in June by test launching in late March or early April. This will help the team get comfortable with the process of setting up equipment and the ignition sequence. As time goes by, a lot still has to be figured out but the leaders and members alike are taking great leaps in learning what needs to be done and making sure that it is executed.

12. Acknowledgments

This team is the product of many different people working together from all corners of the university. There is no one person that could have made all this happen. That being said, each person listed here has been invaluable in more ways than one.

First, the team would like to thank Dr. Rodney Bowersox for his advisement during the entire course of this project. He has been extremely patient with our progress and has helped the team grow from just an idea to a fully functioning team. He never hesitated to sign on for this project and his encouragement has made this all a possibility.

Another round of thanks goes to Dr. Pollock for his great deal of experience regarding practical rocketry. His knowledge and guidance has been greatly received and he has always supported us in any way he can. Whenever we have questions he is always one of the first people we ask.

For his efforts far exceeding expected contributions, the Sounding Rocket Team would like to commend Dr. Creasy of the Materials Science and Engineering Department at Texas A&M University. In addition to permitting access to his Little Hornet filament winder and autoclave, he has continuously met with team members to provide technical expertise. He has also worked diligently to acquire materials to be used during body tube fabrication. Due to his assistance, progress has continued and budget has been spared.

We would also like to thank Drs. Karpetis, Chamitoff, and Shryock for their attendance at the preliminary design reviews. These reviews allowed us to present our ideas collaboratively and the information and advice that they offered

was invaluable. Other professors who have contributed to the guidance of the team include Drs. Hurtado, White, and Bhattacharya. While this is a student-led team, we are extremely grateful for the assistance in a project of this magnitude. All the professors mentioned have been enthusiastic and supportive which means the world to a team like this in its first year.

Additional thanks would like to be extended to William Seward and Carl Johnson for their instruction in machining techniques as well as the hours they volunteered on some of the components. Whenever we encountered a problem they always had practical solutions. Thanks also goes to The Low Speed Wind Tunnel staff and Cecil Rhodes who also helped in the instruction of materials and fabrication.

Other individuals who have contributed a great deal are James Wilson of the Engineering Innovation Center and the sponsors who have donated funds to the project, including the American Society of Mechanical Engineers, the Student Engineering Council, and the Tumlinson ’51 funds granted by the Department of Aerospace Engineering.